Brillouin Spectroscopy of Gelatin Gel and the Use of a CCD Area Detector

by

PEIZHEN ZHAO

A Thesis

Submitted to the School of Graduate Studies

in Partial Fulfilment of the Requirements

for the degree

Doctor of philosophy

McMaster University

January, 1995

BRILLOUIN SPECTROSCOPY OF GELATIN GEL AND THE USE OF A CCD AREA DETECTOR

DOCTOR OF PHILOSOPHY (1995) MCMASTER UNIVERSITY
(PHYSICS)

TITLE: Brillouin spectroscopy of gelatin gel and the use of a CCD area detector

AUTHOR: Peizhen Zhao
B.Sc. (Tsinghua University)
M.Sc. (Tsinghua University)
M.Sc. (McMaster University)

SUPERVISOR: Dr. D. Walton

NUMBER OF PAGES: xix, 145

ABSTRACT

Brillouin scattering method was used to study two kinds of materials: gelatin gel and quasicrystal $Al_{63.5}Cu_{24.5}Fe_{12}$.

The measurements of Brillouin shift and width for gelatin-water system were carried out as a function of temperature, concentration, time and thermal history. New results and a phase diagram for melting were obtained. The results are discussed using different models. The longitudinal storage modulus of the gel network, the frictional damping parameter and the melting enthalpy have been evaluated. However, in order to explain all the experimental results and get the more accurate values for those parameters, a more perfect theory for this biopolymer system is needed.

A more efficient technique — CCD used as a detector, is described, too.

ACKNOWLEDGMENTS

I would like give my sincere thanks to the following persons:

Dr. D. Walton, my supervisor, for giving me the chance to be involved in this project, providing the model, and fostering my ability to do research independently and overcome difficulties;

J. J. Vanderwal for his great technical assistance and helpful discussion;

Dr. G. P. Johari for his suggestions in choosing the thesis project and advice;

Dr. J. P. Carbotte, Dr. J. S. Preston, Dr. S. Zhu, Dr. I. D. Brown and Dr. H. Xia for their helpful discussions and advice;

Dr. D. W. Taylor for his help in the use of WORDPERFECT, Dr. M. F. Collins for his kindness in letting me use the computer in his lab, and R. A. Duncan for his help in solving computer problem;

Dr. C. Holmer for providing the sample of AlCuFe;

Physics Department's support and help, especially from Dr. D. L. Welch, Dr. D. W. L. Sprung, M. Wilby, W. Malarek, C. Johnston, R. McNeice and J. Collin;

My family, especially my mother, for their support in various aspects;

Everyone who gave me moral encouragement.

I wish all the persons mentioned above good luck in their own careers.

Contents

PREFACE

Brillouin scattering is one of the most commonly used techniques for investigating low energy elementary excitations in particular phonons. Its spectroscopy is a powerful tool to obtain the desired information about the elastic properties of materials. It is not only a methodologic extension of classical ultrasonic techniques to hypersonic frequencies, but also an outstanding spectroscopic method which is especially well adapted to investigate the static and dynamic acoustic properties, and the opto-acoustic and optic properties of materials. It has the following advantage: accurate and high resolution (one or two orders of magnitude better than that obtained in neutron spectroscopy), small sample volume (the focus spot can be smaller than 10 μm), and no damage to samples. As part of this project, I studied the possibility to use CCD as a detector in Brillouin scattering and found this new method is more efficient than the scanning way but it has its own weakness.

The other part of this project is about the application of the Brillouin scattering technique. I used this technique to study two different kinds of materials: one is the transparent binary polymer/solvent system — gelatin gel and another is the opaque quasicrystal — $Al_{63.5}Cu_{24.5}Fe_{12}$.

Gelatin gel has been used for a long time and studied quite a lot. On the contrary, quasicrystals were discovered only 10 years ago and the research about it is just beginning. However, no matter how different their histories are, they are both quite new as samples for the Brillouin scattering: this is the first time that the Brillouin spectroscopy method is used to study the elastic properties of quasicrystals. The properties of gelatin gel have never before been so thoroughly studied by this method in the hypersonic frequency range. Moreover, new results have been obtained, which is useful to fully understand this material.

This thesis contains two parts. Part one is about Brillouin scattering technology, in which the new technique — CCD used as a detector, is described. In order to let reader have a general idea about Brillouin scattering, a brief introduction is given in chapter 1, showing the differences when this technique is used to study transparent and opaque materials. Part two deals with Brillouin Spectroscopy of gelatin gel and quasicrystal AlFeCu. Chapter 3 is the main part of this thesis, where experimental results of gelatin gel will be displayed and analyzed by three models. The results about quasicrystal AlFeCu is presented in chapter 4. In appendixes, some basic theories used in the models are introduced. At last is the list of bibliography.

List of Symbols

a $V_m/\lambda(\sigma-\sigma_o)$ (in Chapter 3, model 1)

a transverse correlation length that characterizes the surface roughness (in Chapter 4)

A_i amplitude of the incident light

A_t amplitude of the transmitted light

c concentration, the weight ratio of gelatin powder to water

c_w concentration, %w/w

c_{11} elastic constant

c_{44} elastic constant

C contrast of Febry-Perot interferometer

D mirror separation of Febry-Perot interferometer

f friction coefficient

f' functionality

$f(x_1,x_2)$ displacement normal to the surface at point (x_1,x_2)

f_i focal length (i=2,3,4,5,6)

G complex shear modulus (in Chapter 1)

G shear storage modulus of the network (in Chapter 3)

I light intensity

j number fraction, the ratio between the junctions and the molecules in the network

k	fluid permeability
k_i	incident light wavevector
k_s	scattered light wavevector
K^*	bulk storage modulus of suspension
K_b	bulk storage modulus of network
K_s	bulk storage modulus of solid
l	mean free path
m_m	gelatin molecular weight
m	mass
m_l	the mass of solvent (water)
m_g	the mass of gelatin powder
m_f	the mass of fluid in gel system
m_n	the mass of network in gel system
M	complex longitudinal modulus
M'	longitudinal storage modulus
M''	longitudinal loss modulus
M'_f	longitudinal storage modulus of fluid
M'_n	longitudinal storage modulus of network
n	refractive index
n_o	number of interference
N	number density of gelatin molecules
p	the number of reflection
p	pressure (in Appendix 1)
q	sound wavevector
q_l	sound wavevector in the solvent

q_b bulk phonon wavevector

q_L longitudinal phonon wavevector

q_T transverse phonon wavevector

q_R surface phonon wavevector

$q^{\parallel}$ wavevector component parallel to the surface

$q^{\perp}$ wavevector component perpendicular to the surface

R_g gas constant

r radius

R radius of the image ring

R_f reflectivity of Febry-Perot mirrors

s displacement vector of the solid

S displacement vector of the fluid

t time

T temperature

T_m melting temperature

tgθ mechanical dynamic loss tangent

u solid velocity

U fluid velocity

v sound velocity

v_f sound velocity in the fluid

v_n sound velocity in the network

v_L longitudinal wave velocity

v_T transverse wave velocity

v_R surface wave velocity

V volume

V_m gelatin molecular volume

α mass (or number) fraction between m_g and m_n

α_o tortuosity parameter

γ sound absorption coefficient

Γ sound attenuation

Γ_l sound attenuation in liquid

Γ_B Brillouin full width at half maximum

δ_0 viscous skin depth

δ surface roughness parameter (in Chapter 3)

ΔH^o melting enthalpy

$\Delta\lambda_{FSR}$ free spectral range in wavelength unit

$\Delta\nu_{FSR}$ free spectral range in frequency unit

ε dielectric constant

η_v bulk viscosity

η_s shear viscosity

θ scattering angle (in Chapter 1)
transmitted angle (in Chapter 2)

θ_i incident angle to the surface normal of the sample

θ_s scattering angle to the surface normal of the sample

κ the coefficient between ν and R^2 (in Chapter 2)

λ coupling constant (in Chapter 3, model 2)
wavelength (otherwise)

ν frequency (sec^{-1})

ν_B Brillouin shift

ν	crossover frequency
ρ	mass density
ρ_T	total density of the gelatin-water system
ρ_l	solvent density in the gelatin-water system
ρ_g	gelatin density in the gelatin-water system
ρ_f°	the equilibrium density of the fluid in the gel
ρ_n°	the equilibrium density of the network in the gel
σ	scattering cross-section of a junction
σ_o	scattering cross-section of a gelatin molecule
σ'	Poisson's ratio
τ	phonon lifetime
ϕ	volume fraction
Φ	fluid resistance
Ψ	thermodynamic variable
ω	angular frequency

List of Figures

List of Tables

Part A

Brillouin Scattering Technology

Chapter 1

Concept of Brillouin Scattering

1.1 Bulk Phonon and Surface Phonon Modes

Brillouin scattering is an excellent means of investigating the elastic and photo-elastic properties of materials.

Depending on the properties of the materials, incident light can be scattered inelastically by phonon-induced fluctuations of the dielectric constant in the medium, or by ripples on the surface of the solid, or both.

In the Brillouin spectra of transparent solids, usually three pairs of bulk phonon peaks can be seen: one for longitudinal, two for transverse phonons. For liquids, only longitudinal phonon peak can be seen. From the conservation rule of energy and momentum between phonon, incident and scattered photons, bulk phonon wave-vector **q** can be calculated as

$$q=\frac{4\pi n\sin\frac{\theta}{2}}{\lambda_0} \tag{1}$$

where λ_o is the wavelength of incident light in vacuum, n the refractive index of the scattering system, and θ the scattering angle. The relationship between sound velocity and phonon frequency ν_B is given by

$$\nu_B=\frac{2n}{\lambda_o}v\sin\frac{\theta}{2} \tag{2}$$

This inelastically scattered light is broadened compared with the incident light due to the sound attenuation. Let γ be the sound absorption coefficient (cm^{-1}) then the Brillouin full width at half maximum (FWHM) is given by

$$\Gamma_B=\gamma v/\pi \tag{3}$$

which is inversely proportional to the life time of the phonons involved in the scattering process.

Light scattering from acoustic phonons in opaque materials is quite different:

Firstly, the high optical absorption limits the scattering to a volume close to the sample surface, which has an influence on the wave vector conservation. If the wavevector conservation for bulk phonons is expressed as

$$\begin{cases} q_b^{\parallel}=k_i\sin\theta_i+k_s\sin\theta_s \\ q_b^{\perp}=n(k_i\cos\theta_i'+k_s\cos\theta_s') \end{cases} \tag{4}$$

where $q_b^{\parallel}$ and $q_b^{\perp}$ are the two components, parallel and perpendicular to the surface respectively, θ_i and θ_s are the incident

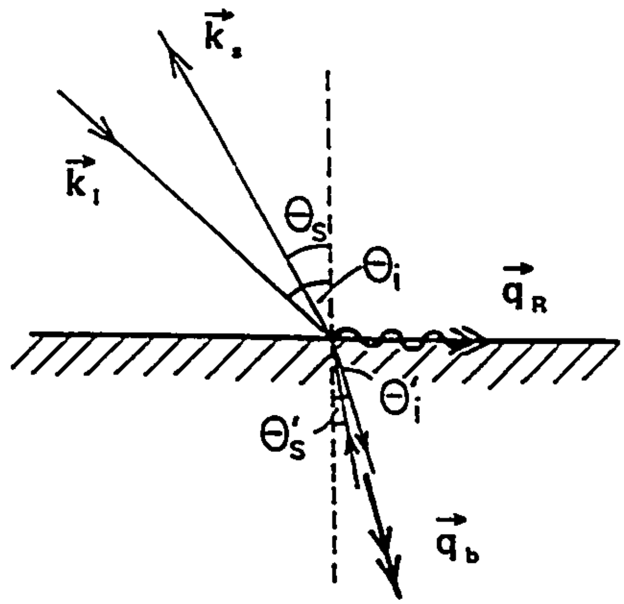

Fig. 1.1 Scattering geometry, where $\vec{k}_i$ and $\vec{k}_s$ are incident and scattered light wavevectors, and $\vec{q}_R$ and $\vec{q}_b$ the surface and bulk phonon wavevectors.

and scattering angles to the surface normal of the sample respectively, θ'_i and θ'_s are the corresponding refractive angles (Fig. 1.1), condition 2 breaks down (uncertainty principle) in this case since the light penetrates only a short distance below the surface, which leads to a weaker and broader spectrum (Sandercock, 1978).

Secondly, the effect of the surface on the excitations cannot be ignored. This effect manifests itself in the reflection of bulk excitations at the surface, which causes the asymmetrical Lorentzian lineshape of the bulk phonon peaks and the appearance of new excitations.

Thirdly, the ripples produced on the surface by these excitations scatter light, and for highly opaque materials it may be the dominant scattering source (Sandercock 1982; Mishra et al., 1977).

Brillouin cross sections depend on the power spectrum of the surface displacements normal to the surface, and the differential scattered power of ripple scattering is propotional to (Loudon, 1978; Loudon et al., 1980; Sandercock, 1982)

$$Re\left\{\frac{\omega v_T^3 q^{\parallel 2} q_L^{\perp}}{4 v_T^4 q^{\parallel 2} q_L^{\perp} q_T^{\perp} + (\omega^2 - 2 v_T^2 q^{\parallel 2})^2}\right\} \tag{5}$$

where

$$q_L^{\perp}=[(\omega/v_L)^2-q^{\|2}]^{1/2}$$
$$q_T^{\perp}=[(\omega/v_T)^2-q^{\|2}]^{1/2} \tag{6}$$

and v_T and v_L are bulk transverse and longitudinal wave velocities, respectively.

From Eq. (5), three frequency regimes can be distinguished:

a) $\omega<q^{\|}v_T$. In this case, both q_T and q_L are purely imaginary, so is the factor in the large brackets of equation (5). Thus the differential scattered power is zero except at the frequency ω_R of a pole corresponding to the Rayleigh surface acoustic wave.

b) $q^{\|}v_T<\omega<q^{\|}v_L$. In this case, q_T is real but q_L is purely imaginary. The cross section is zero at the two ends of the range but otherwise is nonvanishing and the spectrum has a continuous distribution between these two ends.

c) $q_R v_L<\omega$. Now both q_T and q_L are real. Re{$\cdots$} is nonzero except at the bottom end of the range and the spectrum has a continuous distribution extending from $\omega = v_T q^{\|}$ to higher frequencies.

So, the surface-ripple Brillouin spectrum consists of a dominating peak at the frequency of the Rayleigh surface wave, ω_R, accompanied by shoulders which extend to higher frequencies where bulk waves are allowed. $\omega_R=q_R v_R$, where q_R and v_R are the surface wavevector and velocity respectively.

$|q_R|=q^I$ and the wavevector remains precisely defined through condition 1, so a sharp peak should be observed.

The exact form of the spectrum depends on the ratio v_T/v_L. And the intensity is related to the reflectivity: the higher the reflectivity the larger the intensity.

There is a relationship between v_R, v_T and v_L. For an isotropic substrate (Farnell, 1970),

$$[2-(v_R/v_t)^2]^4=16[1-(v_R/v_l)^2][1-(v_R/v_t)^2] \qquad (7)$$

Surface modes are localised typically within a wavelength from the surface and normally would not be observed in transparent material. Opacity is a requirement, which can be qualitatively explained by an electron-mediated coupling mechanism to the phonon. In opaque materials the light is absorbed close to the surface and many electron-hole pairs are produced in the medium just in that region where the surface wave exits (Sandercock, 1978).

1.2 Complex Moduli and Brillouin Spectrum

The propagation of sound in a homogeneous isotropic visco-elastic medium depends on the mechanical and thermal properties of the material. It is convenient to define a complex longitudinal modulus

$$M(\omega) = M'(\omega) + iM''(\omega) \tag{8}$$

to describe the mechanical property of a material with elastic behaviour as well as viscous losses. The real part M', often called the storage modulus, according to the storage of mechanical energy, determines the elastic part of the stress. The imaginary part M", the loss modulus, which gives a measure of the dissipation of mechanical energy, determines the viscous part of the stress. It can be found (Litovitz, 1965)

$$M' = \rho v^2 \frac{1-(\frac{\gamma V}{\omega})^2}{[1+(\frac{\gamma V}{\omega})^2]^2} \tag{9}$$

$$M'' = \frac{2\rho v^2 (\frac{\gamma V}{\omega})}{[1+(\frac{\gamma V}{\omega})^2]^2} \tag{10}$$

where ρ is the density of the material, ω the circular frequency of the wave. M" is related to viscosity η by

$$M'' = \eta\omega \tag{11}$$

For a gel-like material one should observe $M'(\omega) \gg M''(\omega)$, and $M'(\omega)$ and $M''(\omega)$ should vary little with frequency.

The mechanical dynamic loss tangent is defined as

$$tg\delta = \frac{M''}{M'} = \frac{2\frac{\gamma V}{\omega}}{1-(\frac{\gamma V}{\omega})^2} \tag{12}$$

It is easy to see that $\gamma v/\omega = \Gamma_B/2\nu_B$, so

$$M'=\rho v^2\frac{1-\frac{1}{4}(\frac{\Gamma_B}{\nu_B})^2}{[1+\frac{1}{4}(\frac{\Gamma_B}{\nu_B})^2]^2} \tag{13}$$

$$M''=\rho v^2\frac{\frac{\Gamma_B}{\nu_B}}{[1+\frac{1}{4}(\frac{\Gamma_B}{\nu_B})^2]^2} \tag{14}$$

and

$$tg\delta=\frac{\frac{\Gamma_B}{\nu_B}}{1-\frac{1}{4}(\frac{\Gamma_B}{\nu_B})^2} \tag{15}$$

When $(\gamma v/\omega)^2<<1$, these equations can be simplified to

$$M'=\rho v^2 \tag{16}$$

$$M''=\rho v^2\Gamma_B/\nu_B \tag{17}$$

Complex shear modulus G and complex compressional modulus K can also be defined (Herzfeld et al., 1959). And

$$M=K+\frac{4}{3}G \tag{18}$$

Brillouin data are sensitive to the shear rigidity of the system too, even though only longitudinal properties can be probed directly, as in the experiments I have conducted.

Chapter 2

The Use of CCD in Brillouin Scattering

Functionally, the CCD (charged-coupled device) is equivalent to electronic film. The first devices were invented in 1970 by Boyle and Smith of Bell Laboratories. Since then, work has been done to improve their performance. Now a class of devices, scientific CCDs, which are designed to meet the needs of low light level, wide dynamic range, high resolution and sensitivity, are widely used in areas such as astronomical observation, surveillance, and medical and industrial radiology. High quantum efficiency and broad spectral response (UV to near IR) render CCDs highly desirable as imaging devices for Febry-Perot (FP) interferometer application (Janesick et al., 1987; Abreu et al., 1989).

In the conventional method of Brillouin scattering, the FP is scanned by changing the mirror separation or the refractive index of the medium between the mirrors, and only the beam in a small solid angle along the optical axis with a certain wavelength can be transmitted at any given time. The effective time of data collection for a certain frequency range is only a small part of the whole scanning period. If, however, one could discriminate frequencies spatially rather than temporally, considerable increase in data collection efficiency would be obtained. This is possible using the new method, wherein the CCD is used as a detector and the FP as an etalon. A ring pattern which includes all the information will be collected at any time, and the transmitted light satisfies the following condition

$$2D\cos\theta = n_0\lambda \tag{19}$$

where D is the mirror separation, n_0 the order of interference (an integer), θ and λ the transmitted angle and the wavelength, respectively. That is to say there is no time wasted. However, because of the 2-dimensional pattern and the non-uniform illumination of the laser beam, it is not so straightforward as the scanning method to obtain the frequency spectra. In the following part, I will show the experimental arrangement, and how to transfer the 2-D ring pattern into a 1-D Brillouin spectra. Some experimental results will be given.

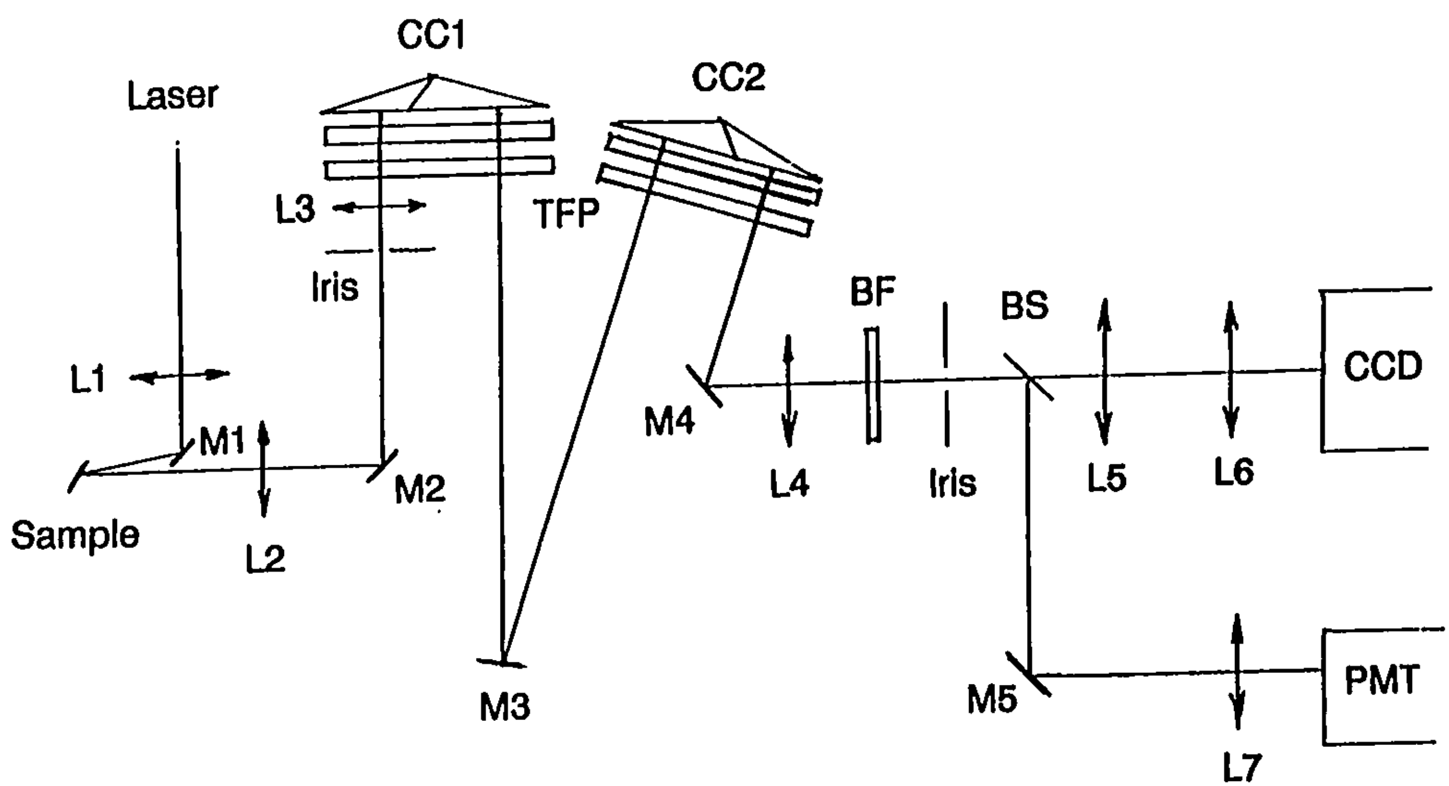

Fig. 2.1 The Schematic of the experimental apparatus using CCD as a detector.

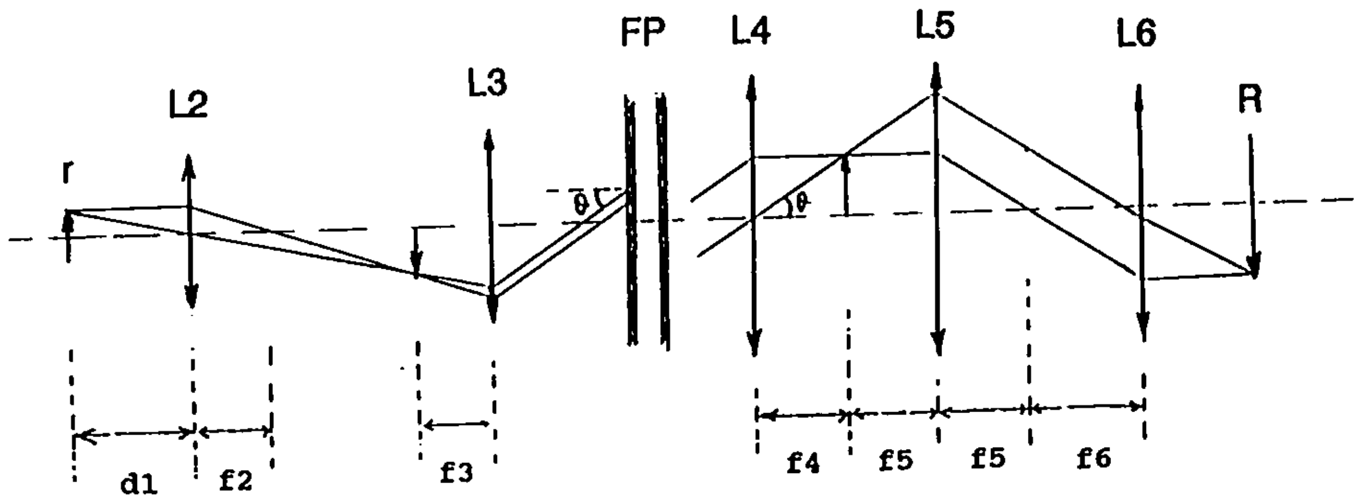

Fig. 2.2 Optical path diagram.

2.1 Experimental Arrangement

The Schematic of the experimental apparatus is shown in Fig. 2.1, which consists of a four-pass Sandercock tandem Fabry-Perot, a liquid nitrogen cooled CCD operating between 153K and 163K, a band filter (BF), and several lenses and irises. The light scattered by the sample forms an image on the CCD chip, composed of 512×512 pixels. In this arrangement, the important thing is to make sure that the image of lens 2 is on the focus plane of lens 3 and the image of lens 4 is on the focus plane of lens 5. A small fraction of the light is directed by a beam splitter (BS) to a photomultiplier detector which is used to align the system by scanning.

From the geometry apparent in Fig. 2.2 it can be deducted that the light appearing in an image ring with radius R comes from a corresponding ring with radius r on the source:

$$tg\theta = \frac{rf_2}{f_3(d_1-f_2)} \tag{20}$$

and

$$R = \frac{f_4 f_6}{f_5}\, tg\theta \tag{21}$$

where f_2, f_3, f_4, f_5 and f_6 are the focal lengths of corresponding lenses. Of course, only the light with wavelength satisfying the condition (19) can transmit and form that ring.

The maximum angle θ_{max} will be limited by the size of the CCD chip and the requirement that the light beam when multipassing through the FP will not overlap.

When doing the exposure, 4-4 binning is used to reduce the read noise.

2.2 From 2-D Ring Pattern to 1-D Brillouin Spectra

2.2.1 Frequency Calculation

Let us look at a whole order ring pattern, in which the main Rayleigh peak (elastic light) of wavelength λ_0 transmitted on the optical axis forms a dot in the centre, the phonon peak of a shorter wavelength λ transmitted at an angle θ to the optical axis forms a ring with radius R, and the first ghost Rayleigh transmitted at an angle θ_1 forms a ring with radius R_1 (Fig. 2.3a). We have

$$2D = n_0\lambda_0 \tag{22}$$

$$2D\cos\theta = n_0\lambda \tag{23}$$

$$2D\cos\theta_1 = (n_0-1)\lambda_0 = n_0(\lambda_0-\Delta\lambda_{FSR}) \tag{24}$$

where $\Delta\lambda_{FSR}$ is the free spectral range (FSR) in wavelength units. Thus,

$$\cos\theta = \frac{\lambda_0-\Delta\lambda}{\lambda_0} = 1-\frac{\Delta\lambda}{\lambda_0} = 1-\frac{\Delta\nu}{\nu_0} \tag{25}$$

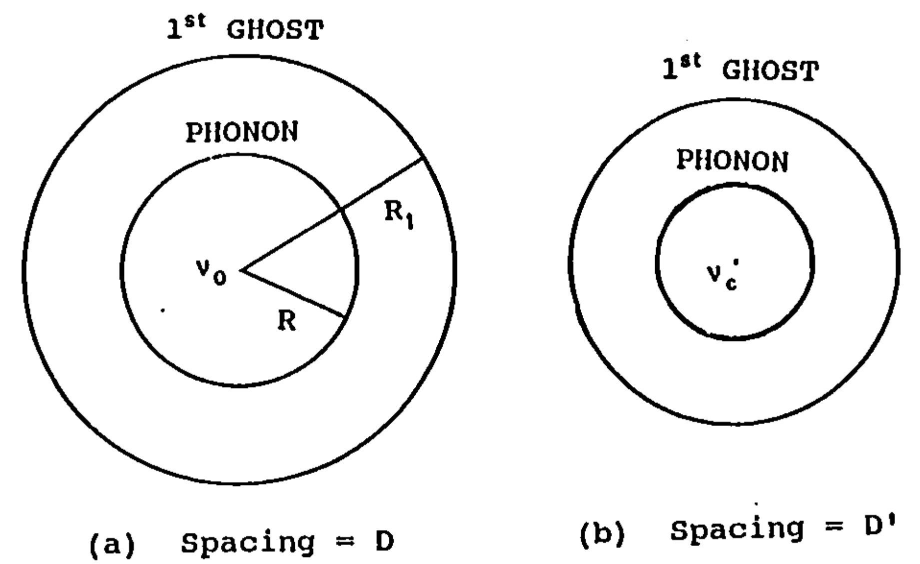

Fig. 2.3 Ring pattern from FP etalon (a) whole order (b) a partially collapsed order.

$$\cos\theta_1 = 1-\frac{\Delta\lambda_{FSR}}{\lambda_0} = 1-\frac{\Delta\nu_{FSR}}{\nu_0} \tag{26}$$

where $\Delta\nu$ expresses the frequency shift (phonon frequency) and $\Delta\lambda_{FSR}$ is the FSR in frequency units. Since

$$\cos\theta \approx 1-\frac{\theta^2}{2} = 1-\frac{R^2}{2s^2} \tag{27}$$

where

$$s = \frac{f_4 f_6}{f_5}\ Cm \tag{28}$$

we have

$$\Delta\nu = \frac{\nu_0}{2s^2}R^2 = \frac{R^2}{R_1^2}\Delta\nu_{FSR} \tag{29}$$

The above case is when we can see the whole order. However, more often we can only see a part of an order, whose frequency range (FR) (or window) is determined by the maximum angle

$$FR = \nu_0\theta_{max}^2/2 \tag{30}$$

Note that FR is determined by the experimental arrangement only, and there is no relation with the FSR. Of course, the size of the ring can be changed by changing f_4, f_5 or f_6 (usually by changing f_6 since lens 6 is a zoom lens). Because R_1 is proportional to FSR, if θ_{max} is limited by the size of CCD chip, FR can be increased by reducing f_6.

Usually, the ring pattern was collapsed to eliminate the large intensity central elastic light (Fig. 2.3b). In this case, $\Delta\nu$ just represents the frequency shift relative to the frequency of the central beam, ν_c. The phonon frequency will be

$$\nu_B = \Delta\nu + (\nu_c - \nu_0) = \frac{\nu_0}{2S^2}R^2 + (\nu_c - \nu_0) \tag{31}$$

where $\nu_c - \nu_o$ is related to the voltage offset acting on the piezoelectric crystals.

Suppose the rings were collapsed by changing the FP mirror spacing from D to D' and D" so that the corresponding frequencies of the central spot will be from ν_o to ν_c and $\nu_o + \Delta\nu_{FSR}$ (1^{st} order ghost peak). We have

$$\begin{aligned} 2D &= n_0\lambda_0 \\ 2D' &= n_0\lambda_c \\ 2D'' &= n_0(\lambda_0 - \Delta\lambda_{FSR}) \end{aligned} \tag{32}$$

Thus,

$$\frac{D-D'}{D} = \frac{\lambda_0 - \lambda_c}{\lambda_0} \equiv \frac{\Delta\lambda_c}{\lambda_0} = \frac{\Delta\nu_c}{\nu_0} \tag{33}$$

and

$$\frac{D-D''}{D} = \frac{\Delta\lambda_{FSR}}{\lambda_0} = \frac{\Delta\nu_{FSR}}{\nu_0} \tag{34}$$

where

$$\Delta\nu_c = \nu_c - \nu_0 \tag{35}$$

So,

$$\frac{D-D'}{D-D''} = \frac{\nu_c-\nu_0}{\Delta\nu_{FSR}} \tag{36}$$

Since there is a linear relationship between the mirror spacing and the voltage offset acting on the piezoelectric crystals via D/A device,

$$\nu_c-\nu_0 \equiv \frac{Z'_{off}-Z_{off}}{Z''_{off}-Z_{off}}\,\Delta\nu_{FSR} \tag{37}$$

where Z_{off} and Z'_{off} and Z''_{off} are the corresponding voltage offsets, which can be read from the meter easily.

2.2.2 Illumination and the Calculation of Intensity

The size and the width of a ring corresponding to the frequency range $\nu\pm\delta\nu$ will be changed by changing the FP mirror separation D, but the total area covered by this ring keeps constant since

$$d\nu \propto RdR \tag{38}$$

i.e. the larger the ring the smaller its width. Therefore, if the sample is uniformly illuminated, the intensity of the ring should not be changed when you enlarge or contract the ring.

Unfortunately, the intensity of the laser beam drops off from the centre, e.g. according to a Gaussian profile

$$I(r) = \frac{P_0}{\pi B^2} e^{-\frac{r^2}{B^2}} \tag{39}$$

where P_0 is the total power in the beam and B the width. It will produce a corresponding exponential drop-off in the image. By using a defocused laser beam, the drop-off will be smaller, but it is still there. So, the calibration by using the intensity of Rayleigh peak rings at different positions is important.

The intensity of the Brillouin spectrum, $I(\nu)$, can be calculated as follows:

Let $I(R)$ be the integrated intensity along the circle of radius R

$$I(R) = \sum_{i=1}^{N} I_i \tag{40}$$

where N is the total number of the pixels on the circle and I_i the counts of the i^{th} pixel. $I(R)$ can be changed to $I(\nu)$ by using the relation

$$I(R)\,dR = I(\nu)\,d\nu \tag{41}$$

or

$$I(\nu) = \frac{I(R)}{2\kappa R} \tag{42}$$

where κ is the coefficient between the frequency and R^2, i.e.

$\nu = \kappa R^2 + (\nu_c - \nu_o)$.

Because of the illumination problem mentioned above, this intensity is not the real intensity and it has to be corrected:

By changing the FP mirror spacing D to get a series of Rayleigh peak rings, and calculating the integrated intensities I_r of all these rings to get a relation between I_r and R, which reflects the drop-off of the laser beam intensity; then dividing I(R) by $I_r(R)$ to eliminate the illumination problem, and transforming this corrected intensity $I_c(R)$, which is $I(R)/I_r(R)$, into $I_c(\nu)$

$$I_c(\nu) = \frac{I_c(R)}{2\kappa R} = \frac{I(R)/I_r(R)}{2\kappa R} \tag{43}$$

2.2.3 Walk-off Problem

The amplitude of the transmitted light is

$$A_t(P) = (1-R_f)\frac{(1-R_f^p e^{ip\delta})}{(1-R_f e^{i\delta})}A_i \tag{44}$$

where p is the number of reflections, R_f the plate reflectivity, A_i the incident amplitude, and δ, the phase angle between successive reflections, is given by (Born and Wolf, 1975; Hecht, 1987)

$$\delta = \frac{4\pi}{\lambda} D \cos\theta \tag{45}$$

For certain transmitted beam width r_1, the reflection number is determined by the angle θ and FP spacing D

$$p = \frac{2r_1}{2D\ tg\theta} = \frac{2r_1 \Delta\nu_{FSR}}{c\ tg\theta} \tag{46}$$

In the scanning method, $\theta \to 0$, so that $p \to \infty$ and the transmitted intensity $I_t(\infty)$ is given by

$$I_t(\infty) = A_t(\infty) A_t^*(\infty) = \frac{(1-R_f)^2}{(1-R_f)^2 + 4R_f \sin^2\frac{\delta}{2}} I_i \tag{47}$$

where T_i is the incident intensity. The contrast for a single-pass FP will be

$$C_1(\infty) = \frac{(1+R_f)^2}{(1-R_f)^2} \tag{48}$$

In this new method, the transmitted intensity is given by

$$I_t(p) = \left[(1-R_f^p)^2 + 4R_f^p \sin^2(\frac{p\delta}{2})\right] I_t(\infty) \tag{49}$$

The finite p causes the attenuation of the intensity and the increase of the width of the transmitted light peak (Fig.2.4). But, it is almost no influence on the contrast, which is calculated according to the formula $C(P)=I_t^{max}(P)/I_t^{min}(P)$. In figures 2.5 and 2.6, I plotted the curves $I_t^{max}(p)/I_t^{max}(\infty)$ and $C_4(p)/C_4(\infty)$ respectively, where the subscript 4 means it is the

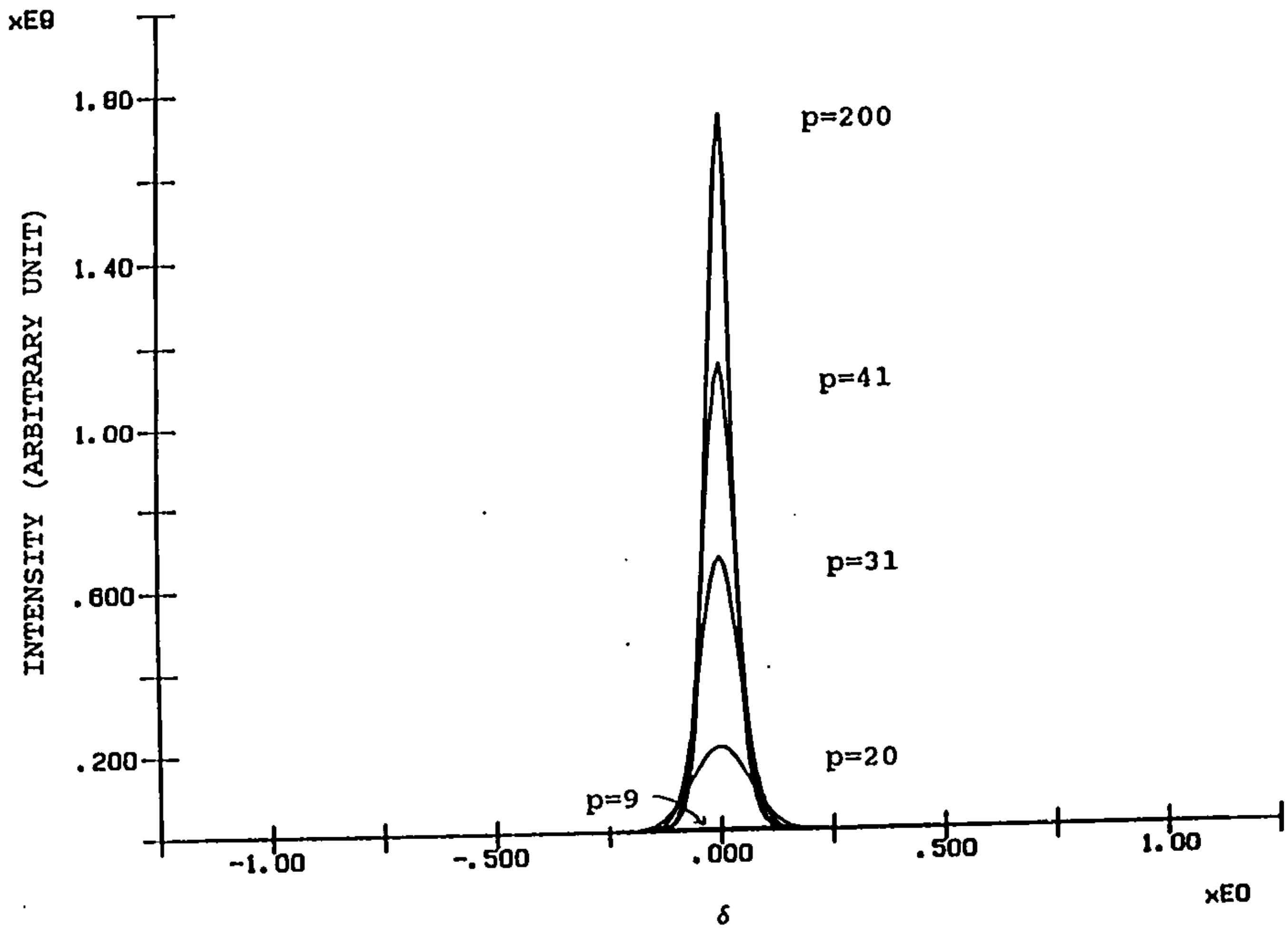

Fig. 2.4 The transmitted light spectra of a 4-pass Febry-Perot interferometer for various number of reflection.

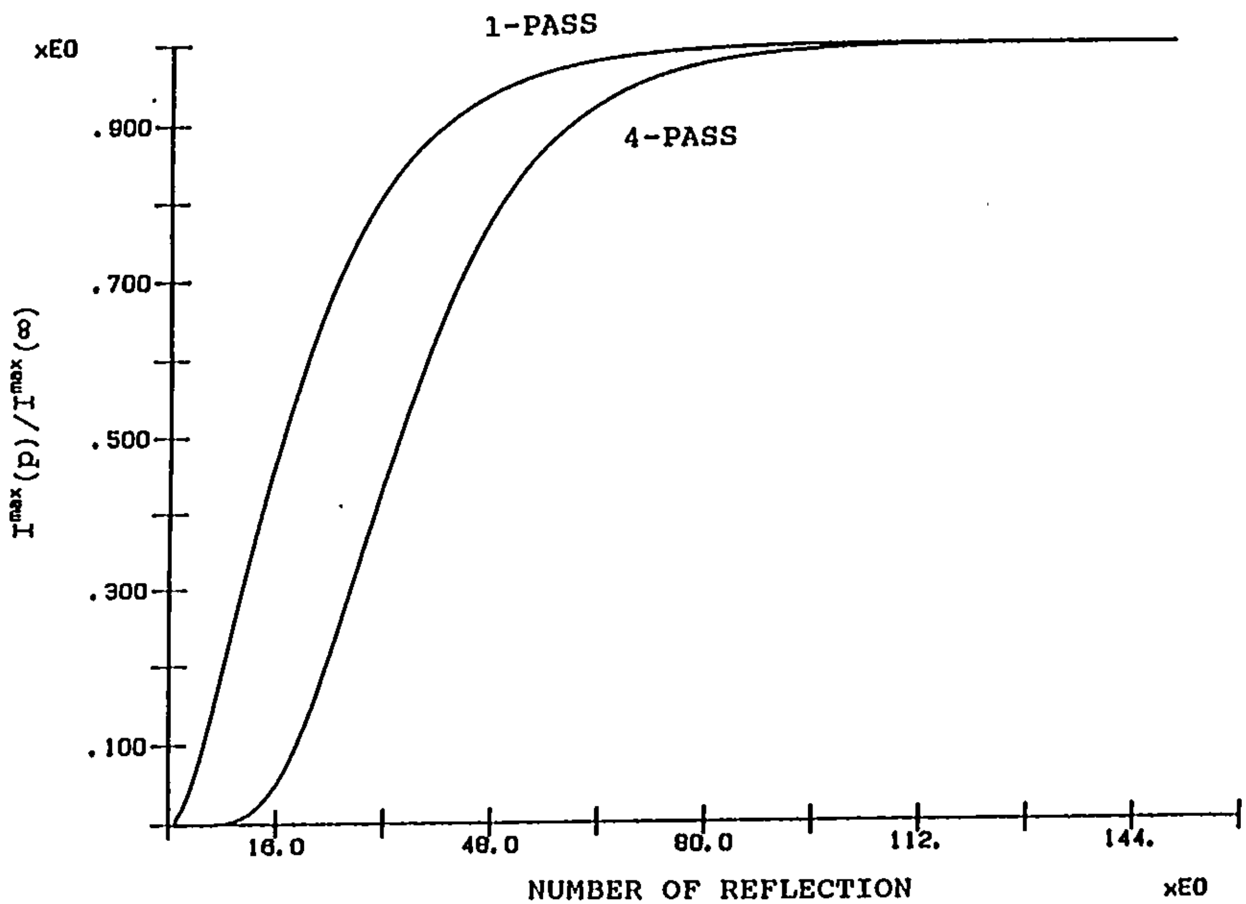

Fig. 2.5 The relative maximum intensity of transmitted light against the number of reflections

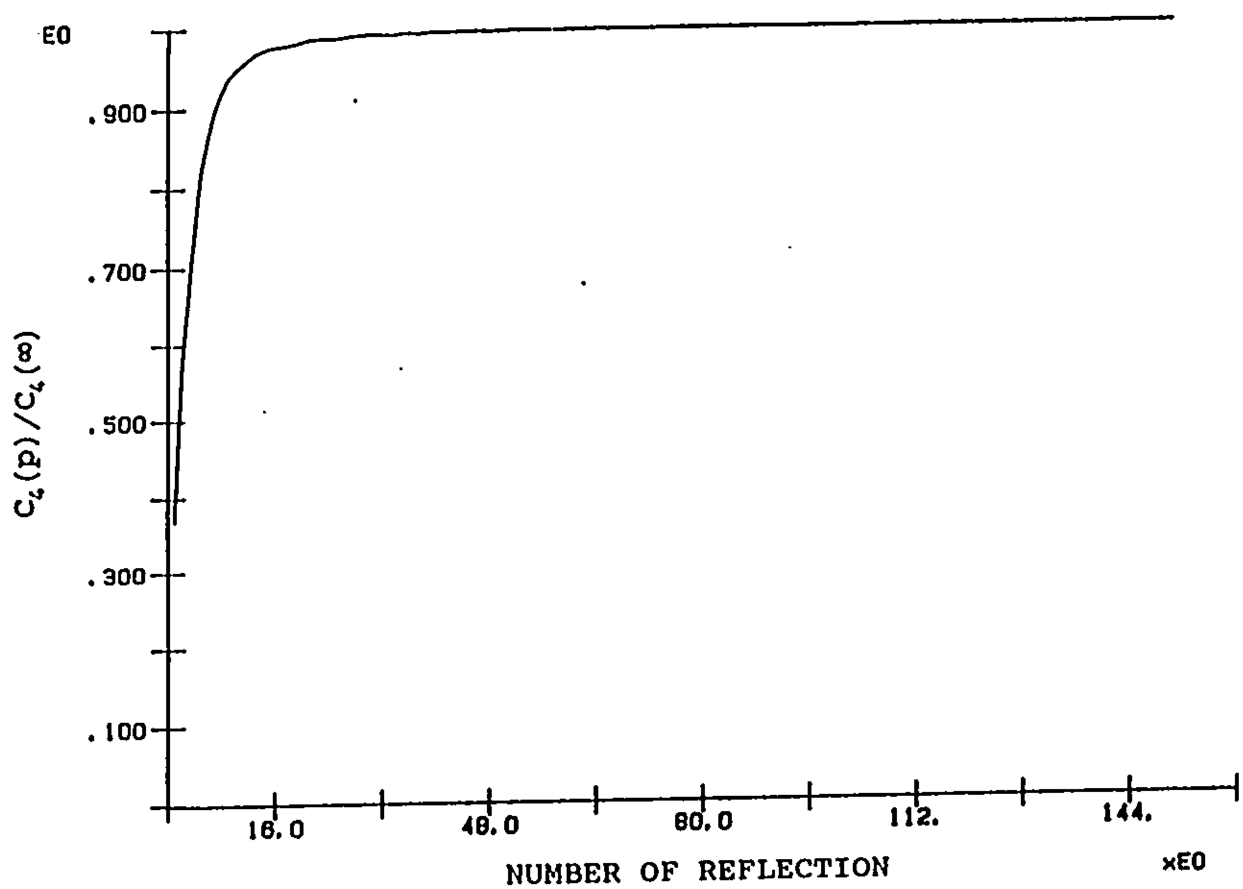

Fig. 2.6 The relative contrast against the number of reflections, resulted from 4-pass FP.

result of 4-pass FP. It can be seen that the transmitted intensity is attenuated by 10% when p=60 but it is hard to see any drop of the contrast at that value of p. It is because I^{min} drops at the same rate as I^{max} does when p decreases. Usually, θ is no larger than 0.015 radians and r is about 0.15cm. Thus, in order to get p≥60, FSR can not be less than 34GHz.

The walk-off problem will affect the experimental results:

Firstly, since p decreases with increasing angle θ, the image intensity will drop off from the centre, especially in the case of relatively small FSR. That is why even if I use uniform white light as the light source, the image may not be uniform. In that case, the intensity $I_c(\nu)$ calculated from formula (43) is not the real intensity yet and $I(R)/I_r(R)$ need to be corrected by white light intensity $I_w(R)$ again, which is obtained from the experiment using uniform white light as the light source. Then, the real intensity $I_{re}(\nu)$ will be

$$I_{re}(\nu) = \frac{I(R)/I_r(R)/I_w(R)}{2\pi R} \tag{50}$$

Secondly, the peak will be broadened by small p at small FSR, i.e. the finesse will be small. Besides that, the intensity can be quite low. All of these will make it hard to get the signal at small FSR.

2.3 Experimental Results

A typical CCD image formed by scattering from a crystal of KBr is displayed in Fig. 2.7 (Walton et al., 1992). It was obtained in the back-scattering geometry and the incident angle with the <100> axis is 15°. The central main Rayleigh peak is suppressed, and the first two rings correspond to the transverse and longitudinal phonon modes; the outermost ring is from the tail of the first ghost Rayleigh peak scattered by the edge of the iris.

The corresponding frequency spectrum is shown in Fig. 2.8. Note that the longitudinal peak, which is normally about four time larger than the transverse peak, has been diminished because we did not do the intensity correction.

In order to show the efficiency of this new method, two spectra obtained from the same sample in the 90° scattering geometry are plotted in Fig. 2.9, one using the new method with a twenty-minute exposure (upper curve), another using the conventional method with a three-hour collection time. The phonon is a T_{2g} transverse phonon, which is rather weak.

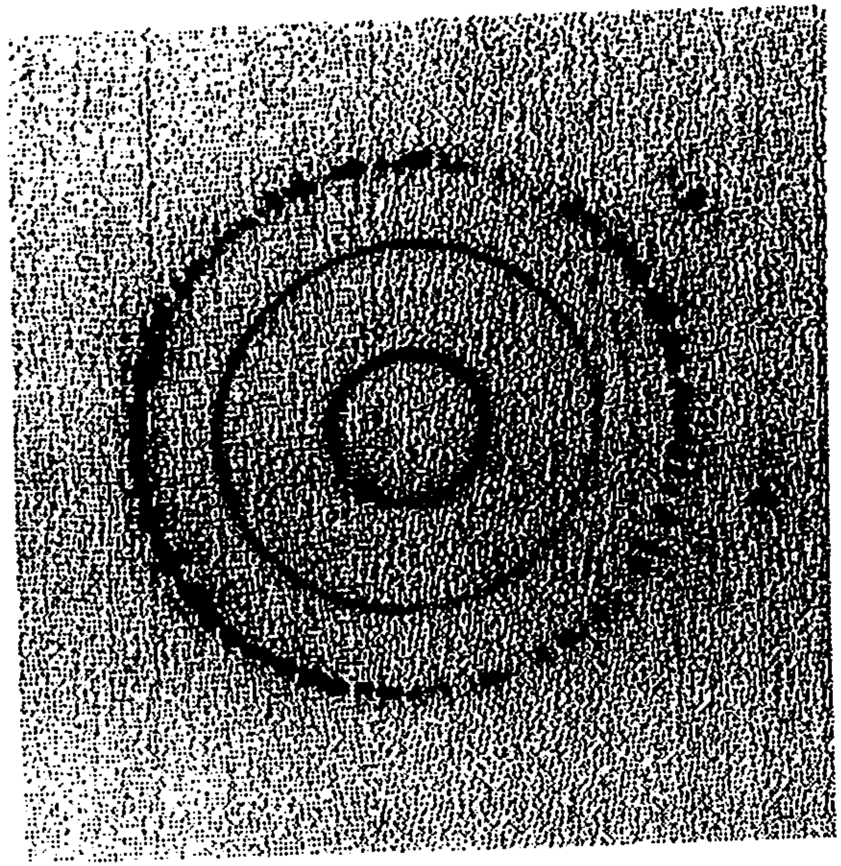

Fig. 2.7 CCD image formed by scattering from a crystal of KBr in backscattering geometry.

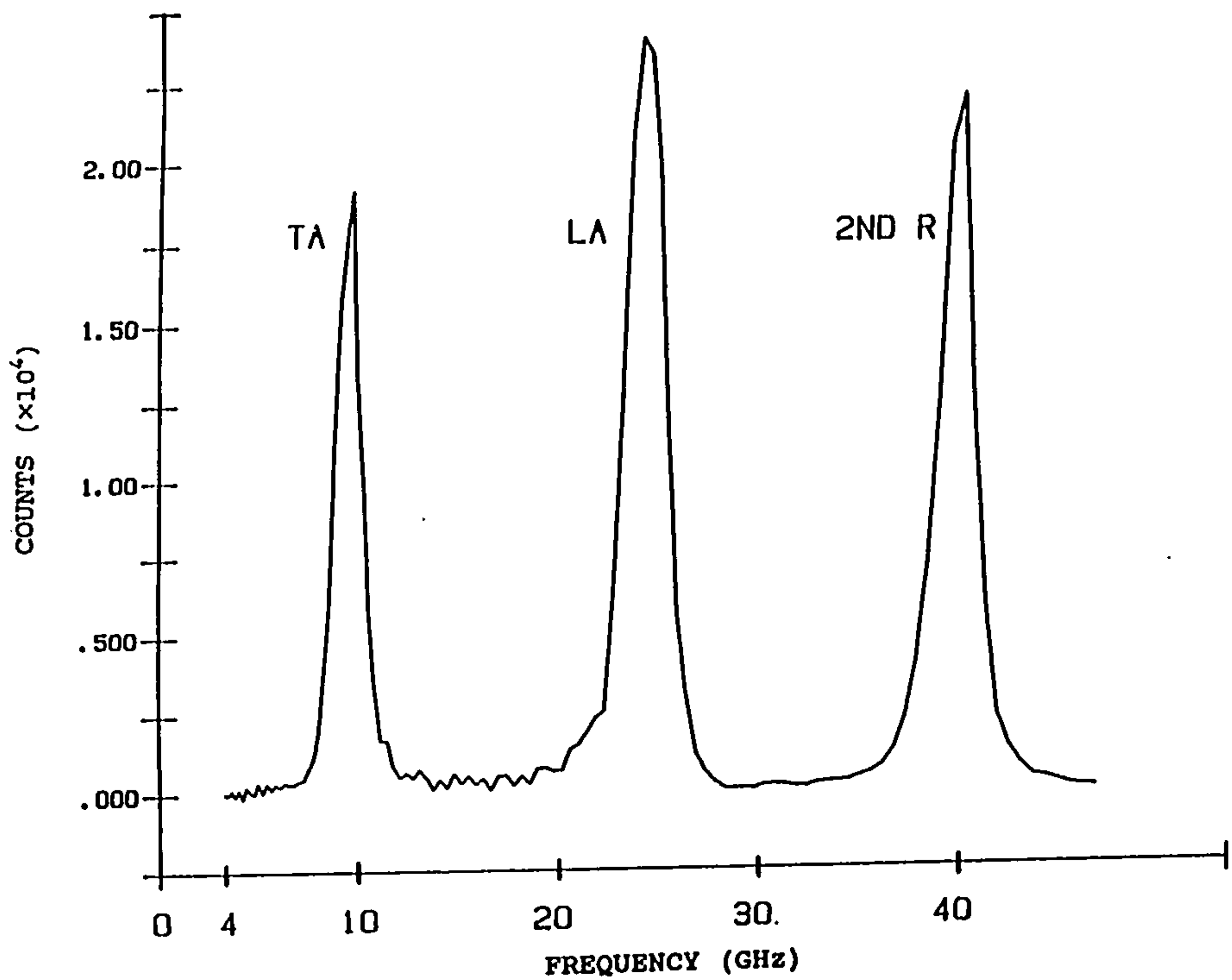

Fig. 2.8 The spectrum derived from the image of Fig. 2.7.

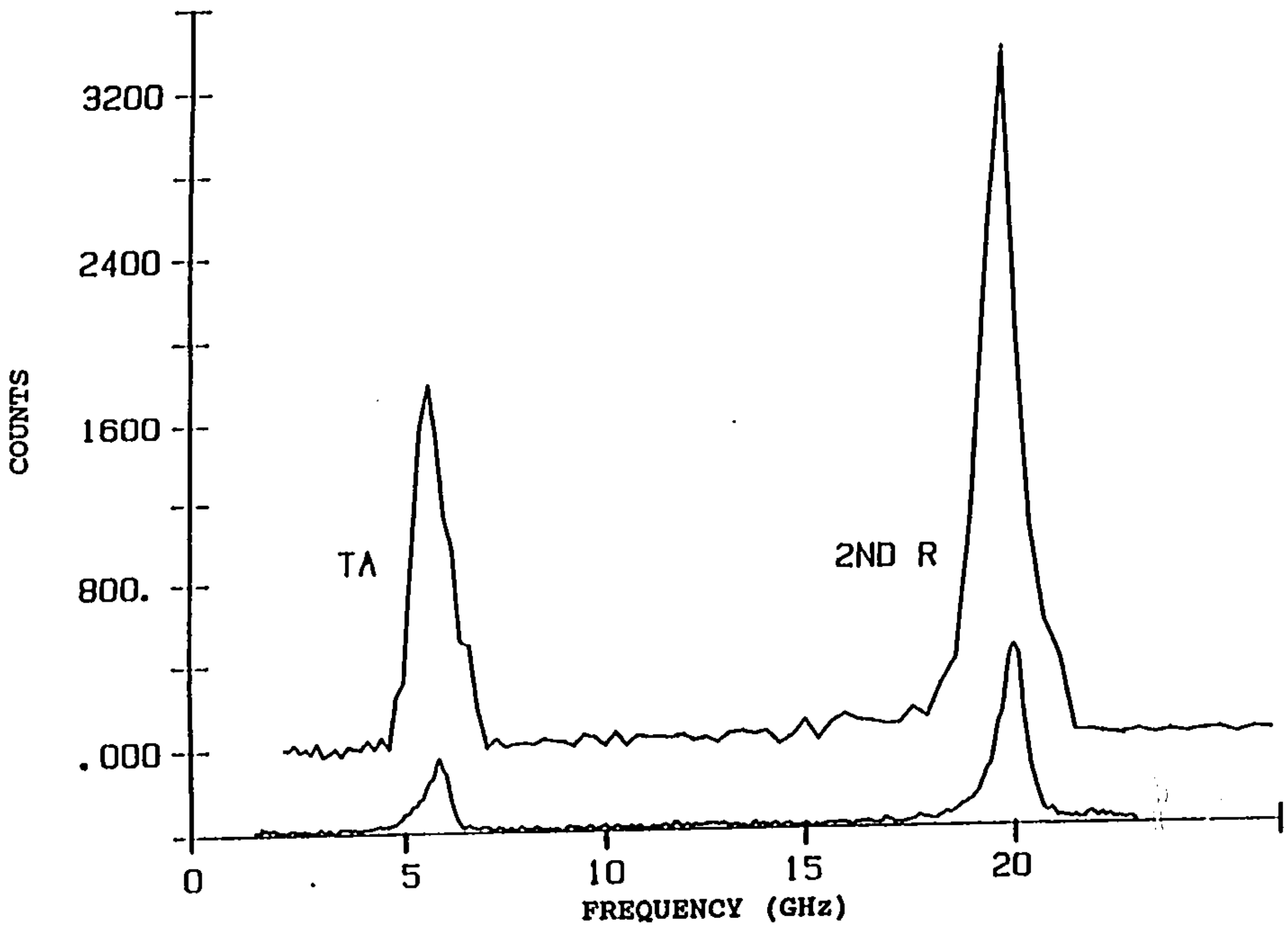

Fig. 2.9 Spectra of KBr for 90° scattering geometry: the upper spectrum is derived from a CCD image obtained with a 20-min exposure, and the lower one, offset by -400 counts, is the result of a standard FP scanning run with a 3-h collection time.

2.4 Conclusions

The CCD provides an efficient means of collecting Brillouin spectra. Its disadvantage is that it is hard to get the real intensity, hence the correct shape of the spectra. Also, since only a limited portion of the FSR is available for every exposure, it is hard to get a continuous spectrum of the whole FSR. So, the CCD is suitable for experiments to study fast changing phenomenon relating to Brillouin shift, but not suitable for those involving background, e. g. electron scattering and quasielastic scattering.

Part B

Brillouin Spectroscopy

Chapter 3

Gelatin Gel

3.1 Introduction

A gel is a jellylike binary material (Mallamace, 1992) intermediate between a solid and a liquid (Derossi et al., 1991). It consists of polymers, or long-chain molecules, cross-linked to create a tangled three-dimensional network and immersed in a liquid medium. The properties of the gel depend strongly on the interaction of these two components. The liquid prevents network from collapsing into a compact mass; the network prevents the liquid from flowing away. (Tanaka, 1981; Silberberg, 1989; Kulicke et al., 1989; Peters et al., 1989; Brinker et al., 1990). So, a gel can be viewed as a container of solvent made of a three dimensional mesh (Flory, 1957; DeGennes, 1979) (Fig. 3.2). Also, it can be viewed as a "single polymer molecule" considering that all the monomer unit in a one piece of gel are connected to each other and form one big molecule on a macroscopic scale (Shibayama, et al., 1993). Depending on chemical composition and other factors, gels vary in consistency from viscous fluids to fairly rigid solids, but typically they are soft and resilient or, in a word, jellylike.

According to the process whereby the elements of the network are connected, gels break down into two categories: chemical gels and physical gels (Guenet, 1992). In the chemical gels, the connection usually occurs through covalent bonds. In physical gels, the network structure is formed by either physical interactions from van der Walls force or by hydrogen bonds or by ionic interactions (Kuliche et al, 1989), which leads to two major consequences: (1) the conjunction domains are not point-like as in the case of chemical gels, but extend into space (conjunction zones) (2) these gels are thermoreversible since the energy involved in interactions is finite (Ross-Murphy, 1991).

Physical (or thermoreversible) gels can be made from biopolymers or synthetic polymers. Water is usually the solvent used for preparing the biopolymeric gels.

Gelatin is a neutral biopolymer. It is a water-soluble protein resulting from the partial hydrolytic degradation of collagen, which can be found in various animal tissues (skin), tendons and bones. The collagen unit is a rod of approximately 280 nm length of three strands, each one being twisted into a left-handed helix of about 0.9 nm pitch and all three being

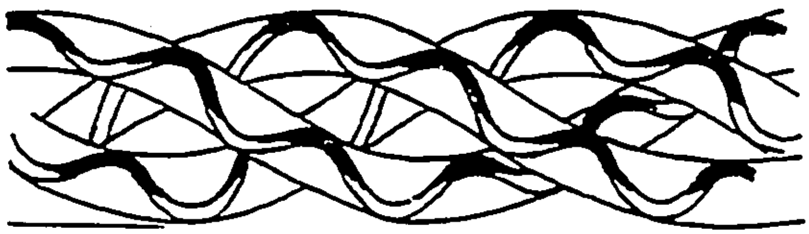

Fig. 3.1 Schematic representation of the triple helix in native collagen. Each chain adopts a left-handed helical form while the super helix is right handed.

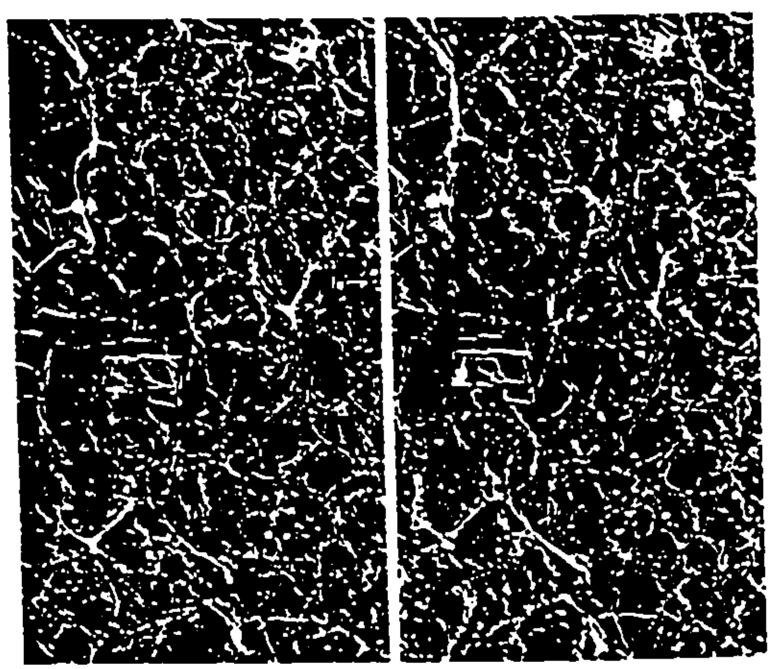

Fig. 3.2 Electron micrograph (stereoview) of a 2% (w/w) gelatin-water gel sample.

wrapped into a super-right-handed helix with a pitch of 8.6 nm (Maquet et al., 1986; Djabourov et al., 1987) (Fig. 3.1) (Clark et al, 1987). The collagen structure is stabilized by interchain hydrogen bonds which are perpendicular to the chain axes (Maquet et al., 1986).

Although the chemical formula of gelatin is complex and depends upon its origin, it always contains large amounts of proline (Pro), hydroxyproline (Hyp) and glycine (Gly) (Guenet, 1992):

Proline

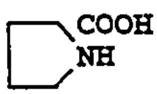

Hydroxyproline

Glycine

NH_2-CH_2-COOH

The commonest sequences are -(Gly-X-Pro)- and -(Gly-X-Hyp)-, in which X is another amino acid.

Above about 40°C, in the sol states of the gelatin-water system, the gelatin chains are believed to be in the coil conformation. When the hot solutions are cooled below about 30°C, a coil-helix transition takes place. The role of the solvent is important in the gelation mechanism, as water molecules participate in the formation of the junctions in which they are specifically oriented inside the triple helices (Pezron et al, 1991). The triple-helical junction zones cross-link the chains, and when the amount of cross-links reaches the critical number, the sol will transform into an elastic, transparent gel, which corresponds to the formation of an infinitely large three-dimensional network pervaded by the remaining liquid. An electron micrograph of a 2% (w/w) gelatin-water gel sample prepared by Escaig's method (1982) (rapid freezing followed by sublimation) was given by Favard et al. in 1989 (Fig. 3.2). The gel was matured at room temperature for one week before observation.

Gelatin gel has been used for a long time in various fields such as food, photography and pharmacy due to its remarkable mechanical properties and its natural biological origin. Gel properties have been extensively studied mechanically (Ferry, 1948; Flory et al., 1960; Macsuga, 1972; Godard et al., 1978; etc.), but only a few of those studies were done in the hypersonic frequency range using Brillouin scattering technique. For gelatin gel, as far as I know, only one paper in which this technique was involved has been published. And also only the results of the concentration-dependent experiments for low concentration solutions (Bedborough et al., 1976) were reported. In this chapter, Brillouin spectra as functions of temperature, time and thermal history for gelatin -water system at various concentrations will be reported. Some dynamic mechanical data will be given, which I think is helpful to more fully understand the viscoelastic properties of this material. Three models will be used to discuss the behaviour of the temperature and concentration dependence of the Brillouin data.

3.2 Experimental Arrangement

3.2.1 Sample Preparation

The gelatin gel (pure pigskin) used in my experiments was bought from Fisher Scientific Ltd. Its average molecular weight is about 80000.

Gel solutions with concentrations (the weight ratio of gelatin to water) from 0.01 to 0.8 were made by dispersing appropriate quantities of gelatin powder into 0.15 M NaCl solution, which had been made using distilled water. The salt solution was used because it is known that the nature of the gel is dependent upon the ionic nature of the solvent, and the presence of a significant amount of NaCl fixes the ionic force of the solution and screens out the electrostatic interactions between the charged groups of the protein chains (Djabourov et al., 1988; Silberberg, 1989), and reduces the effects of impurities (Stainsby, 1977). The mixtures were heated to not more than 60°C, and stirred at the same time until the powder was dissolved in the water completely. That temperature was maintained for some time to rid the solutions of the air bubbles. These hot solutions were adjusted to other desired temperatures for further experimentation.

3.2.2 Light Scattering System

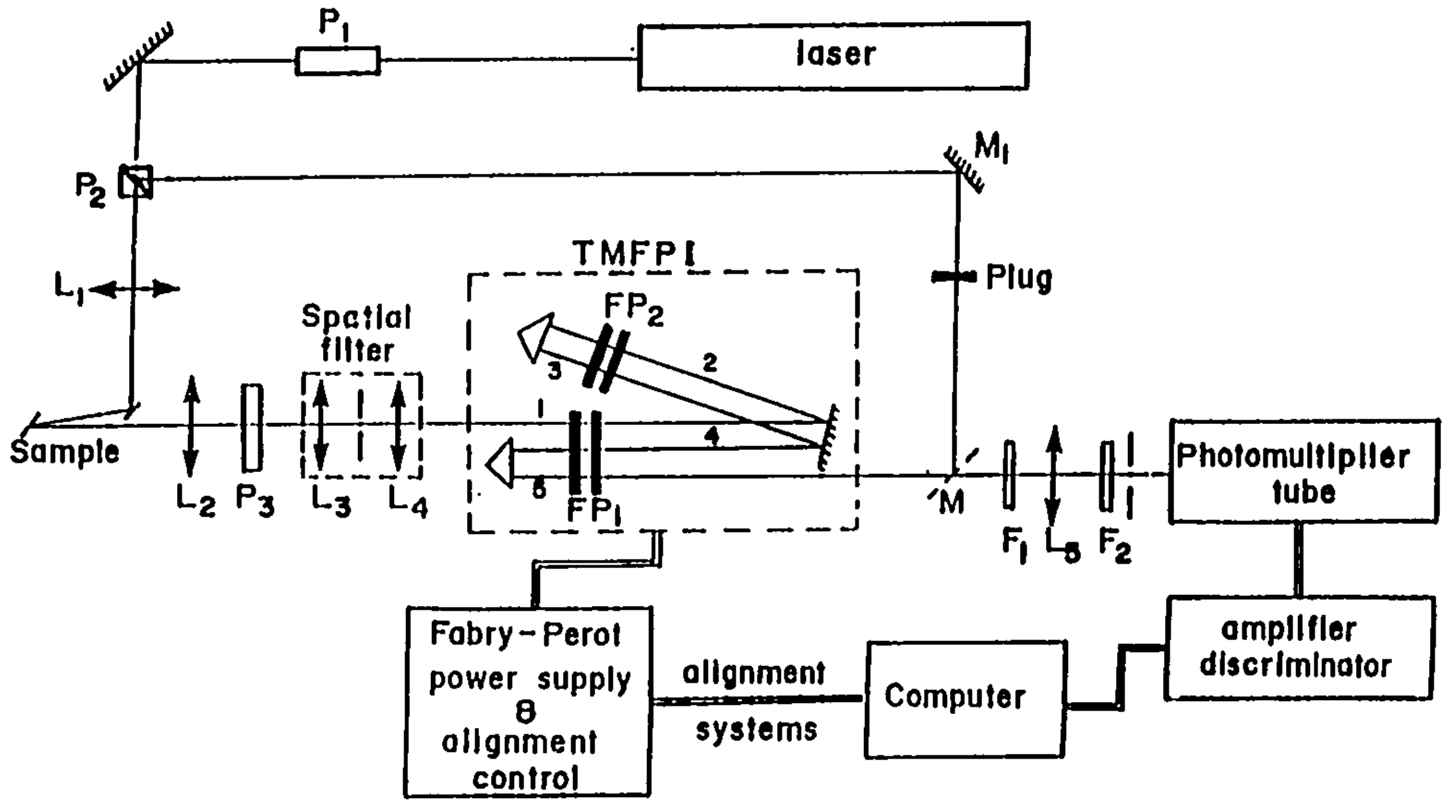

Fig. 3.3 Block diagram of experimental apparatus in gelatin gel experiment.

The Brillouin spectra were obtained with a conventional apparatus, consisting of a Coherent Innova 90-3 Argon laser operating in single mode at a wavelength of 514.5nm and 75mW power, a piezoelectrically scanned 4-pass Sandercock tandem Fabry-Perot spectrometer, and a thermoelectrically cooled photo multiplier tube as a detector (Fig. 3.3).

The experiments were performed at near back scattering geometry (about 173°). The interferometer was operated at a free spectra range of 15 GHz. The overall finesse of the complete optical system was about 40, which gave a resolution of 375 MHz. Experiments were carried out as a function of temperature, time and concentration. The broadening of the Brillouin linewidth by the optical system was corrected by deconvolution technique (Vanderwal et al., 1981). The Brillouin shift and width of the deconvolution spectrum were obtained by least-squares fitting of a Lorentzian lineshape. The error in the Brillouin shift is about 0.3% and the width is about 3%.

Besides the conventional scanning way, I used that more efficient method discussed in Chapter 2, CCD used as a detector, to check the time dependence behaviour at fast changing stage. It should be mentioned here that since the free spectra range is only 15 GHz the finesse is small. If the change is not large enough, it may not be seen clearly.

3.3 Results

Throughout the entire experiment only longitudinal phonons were observed. The failure to observe the transverse phonons indicates that the relevant Pockel coefficient is very small rather than that there were no transverse waves in this material.

3.3.1 The Influence of Time and Thermal History

Gelatin gel is thermoreversible, but the thermal history will effect its behaviour. In order to study the thermal history influence on the loss tangent, I did the time dependence experiments in two ways: 1) approaching the experiment temperature from above and 2) from below, which, for simplicity, will be referred to as the cooling process and the warming process respectively. In the cooling process, the samples at about 60°C were allowed to cool in air to room temperature about 22°C. In the warming process, the samples at ~60°C were quenched in ice-water and left there overnight, then removed from the water bath, and allowed to warm up in air to room temperature. Both methods required about 20 minutes to reach the temperature equilibrium state. The temperature variation with the time is shown in Fig. 3.4.

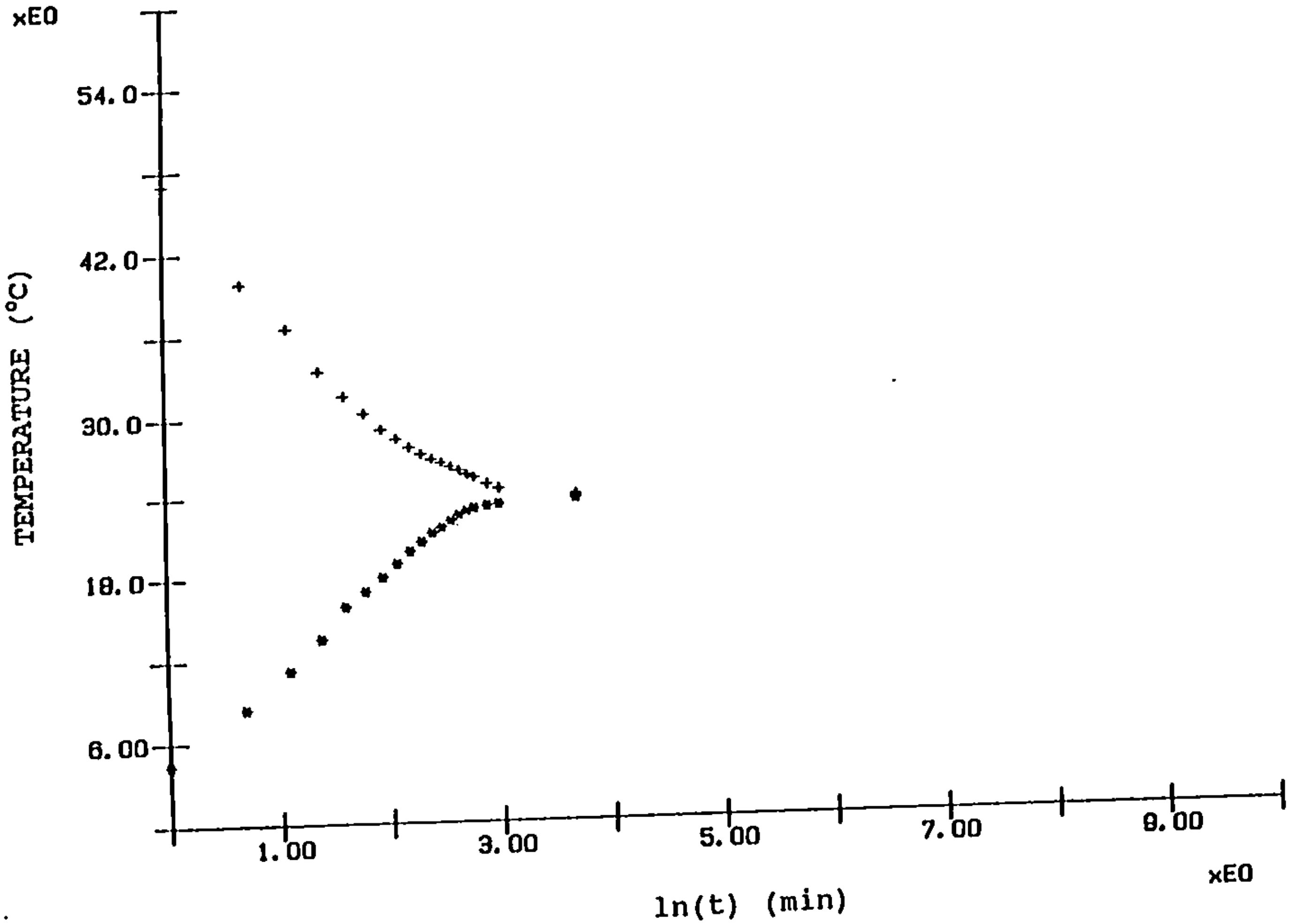

Fig. 3.4 Temperature behaviour as a function of time.

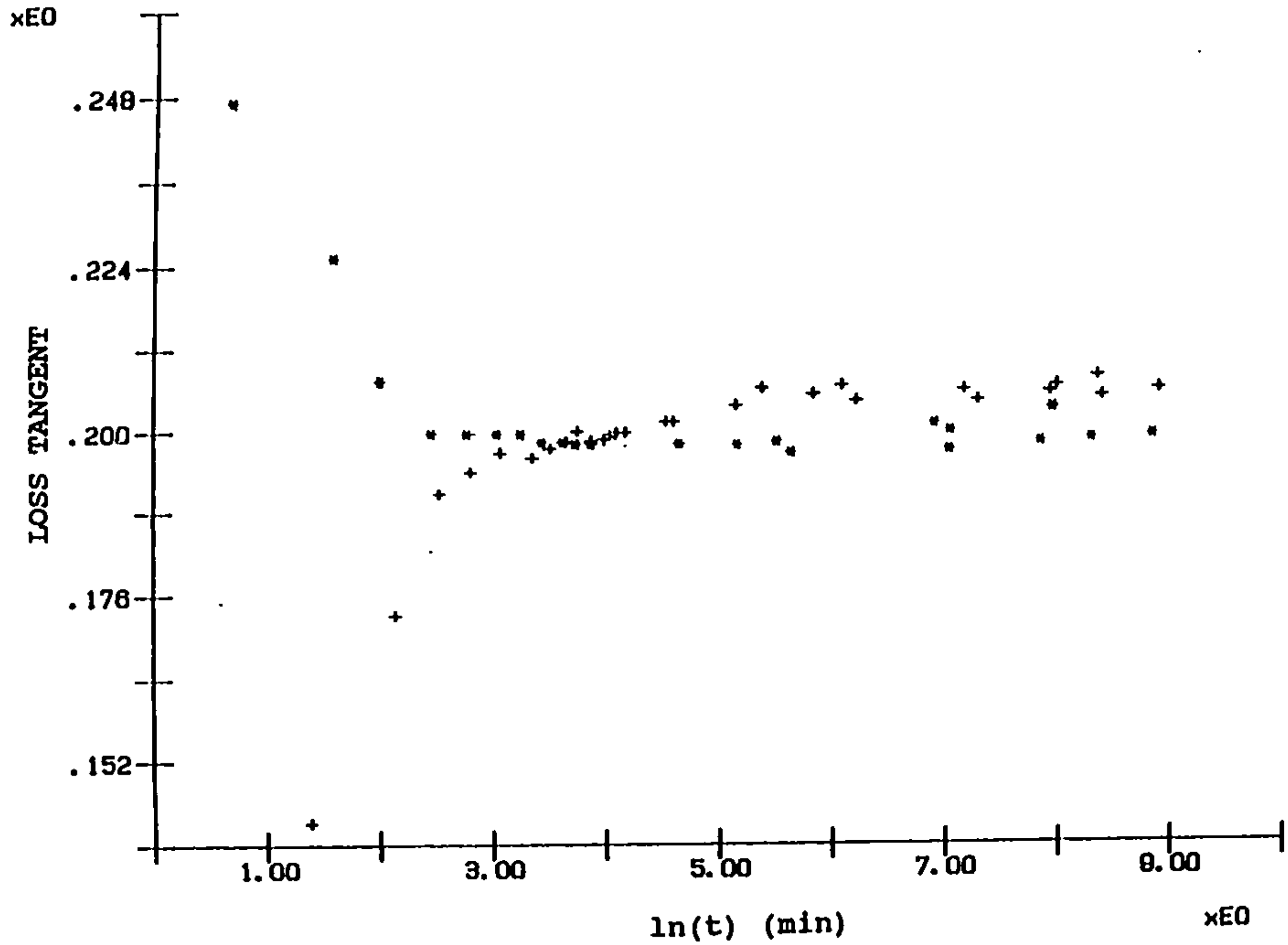

Fig. 3.5a Mechanical loss tangent as a function of time: c=0.6, * and + represent the warming process (0°C → 22°C) and the cooling process (58°C → 22°C), respectively.

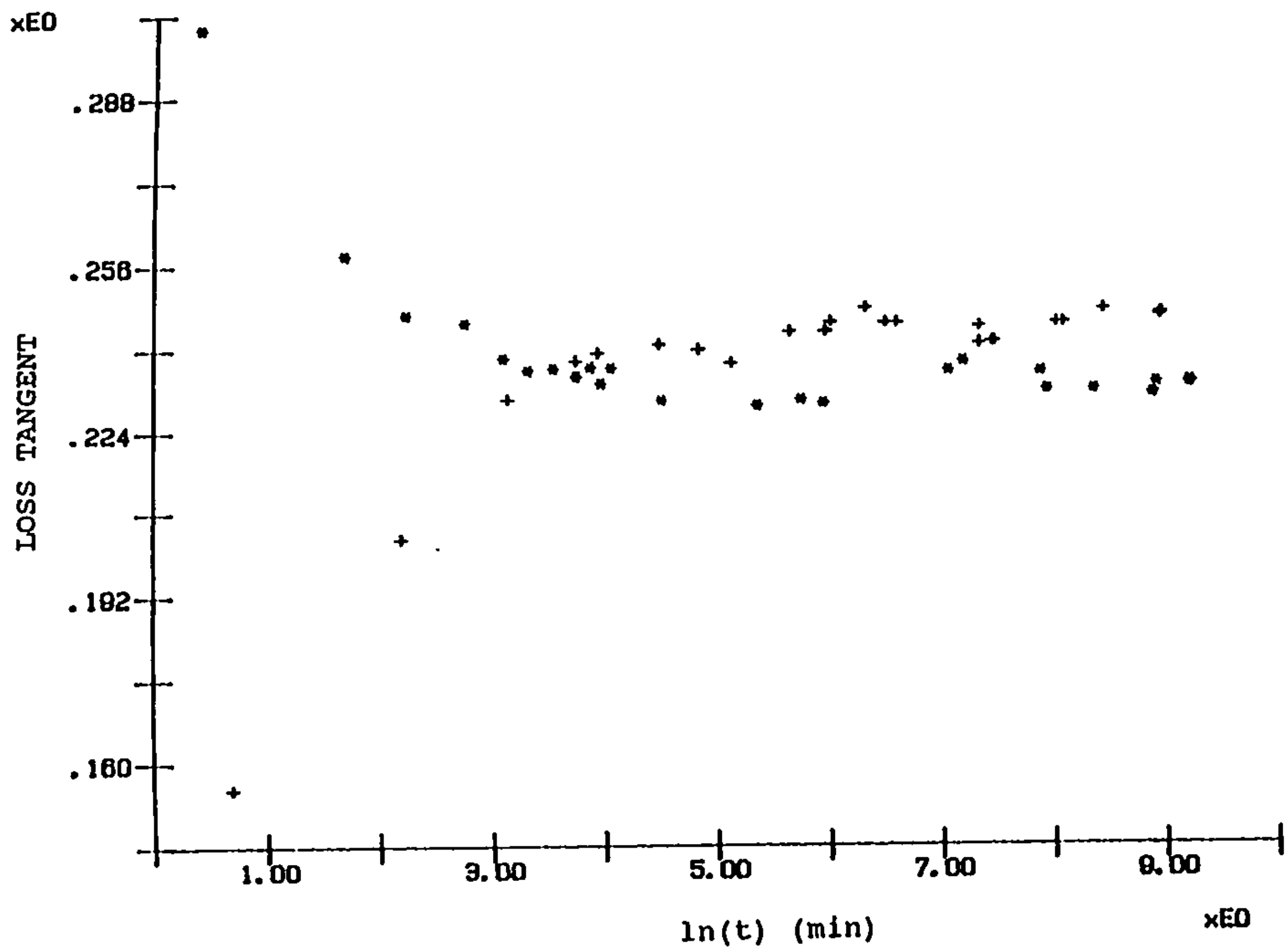

Fig. 3.5b Mechanical loss tangent as a function of time: c=0.8, * and + represent the warming process (0°C → 22°C) and the cooling process (60°C → 22°C), respectively.

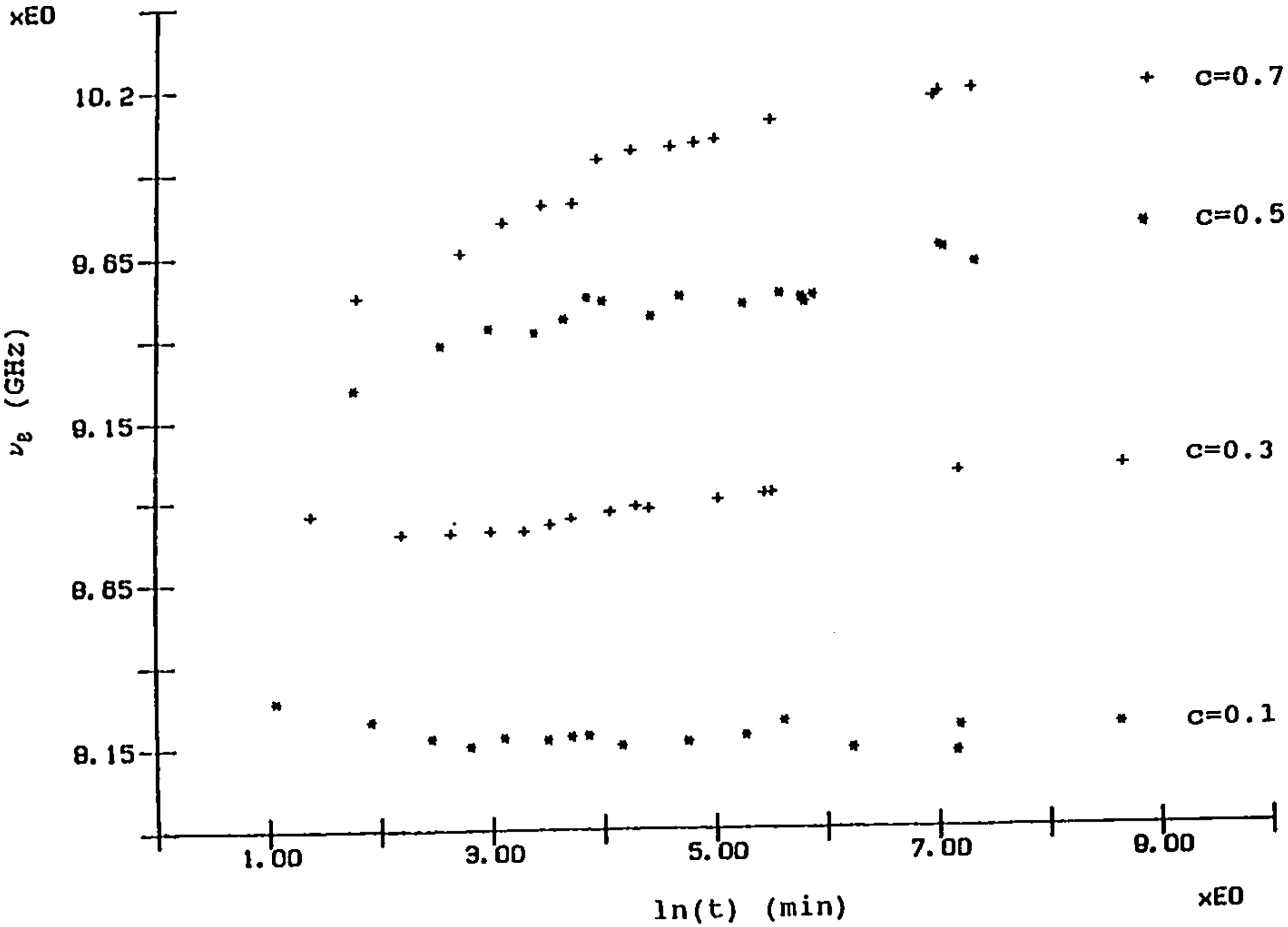

Fig. 3.6 Time dependence of the Brillouin shift in gelation process (60°C → 22°C).

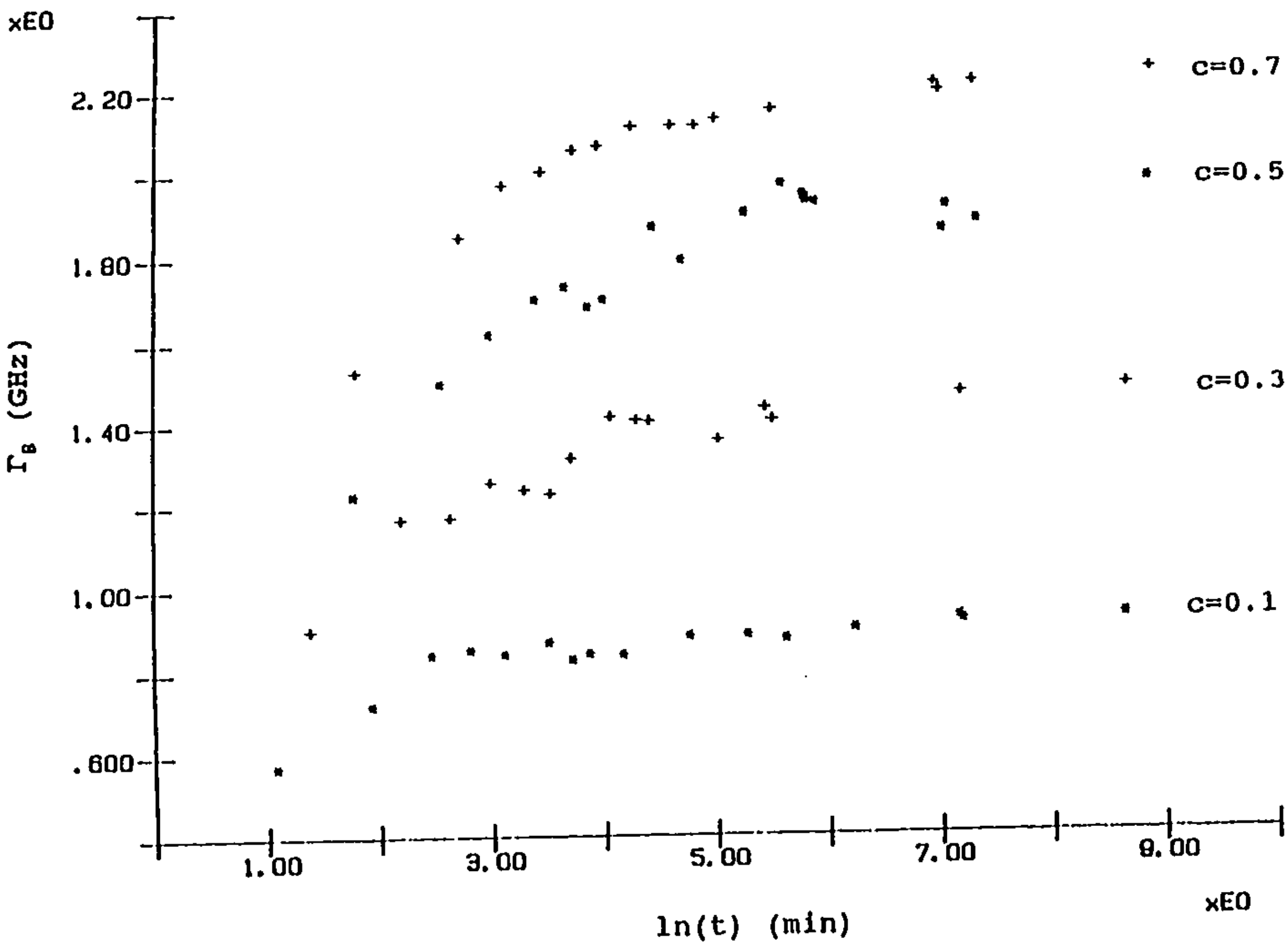

Fig. 3.7 Time dependence of the width in gelation process (60°C → 22°C).

Fig. 3.5 shows the curves of $tg\theta$ versus $\ln(t)$ for concentrations of 0.6 and 0.8. From these graphs, we can see that after the 20 minutes required to reach temperature equilibrium, the loss tangent still decreases with time in the warming process and increases in the cooling process (which is really a gelation process since the experiment temperature is below the gel point T_g). The two curves of these two processes intersect after about half an hour, and when approaching the equilibrium state, the loss tangent of the cooling process is larger than that of the warming process. This behaviour can be seen for other concentrations (refer to Figs. 3.8 and 3.9) so I think it is real, not because of the experimental error even though the difference is small.

The gelation results for various concentrations are shown in Fig. 3.6 and Fig. 3.7. The decrease of ν_B at the beginning of gelation in the low concentration case is caused by the temperature changing. It can be seen that (a) after about half an hour when the gelatin-water system was already in the gel state, ν_B and Γ_B are still increasing for C=0.5 and 0.7 sample, but almost not for c=0.1 sample; and (b) the larger the concentration the bigger the eventual value.

The behaviour of these curves is similar to those resulting from mechanical experiments (Ferry, 1948). However, the influence of thermal history on the essentially constant values of ν_B and Γ_B are different. From the mechanical

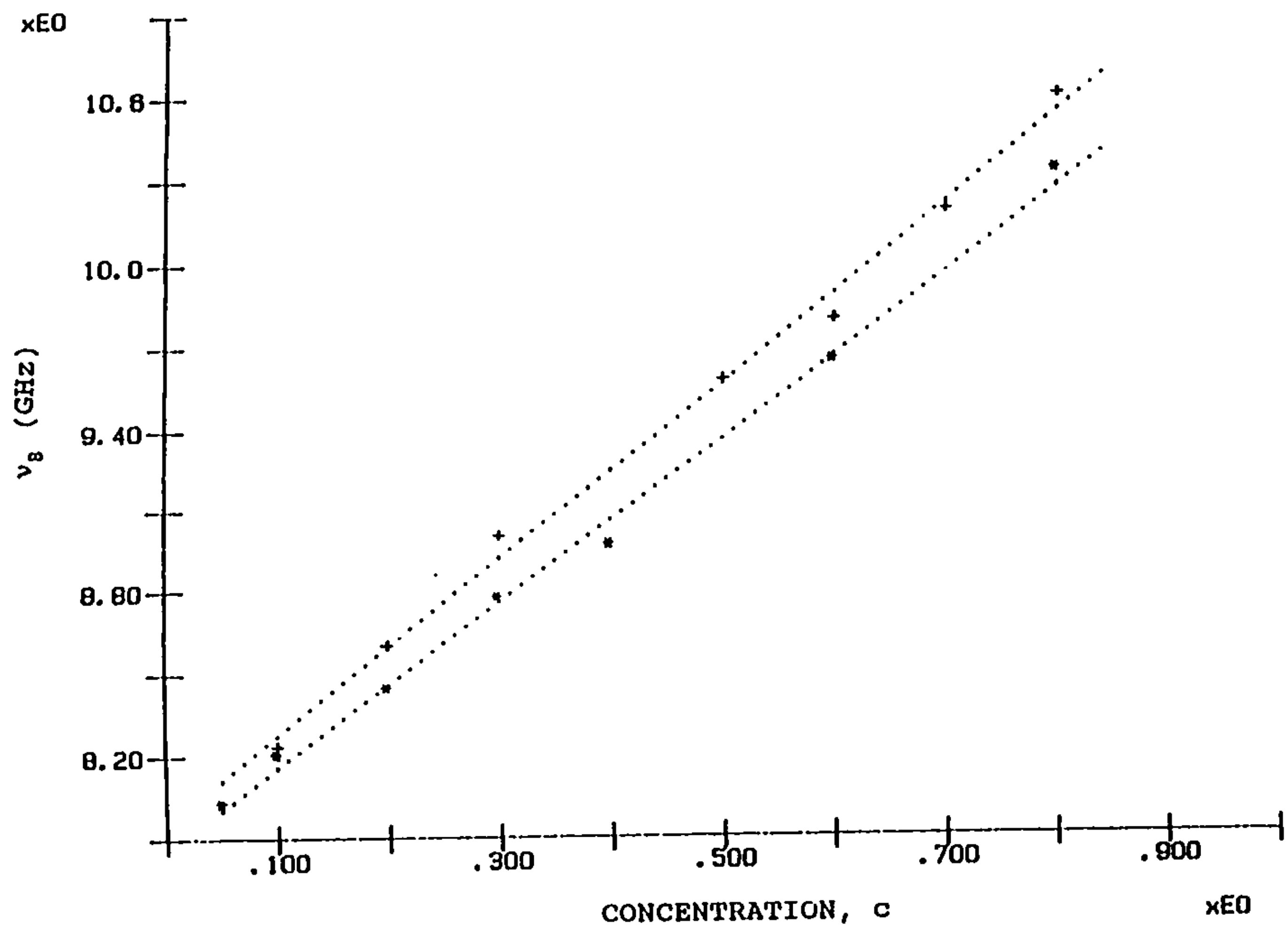

Fig. 3.8 The essentially constant values of the Brillouin shift at 22°C. * and + represent the results from warming and cooling processes, respectively. The dotted lines are the best fitting curves.

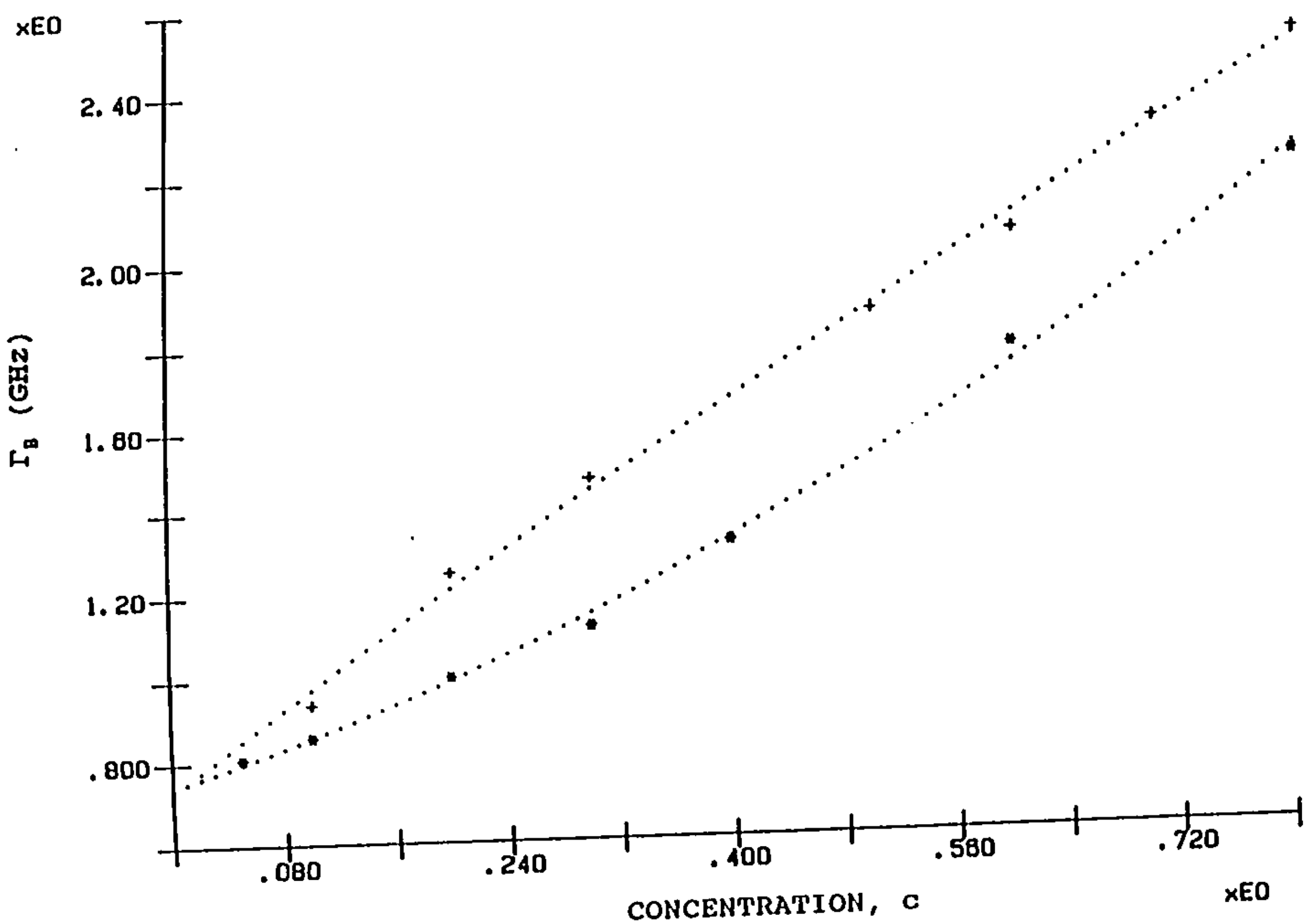

Fig. 3.9 The essentially constant values of the width at 22°C. * and + represent the results from warming and cooling processes, respectively. The dotted lines are the best fitting curves.

experiment, the rigidity of the warming process is always larger than that of the cooling process even after fifty hours. My results show both v_B and Γ_B of the cooling process are larger than those of the warming process (Figs. 3.8 and 3.9, in which the dotted lines are the best fitting curves). Also, the difference between the two processes increases with the concentration. My results agree with Bedborough and Jackson's result about Γ_B, but differ from theirs about v_B which did not show this difference. I think my results are reasonable if we remember the two processes have different cooling rates.

The sample gelatin solution in the warming process was cooled down very rapidly before being warmed up. This fast cooling "froze" the molecules in the configuration they had immediately prior to chilling and the gel had small crystalline regions. On the contrary, the solution in the cooling process was cooled naturally in the air at a relatively slow speed, which gave the polymer chains in the solution more chance to contact each other to form links, and the crystalline regions were bigger, which caused the larger values for v_B and Γ_B.

To get rid of the temperature influence and also to study the influence of the cooling rate on the fast changing stage, I cooled the sample of about 60°C to room temperature quickly (about 1.5 minute) and used the CCD' method to study the fast changing stage of the gelation process. I did the exposure every minute. The radius of the ring is related to the Brillouin shift and there is no obvious change of the size of the rings with time. There are two possibilities which can cause this result: (a) the fast quenching "froze" the molecules and made the change small; (2) the resolution of the equipment is not high enough to observe the change, especially when the phonon peak is broad.

3.3.2 Temperature Dependence

The solutions at about 60°C were quenched in ice-water overnight before increasing the temperature in steps, from about 2°C to 61°C. At every step, samples were maintained at that temperature at least four hours before doing the experiment. According to the previous section, the Brillouin shift ν_B and width Γ_B shown in figures 3.10 and 3.11 are the essentially constant values at individual temperatures. It was found that

— for dilute solutions ν_B increases monotonously with T, as water does in that temperature region (O'Connor et al., 1967);

— for condensed solutions, ν_B decreases at first, and then becomes approximately constant;

— for intermediate concentrated (with c between 0.2 and 0.3) solutions, ν_B is more or less independent of temperature;

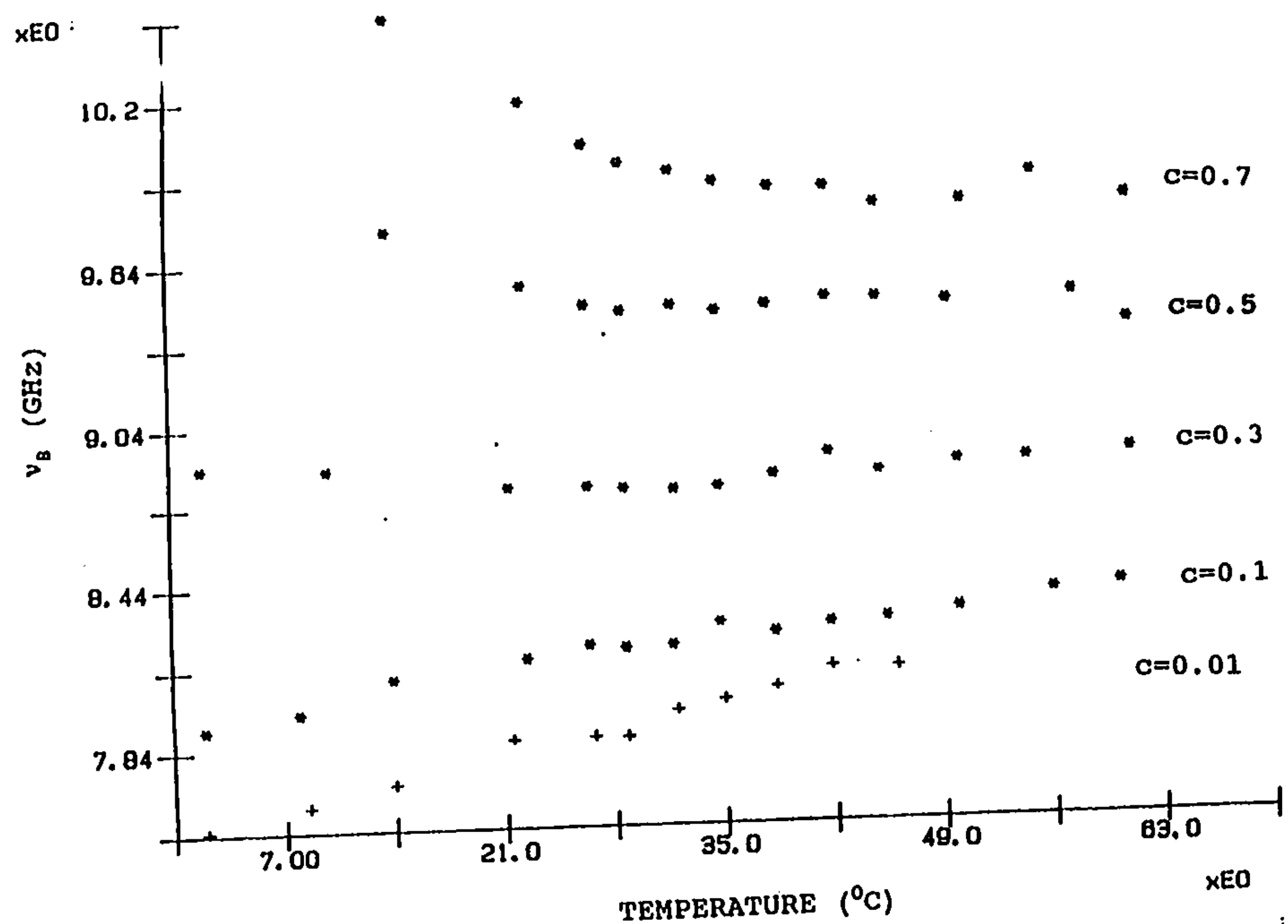

Fig. 3.10 Temperature dependence of the Brillouin shift.

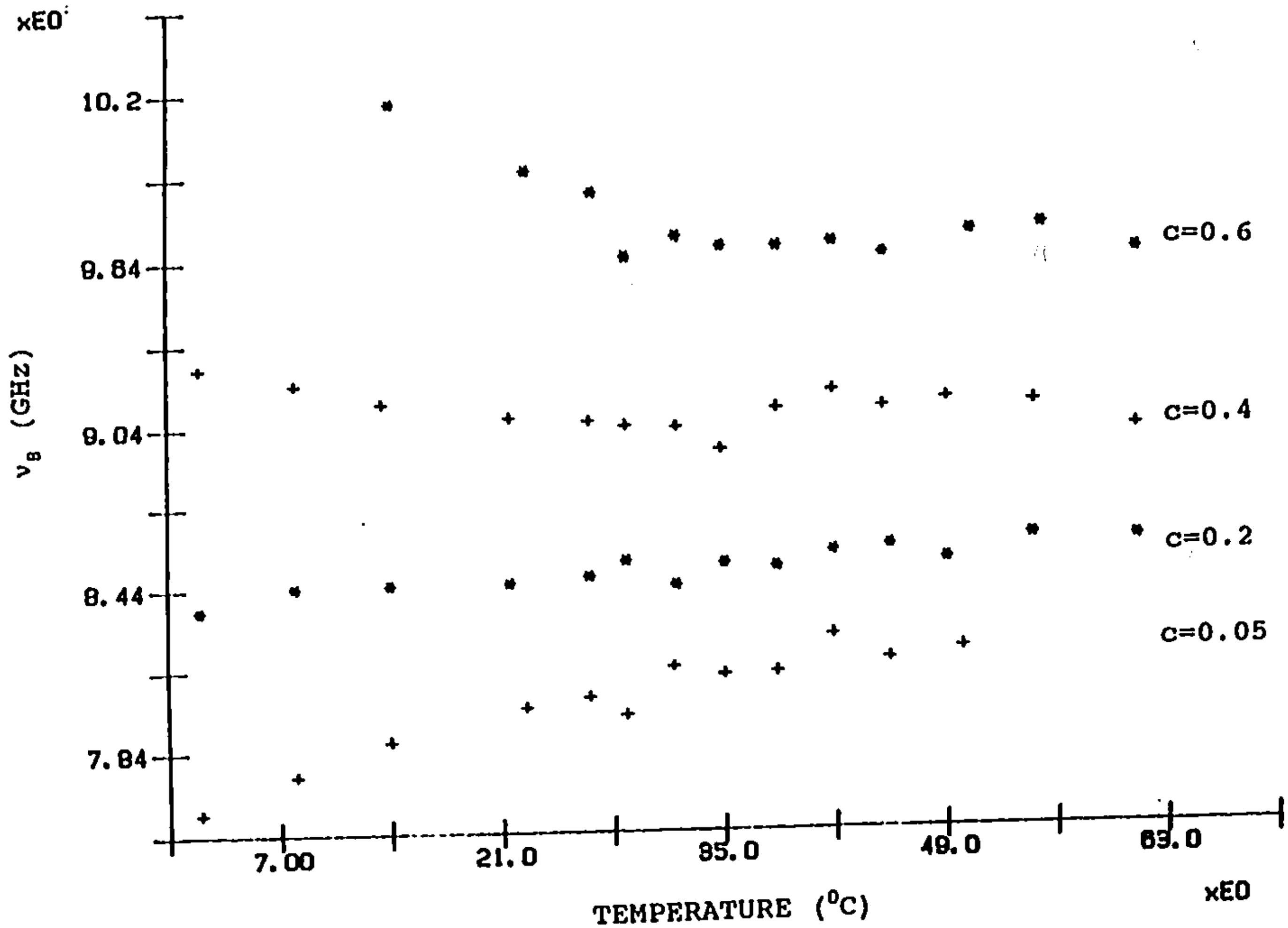

Fig. 3.10 Temperature dependence of the Brillouin shift.

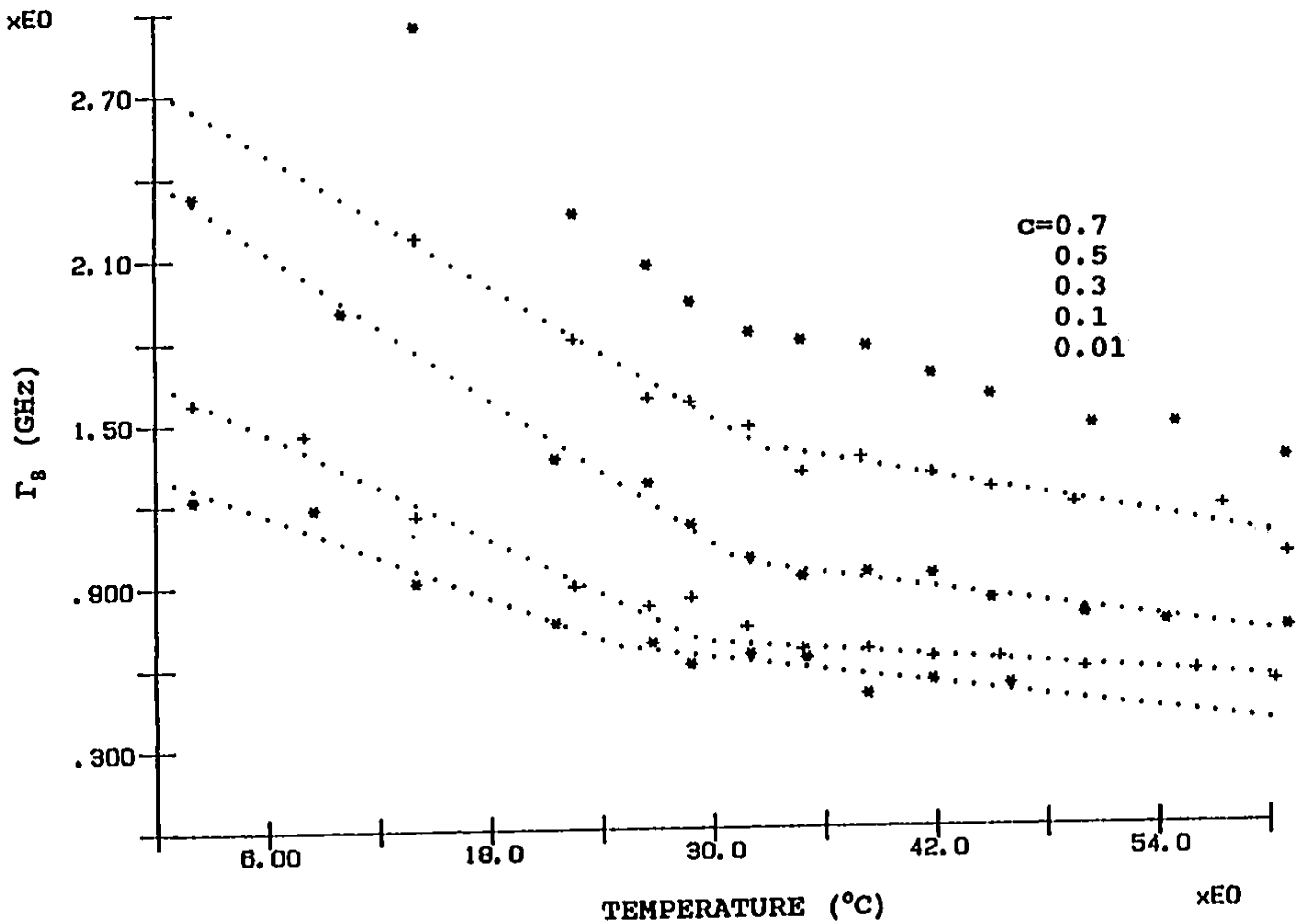

Fig. 3.11 Temperature dependence of the width. The dotted lines are the fitting curves.

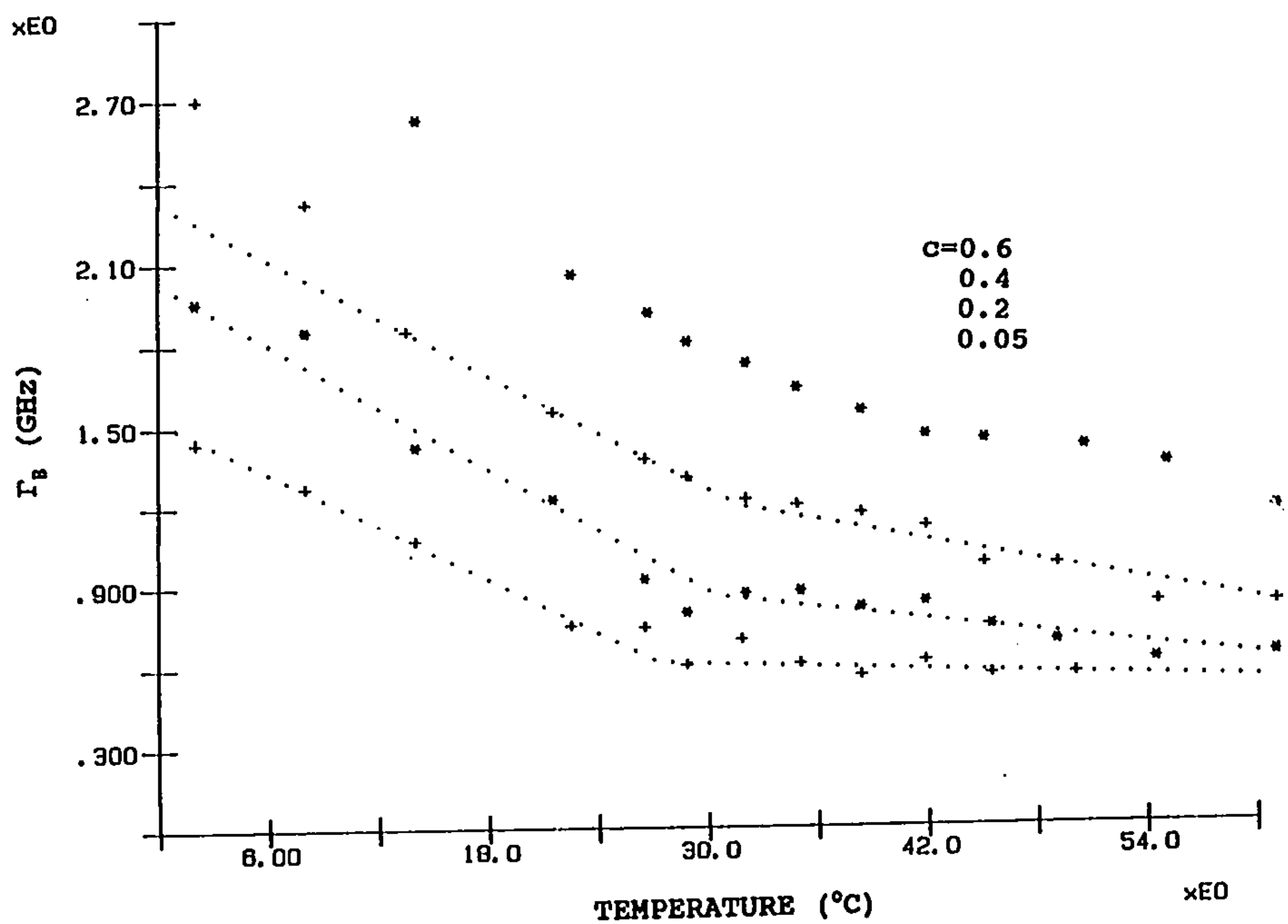

Fig. 3.11 Temperature dependence of the width. The dotted lines are the fitting curves.

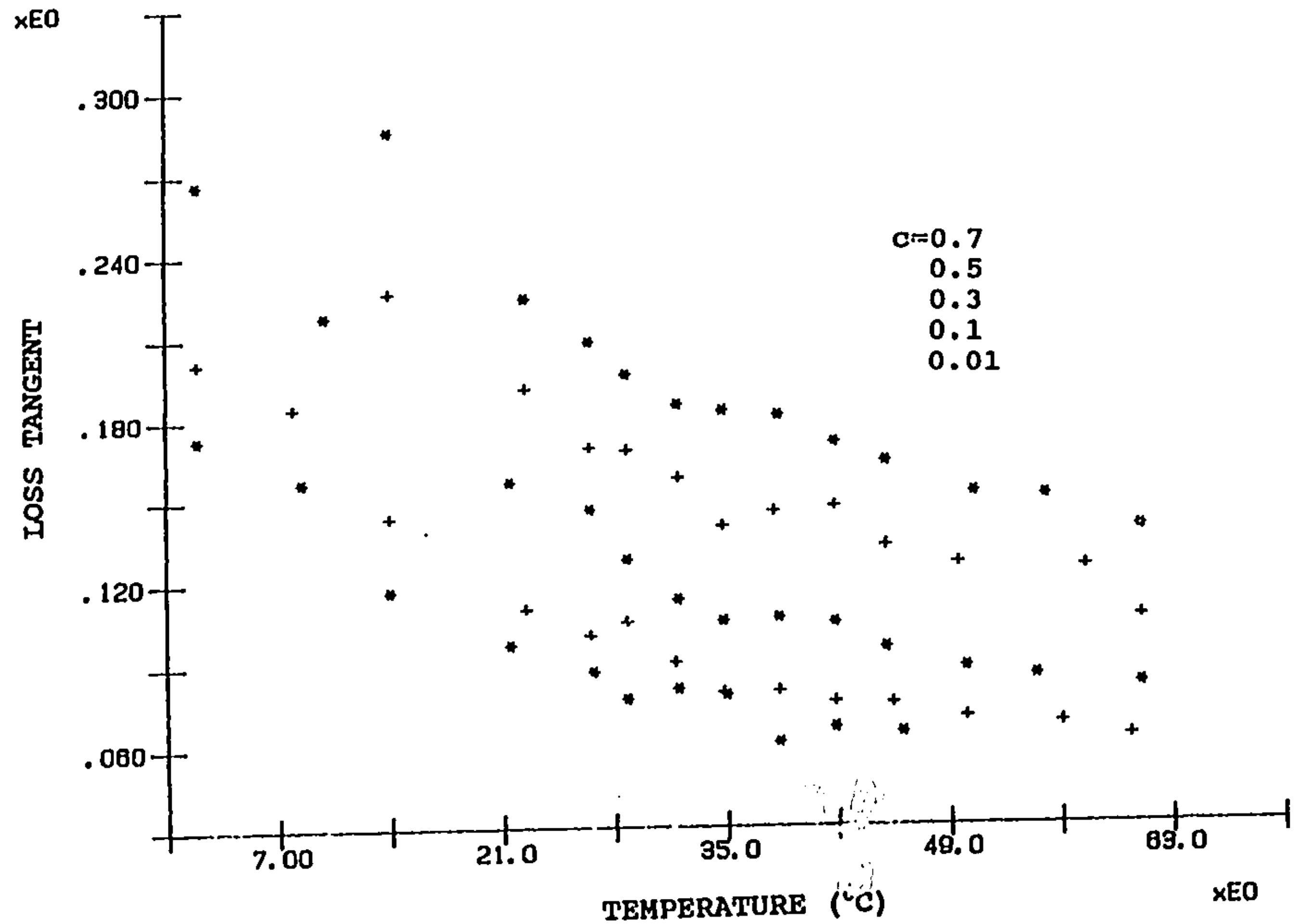

Fig. 3.12 Mechanical loss tangent an a function of temperature.

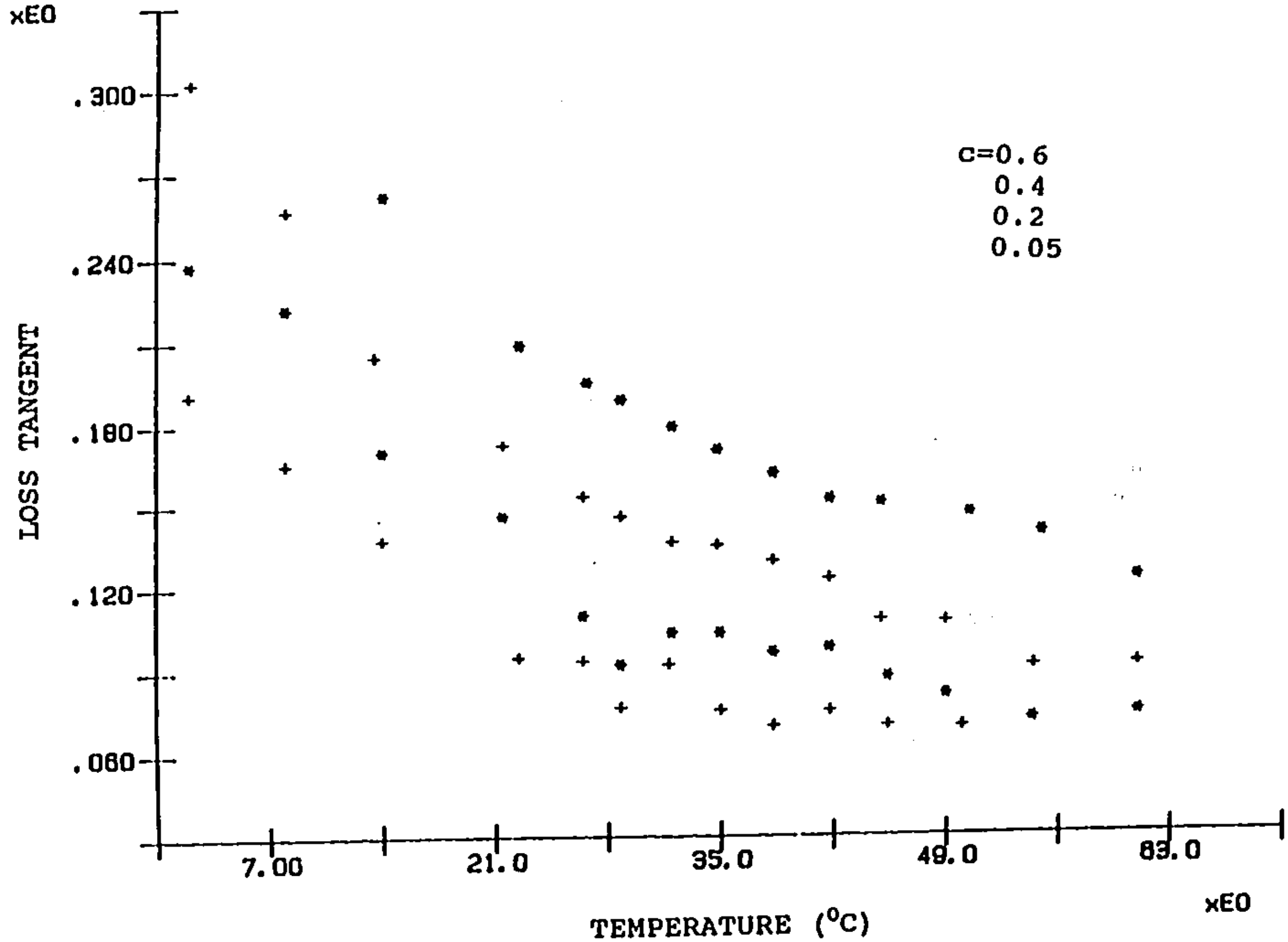

Fig. 3.12 Mechanical loss tangent as a function of temperature.

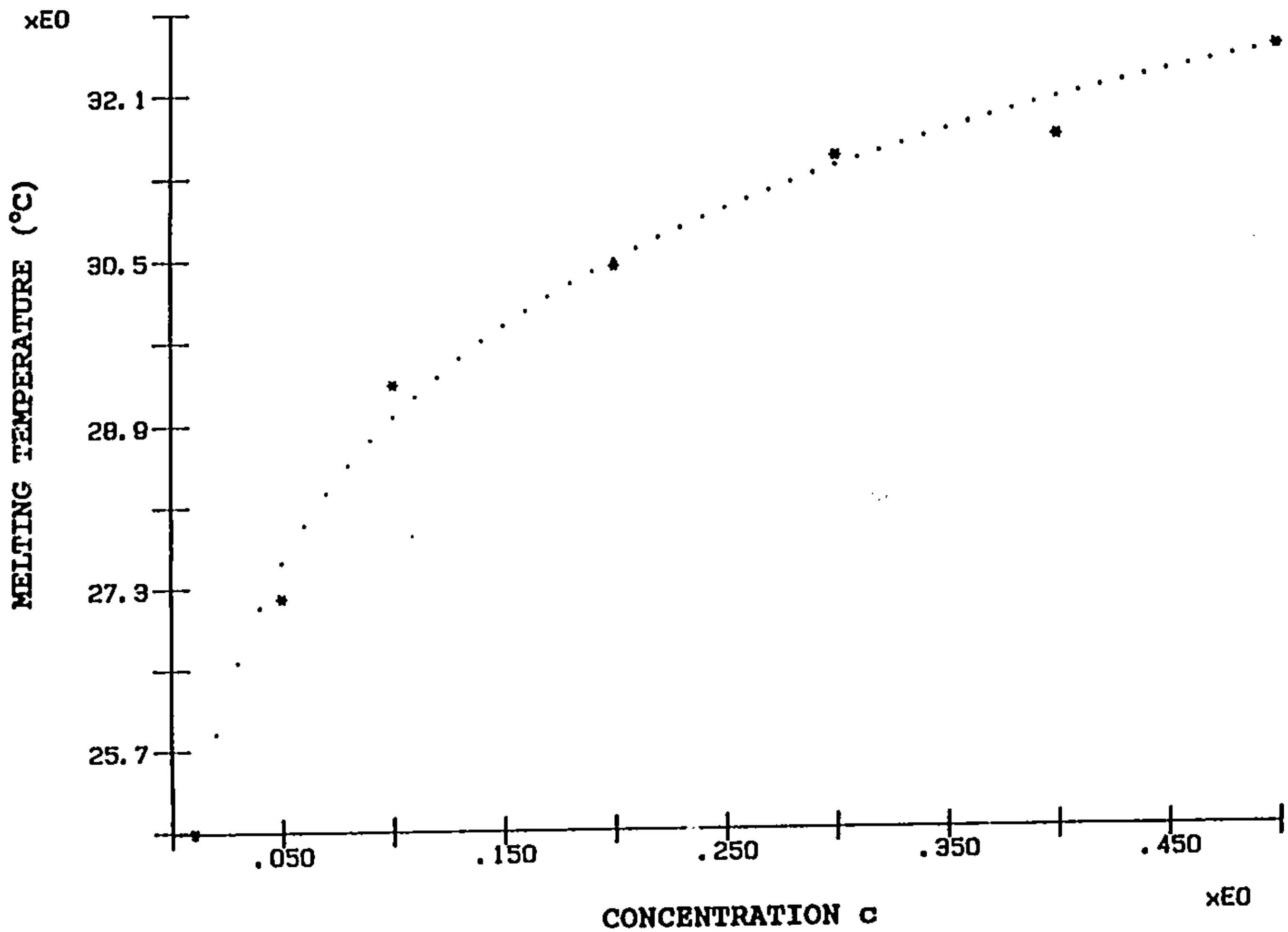

Fig. 3.13 Phase diagram. The dotted line is the fitting curve.

— at the same temperature, the higher the concentration, the larger the shift.

As to the width, no matter how much the concentration is, Γ_B decreases with increasing temperature, and at the same temperature, the higher the concentration, the larger the width.

When the concentration is not too high, Γ_B decreases almost linearly with temperature and a change in slope occurs at certain temperature. The first part of the curve must correspond to the gel state, and the change in slope signals the transition to the sol state. So, the temperature at which the slope changes can be treated as "melting" temperature T_m as Ng's group did (1984, 1985a). T_m is concentration dependent, from which the phase diagram can be obtained (Fig. 3.13).

The temperature dependence of the loss tangent is shown in Fig. 3.12. The general feature of these curves are similar to those of Γ_B except that the slopes are different. The slope at gel state is larger than that at sol state, which indicates there is an extra mechanical loss tangent in the gel state.

Fig. 3.14 and Fig. 3.15 show the temperature dependence of storage modulus M' and loss modulus M". The refractive indexes I used (listed in Table 3.1) were measured at room temperature by refraction and using Snell's law. Their change with temperature is hard to see. The curves M' and M" have the behaviour similar to ν_B and Γ_B, respectively.

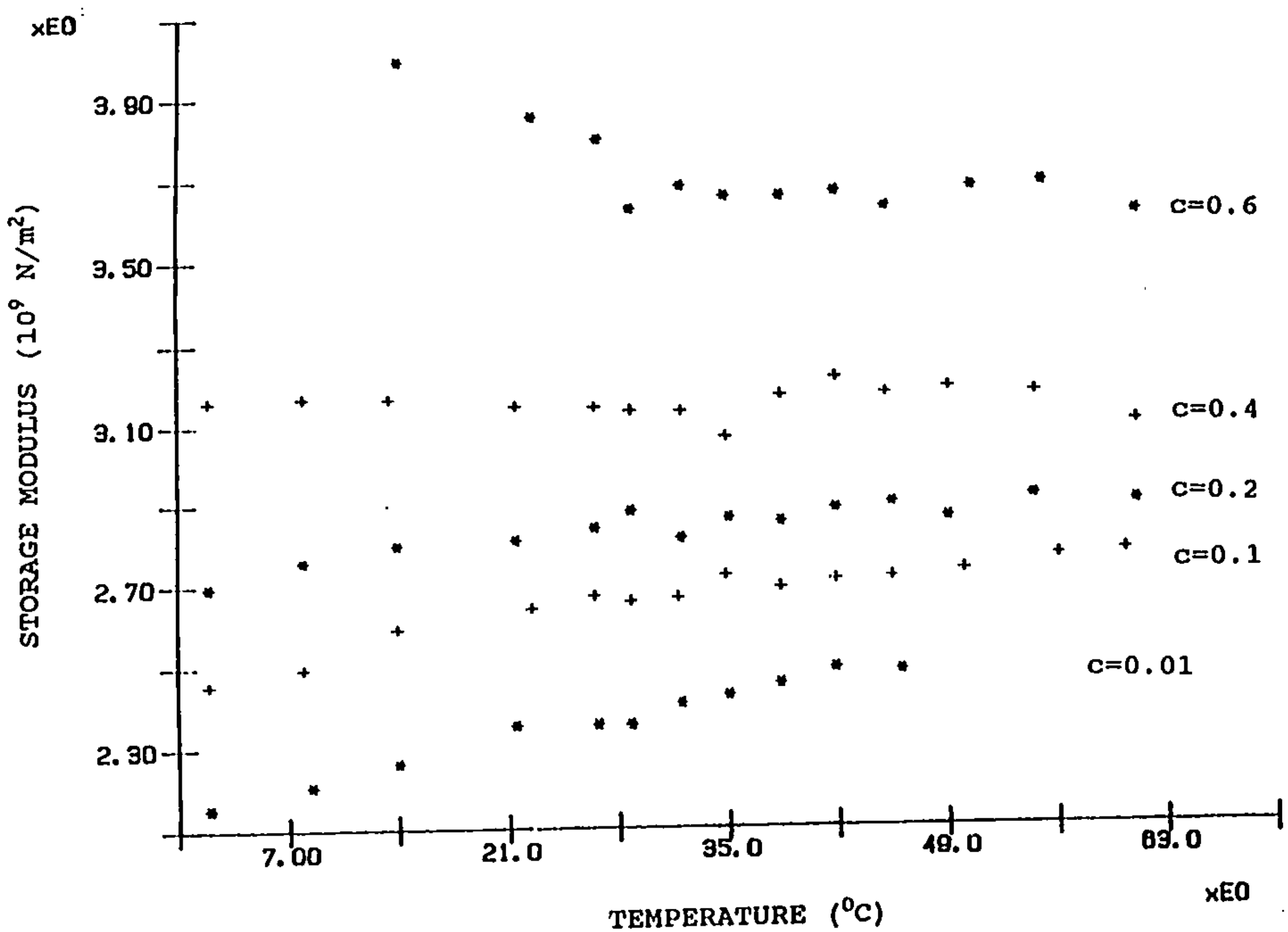

Fig. 3.14 Temperature dependence of longitudinal storage modulus.

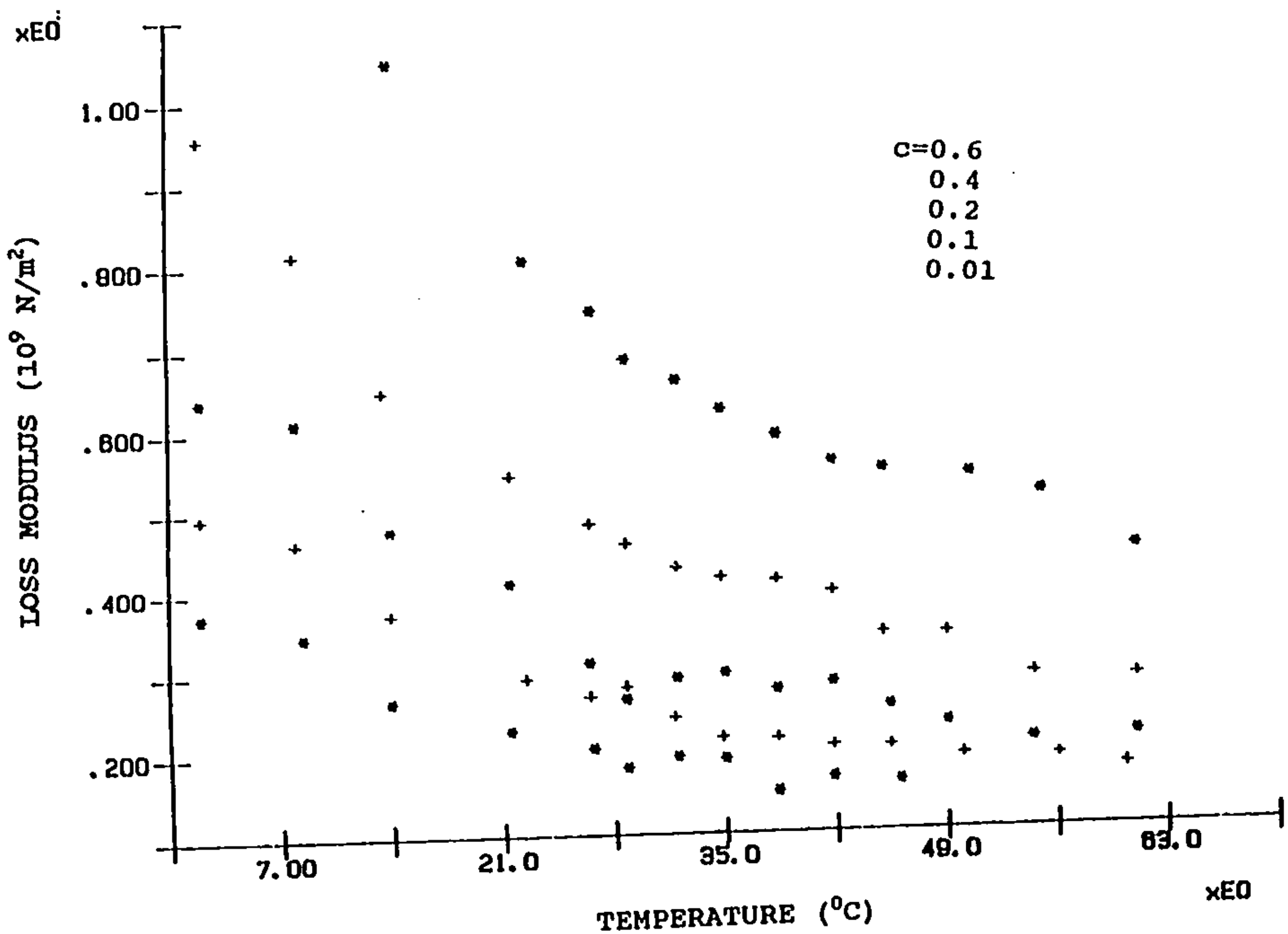

Fig. 3.15 Temperature dependence of longitudinal loss modulus.

Table 3.1 Refractive indexes

c	0.01	0.1	0.2	0.4	0.6	0.8
n	1.3324	1.3385	1.3545	1.3707	1.3867	1.4034

That different concentrated solutions have different temperature dependent behaviours of the Brillouin shift (or equivalently, the sound velocity and storage modulus) is quite interesting, and has not been presented in other reports.

3.3.3 Concentration Dependence

Fig. 3.16 displays the change in Brillouin shift with concentration for two temperatures (14°C and 26°C). It is quite clear that a linear relation exists within experimental error. The linear approximation breaks down at concentration of about 0.4. The same behaviour can be found at other temperatures. In the inset are the best fitting lines for the temperatures of 14°C, 22°c, 26.5°C 32°C and 35°C. It can be seen that the lower the temperature the larger the slope of the fitting line, and all of these lines having different slopes intersect in the region around c=0.25. But at even higher temperatures, the best fitting lines will not intersect at that region. As to the Brillouin width, it increases with concentration (Fig. 3.17), however, the curves for various

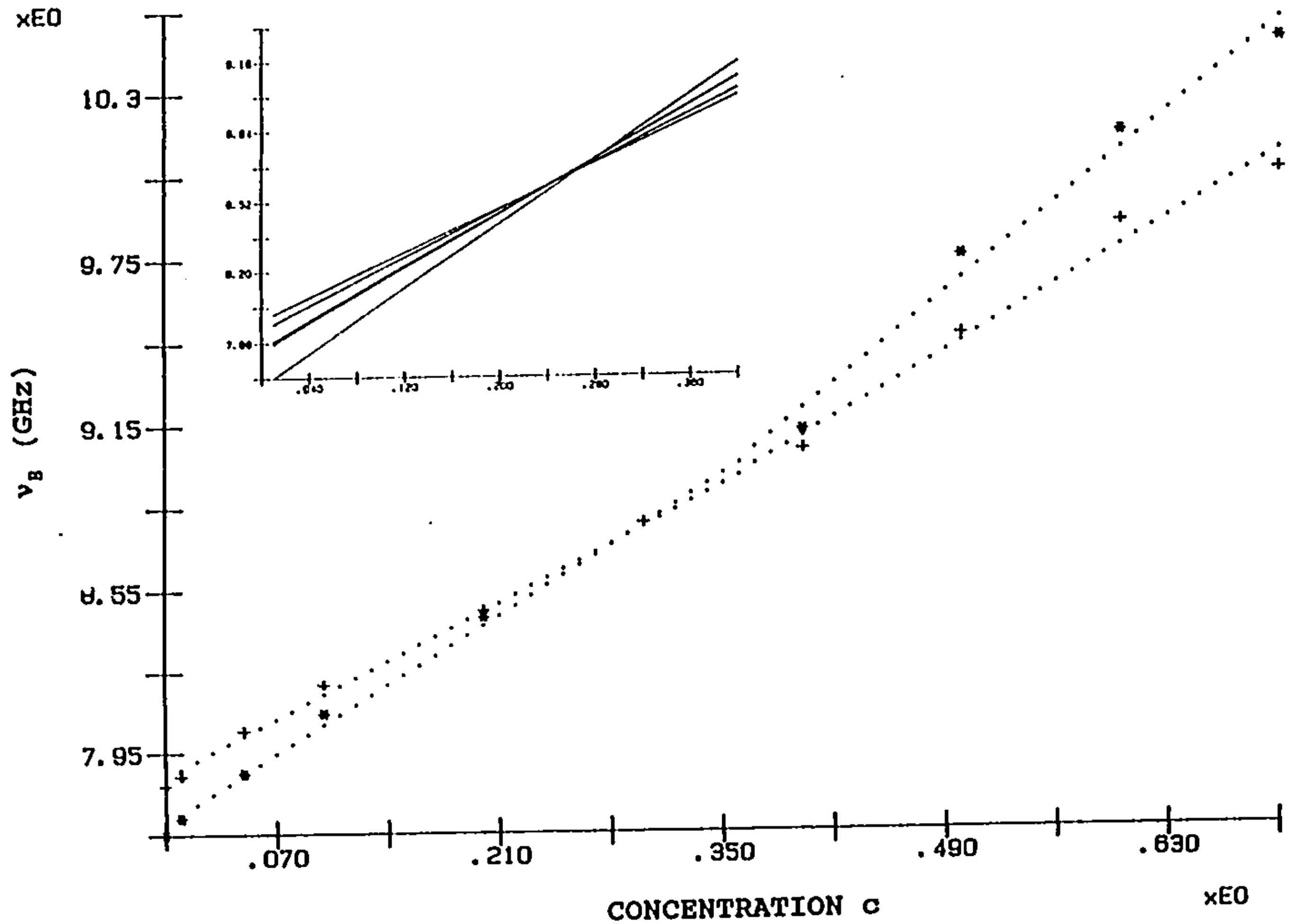

Fig. 3.16 Concentration dependence of the Brillouin shift at 14°C (*) and 26°C (+). The dotted lines are the best fitting curves. In the inset are the best fitting lines for 14°C, 22°C, 26.5°C, 32°C and 35°C.

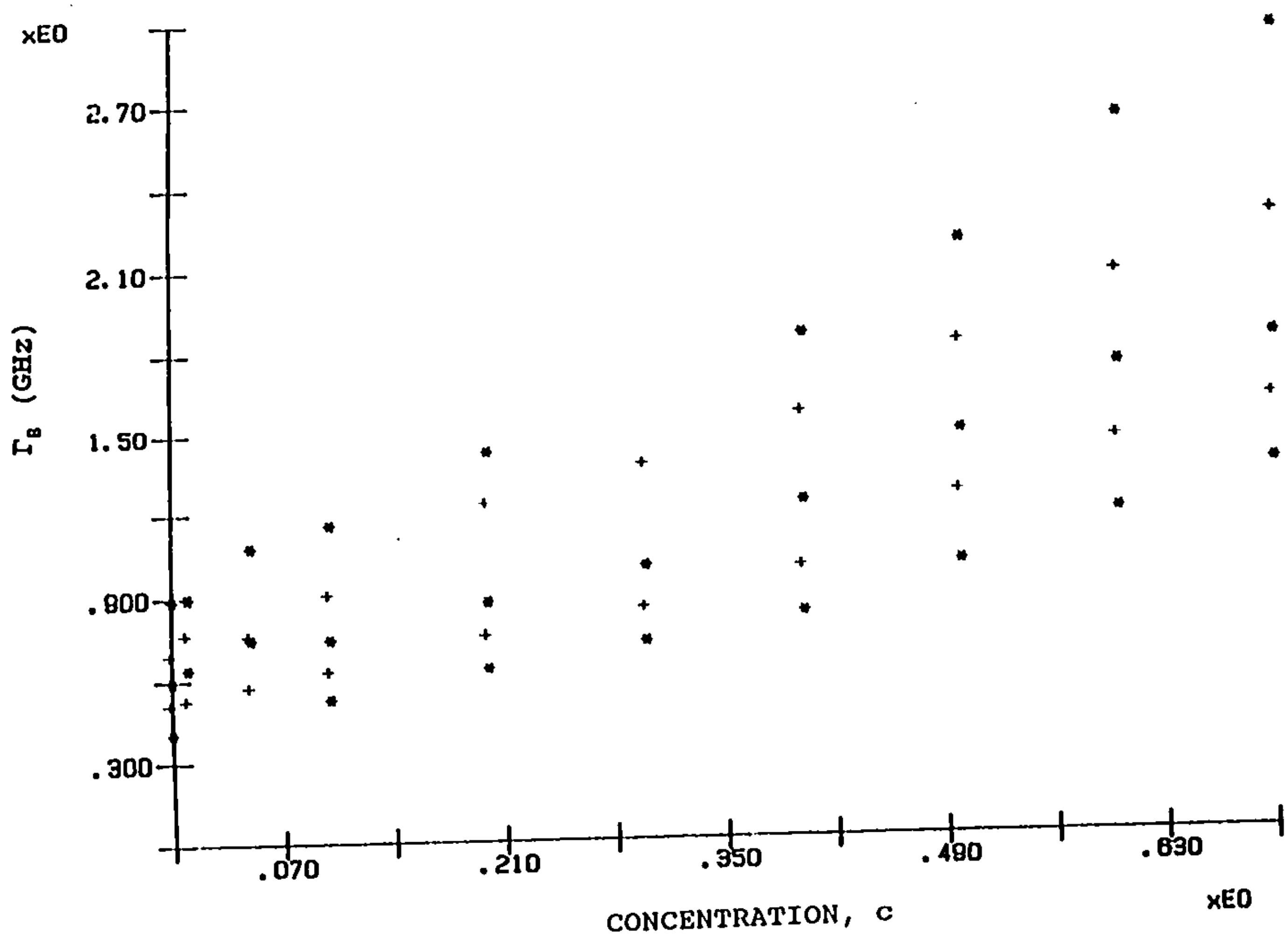

Fig. 3.17 Concentration dependence of the width, T=14, 22, 32, 45, 61^{0}C (from top to bottom).

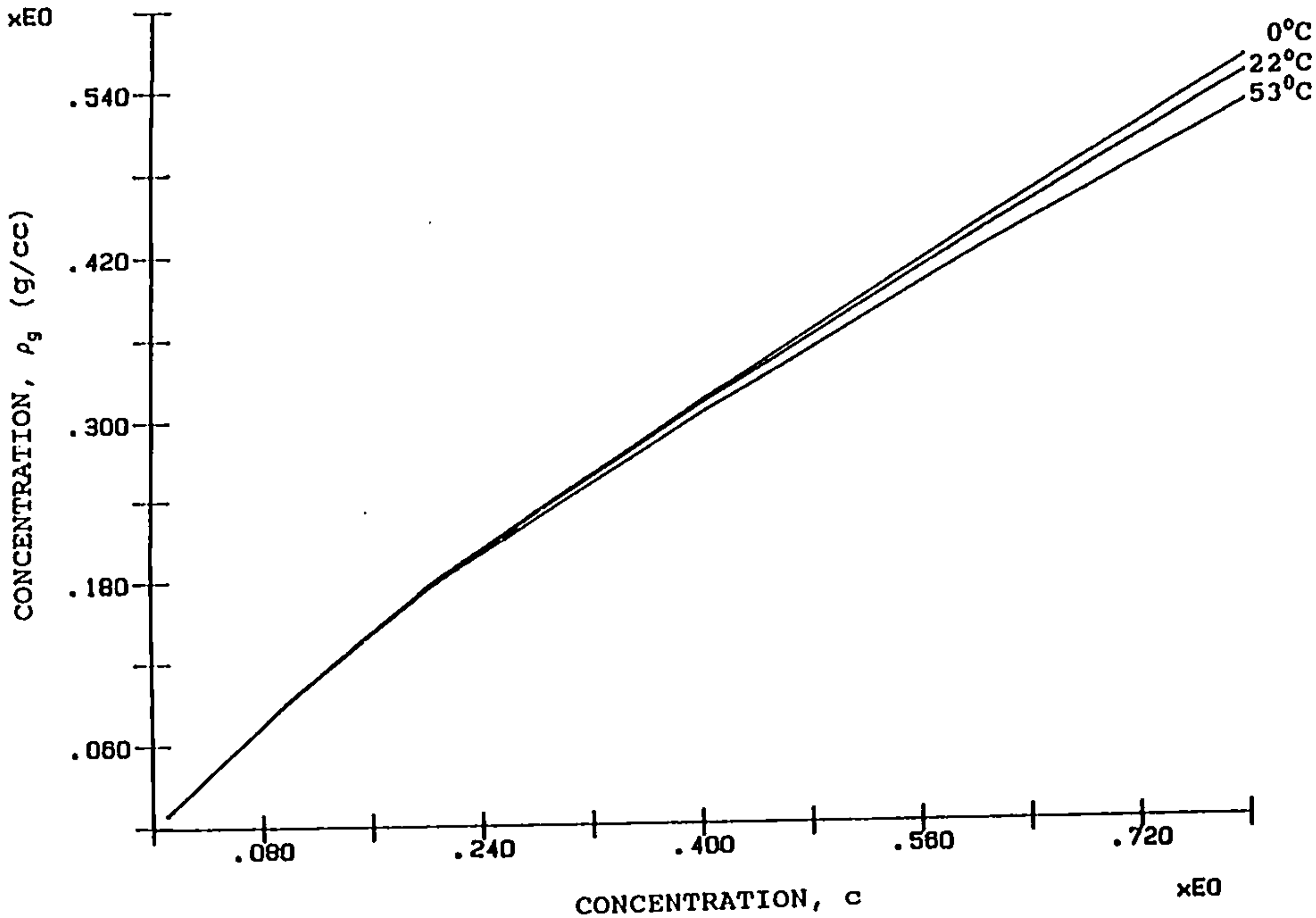

Fig. 3.18 The relation between two units of concentration: ρ_g vs c.

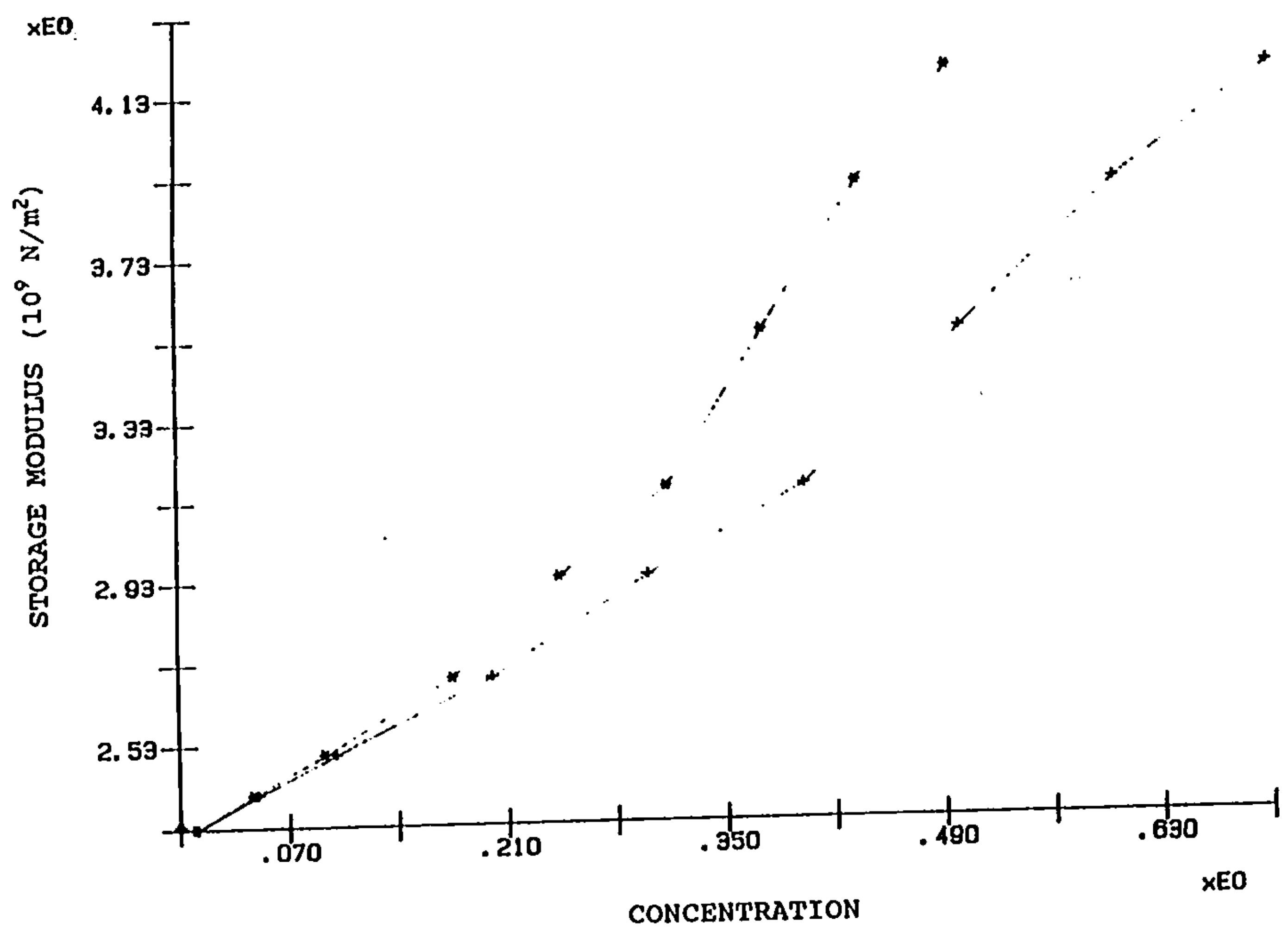

Fig. 3.19 Storage modulus as a function of concentration at 22^{o}C, where different units were used for concentration: c (+) and ρ_g (*).

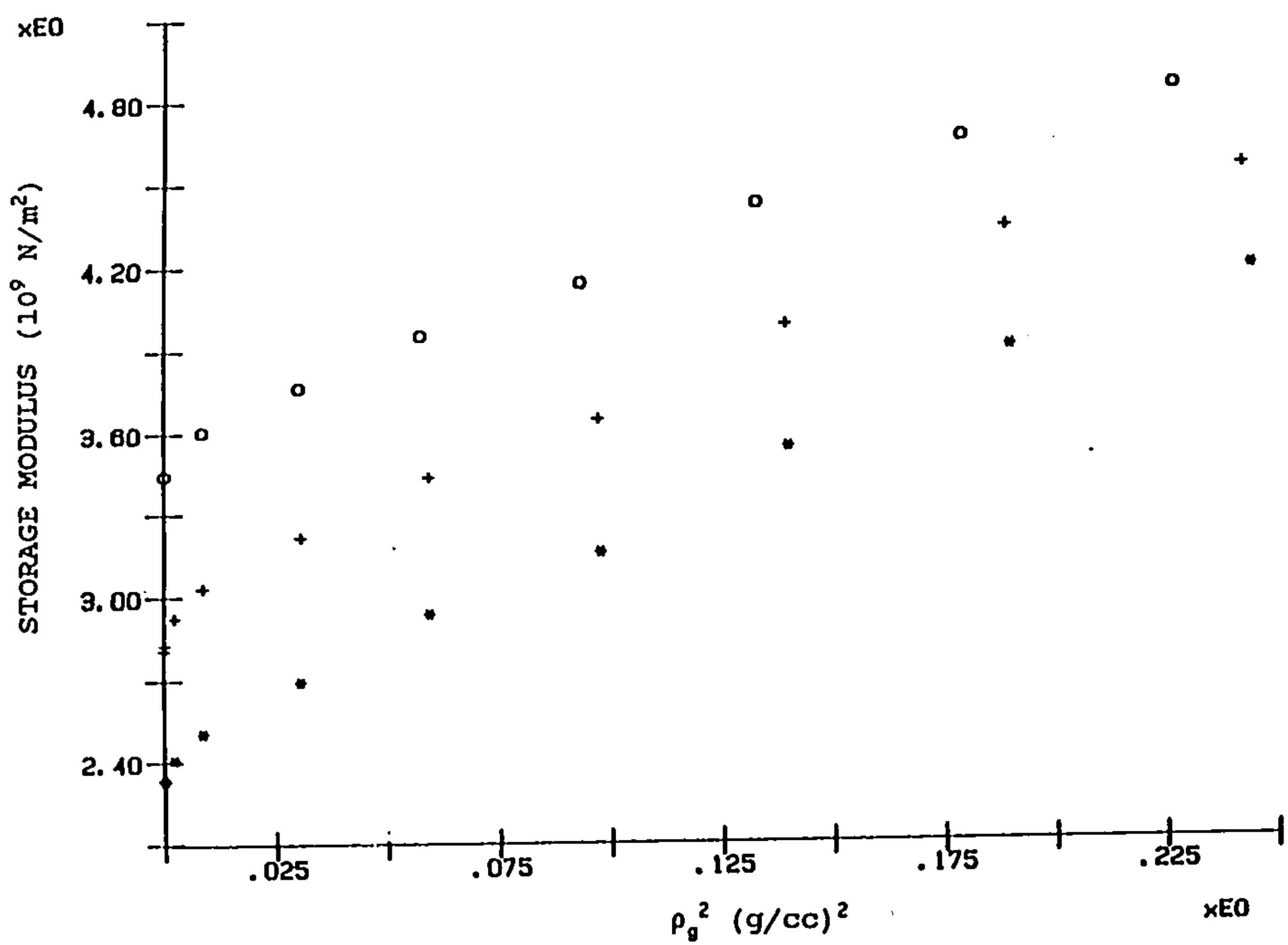

FIG. 3.20 Storage modulus, plotted against square of concentration (ρ_g^2) at different temperatures: 55°C (o), 26°C (+) and 22°C (*), where the higher plots have been offset by 0.5 and 1.0 for clarity.

temperatures do not intersect each other but diverge.

It should be mentioned that the concentration dependence shown in figures 3.16 and 3.17 are the data from temperature dependence experiments. The data from time dependence (warming process) are different, presumably due to a different influence of thermal history on the experimental results.

Also it should be noted that the concentration unit used till now was the weight ratio of gelatin to water. If the concentration is expressed as %w/w or gelatin density ρ_g (g/cc) (Fig. 3.18), the shape of those curves in Fig. 3.16 will be different.

Fig. 3.19 displays the concentration dependence of storage modulus at 22°C, where two different units c and ρ_g were used to express concentration. According to J. Ferry' data (1948), the shear modulus is proportional to the square of concentration (g./100cc). I plotted the longitudinal storage modulus against the square of concentration (ρ_g^2) (Fig. 3.20) as a comparison.

3.4 Discussion

In order to get more information about the gelatin-water system, I will use three different models to analyze the experimental data. It should be mentioned since this biopolymer system is quite complicated there is no perfect theory for it. Every model has its merit, also its problem.

Also, I would like to mention the work of two other groups. One is E. Courtens' work on Brillouin-scattering measurements of phonon-fracton crossover in silica aerogels (1987). Another is C. M. Sorensen's work on anomalous diffusion in aqueous solutions of gelatin (Ren et al. 1992, 1993).

Courtens' results are reprinted and shown in Fig. 3.21. Although I did not do the wave-vector (angular) dependent experiment, I am sure I will not get the same dispersion curve at low density as his even if I did it, which can be expected if we compare his ν_B-ρ, Γ_B-ρ behaviour with mine.

Table 3.2 A comparison between Courtens' results and mine

His results $\theta = 180°$	ρ_g Kg/m^3	103	186	407
	ν_B GHz		0.7	3.55
	Γ_B GHz		~0.55	~0.35
	ν_B/Γ_B		1.27	10.14
My results $\theta = 173°$	ρ_g Kg/m^3	93	175	435
	ν_B GHz	8.16	.45	9.96
	Γ_B GHz	0.90	1.23	2.05
	ν_B/Γ_B	9.10	6.90	4.85

The column for ρ_g = 103 kg/m^3 is empty because at that density ν_B is too small and Γ_B is too large to be figured out from the curve in Fig. 3.21a.

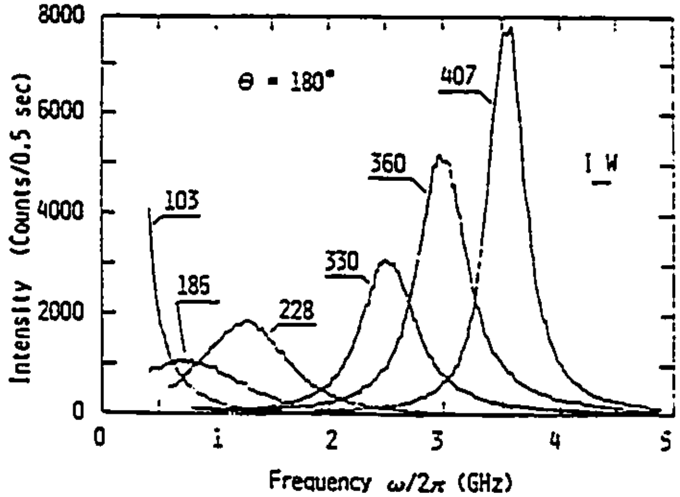

(a)

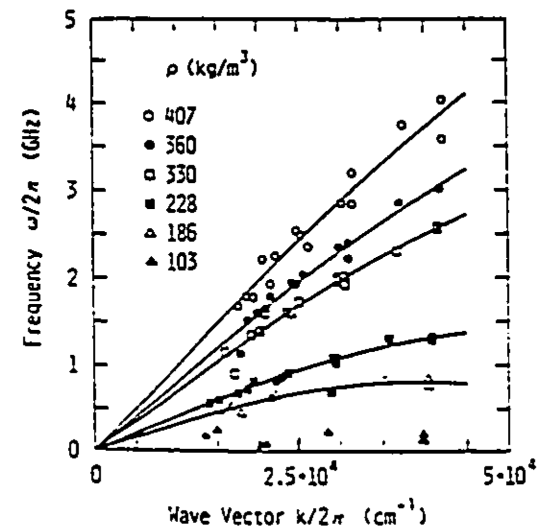

(b)

Fig. 3.21 Courtens' results. (a) Backscattering spectra for six densities (in Kg/m^3) of silica aerogel samples. IW is the full instrumental width at half-height. The central portion of the spectra, affected by the elastic line, was removed for clarity. (b) Measured dispersion curves.

His spectra demonstrate a remarkable decrease of Brillouin shift and increase of Brillouin width on decreasing density at constant wave-vector. But my results show both of ν_B and Γ_B decrease on decreasing density (Fig. 3.16 and Fig. 3.17). His ν_B/Γ_B decreases with decreasing density, but mine increases (Table 3.2). That is why Courtens' group can find a density just under 186 Kg/m^3 at which $\nu_B = \Gamma_B$ (crossover frequency), but I cannot no matter how low the density is.

That $\nu_B = \Gamma_B$ corresponds to the phonon mean free path equal to phonon wavelength since $\Gamma = \tau^{-1} = v/l = \nu\lambda/l$, implying that the phonons are localized. I can never get that point of $\nu_B = \Gamma_B$ or $l = \lambda$ means one will not find a localized phonon (group velocity = 0) at low density in this gelatin-water system.

Sorenson's group used a dynamic light scattering technique, performed in the homodyne mode, to study the relaxation process of semidilute gelation solution. Their results indicate three modes of relaxation: a fast exponential mode at short time ($t < \sim 50$ μs), followed by a power law at intermediate time ($t < \tau_c$), and a stretched exponential mode at long time, where $\tau_c \rightarrow \infty$ as the quenched system evolves to a gel. They interpret the fast mode as the incipient gel mode due to short-range monomer or blob motion of the chains, and the second and third modes as anomalous diffusion modes where the mean-square displacement is proportional to ln(t) at intermediate time and t^{β} with $\beta < 1$ at long time.

It is hard for me to make any comment on their results and conclusions since I did different experiments and studied different phenomenon.

Firstly, Brillouin scattering method is usually used to study relatively rapid dynamic processes occurring on a time scale faster than about 10^{-6} second. The optical mixing homodyne method are used for processes that occur on a time scale slower than about 10^{-6} second. That is why it is impossible for me to study the diffusion process on a time scale as large as 50 μsec.

Secondly, the main field I studied is the mechanical properties (sound propagation and attenuation) of gelatin gel, their change with time, temperature and concentration. Sorenson's attention was focused on the diffusion in gelatin solution ($T > T_g$) or the diffusion in solution set to gel ($T < T_g$, but before gelation).

Thirdly, there is a fundamental difference between the diffusion process in a solution of polymer, and in gels. The difference results from the cross-linking between polymers in gels (Tanaka, 1985; Munch, et al. 1976). So, even if I study the diffusion process, we are still not studying the same physical system.

3.4.1 Model 1

A simple model can be constructed by assuming that the storage modulus of the gel system is the sum of the contributions from the network and from the fluid. Phonons will be scattered by solvent molecules and gelatin molecules, and the scattering cross-section of a gelatin molecule in the network is different from that of the residual molecule in the fluid (Walton, 1994).

Consider a unit volume of gelatin-water system. Let N be the total number of gelatin molecules which occupy a fraction ϕ of the volume, and $\alpha(T)$ the number fraction in the network at gel state, then αN will be the number of gelatin molecules in the network which occupy a fraction $\alpha(T)\phi$ of the volume. The fluid, consisting of water and gelatin residual molecules, occupies a volume of $1-\alpha(T)\phi$, and the gelatin residues occupy a volume of $[1-\alpha(T)]\phi$. Thus, the gelatin residues volume fraction ϕ_r in the fluid is given by

$$\phi_r = \frac{[1-\alpha(T)]\phi}{1-\alpha(T)\phi} \qquad (51)$$

Since fluid is a suspension, its bulk modulus can be calculated using the following formula (Wood, 1964)

$$1/K_f = (1-\phi_r)/K_w + \phi_r/K_m \qquad (52)$$

where K_w and K_m are the bulk moduli of water and gelatin molecules, respectively. Note that from now on all the modulus means storage modulus.

$$K_f = \frac{[1-\alpha(T)\phi]K_v}{1-\phi(1-r)-r\alpha(T)\phi} \tag{53}$$

where $r = K_v/K_m$.

Let the contribution of the network to the longitudinal modulus be $M'_n(\alpha(T)\phi)$, some function of the number of molecules in the network, then the total longitudinal modulus can be written as

$$M' = K_f + M'_n(\alpha(T)\phi) \tag{54}$$

Fluctuations in density will scatter phonons. Let the scattering cross-section of a gelatin molecule in the network be σ and that of the residual molecule in the fluid σ_0, the phonon mean free path l is given by

$$l^{-1}=l_i^{-1}(T)+[N-\alpha(T)N]\sigma_0+\alpha(T)N\sigma \tag{55}$$

where $l_i^{-1}(T)$ is the inverse of the phonon mean free path in the solvent. The inverse of the phonon lifetime is

$$\tau^{-1}=\Gamma=\frac{v}{l}=v\lambda l^{-1} \tag{56}$$

and

$$tg\theta=\frac{\Gamma}{v}=(tg\theta)_i+\frac{2\pi}{q}[\sigma_0 N+(\sigma-\sigma_0)\alpha N] \tag{57}$$

where $(tg\theta)_i$ is the loss tangent of the water.

Let m_m and V_m be the gelatin molecular weight and volume, then

$$N = \frac{\rho_g}{m_m} = \frac{\phi}{V_m} \tag{58}$$

Thus,

$$\begin{aligned} tg\theta &= (tg\theta)_i + \frac{2\pi}{q}\frac{\rho_g}{m_m}[\sigma_0+(\sigma-\sigma_0)\alpha(T)] \\ &= (tg\theta)_i + 1.933\times10^{14}\frac{\rho_g}{n(\rho_g)}[\sigma_0+(\sigma-\sigma_0)\alpha] \end{aligned} \tag{59}$$

or

$$tg\theta = (tg\theta)_i + \frac{2\pi}{q}\frac{\phi}{V_m}[\sigma_0+(\sigma-\sigma_0)\alpha(T)] \tag{60}$$

σ_o and Empirical Formula for Loss Tangent

σ_0 can be determined from the experimental results of 61^0C (Fig. 3.22). The best fitting curve gives

$$tg\theta=0.1315\rho_g+0.0503 \qquad (\rho_g<0.3g/cc) \tag{61}$$

Since at this temperature α should be equal to zero, by comparing Eq. (59) with Eq. (61) we have

$$\frac{1.933\cdot10^{14}}{n}\sigma_0=0.1315 \tag{62}$$

and

$$\sigma_0=0.068\cdot10^{-14}n=0.058\cdot10^{-14}(1.3308+0.1331\rho_g) \tag{63}$$

$$(\sigma_0)_{ave}=9.2\cdot10^{-16}cm^2 \tag{64}$$

Now, equation (59) can be rewritten as

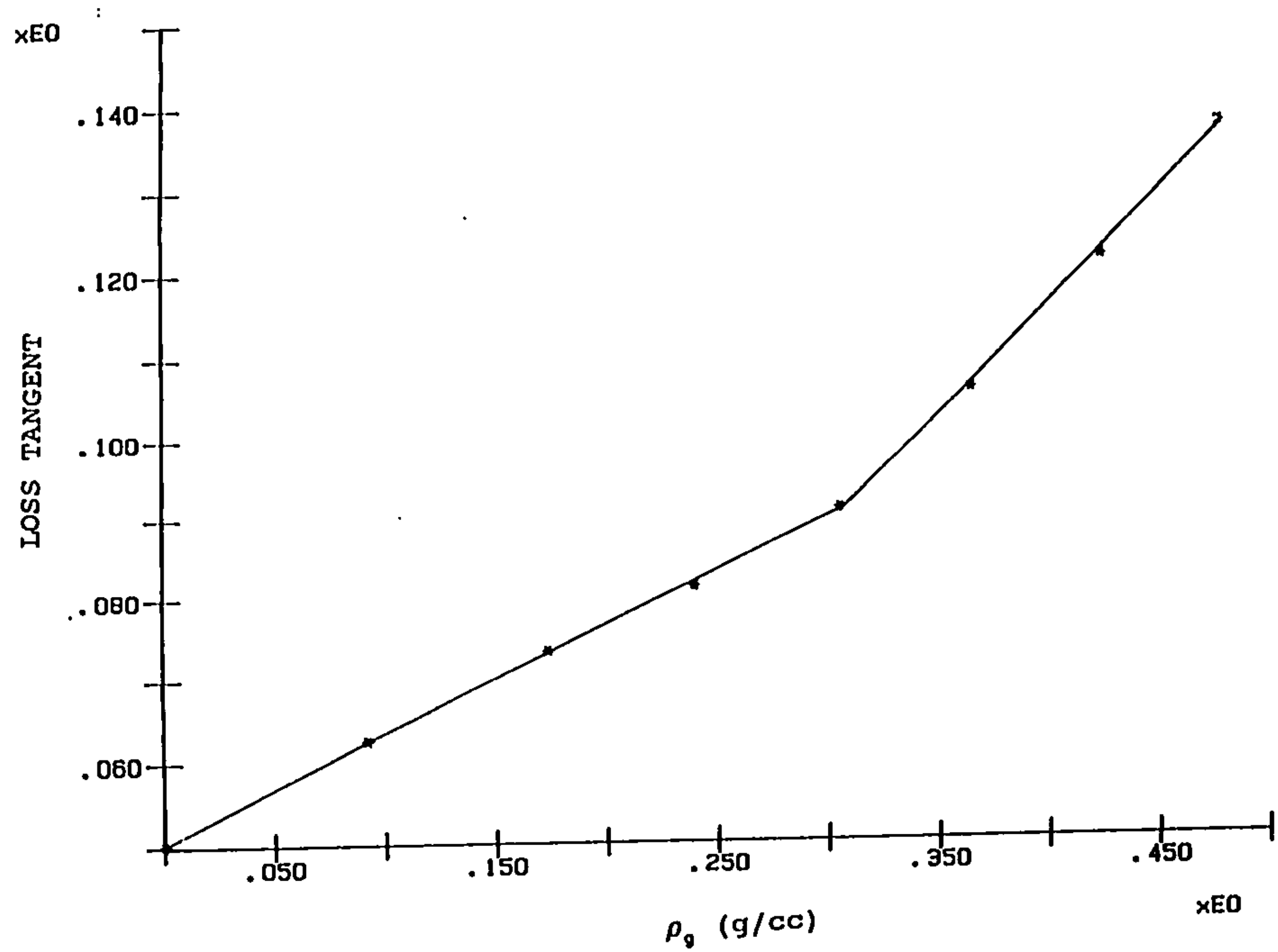

Fig. 3.22 Loss tangent vs ρ_g at 61°C. The solid line is the best fitting curve.

$$(tg\theta)(\rho_g,T)=(tg\theta)_i(0,T)+0.1315\rho_g + 1.933\cdot10^{14}\frac{\rho_g}{n(\rho_g)}(\sigma-\sigma_0)\alpha(T) \tag{65}$$

or

$$\left[\frac{(tg\theta)-(tg\theta)_i}{\rho_g}-0.1315\right]n(\rho_g) = 1.933\cdot10^{14}(\sigma-\sigma_0)\alpha(T) \equiv y(T,\rho_g) \tag{66}$$

where y, according to the assumption, should be a function of T only. However, after comparing with experimental data, I found that y depends on concentration too. That is to say either $(\sigma-\sigma_0)$ or α has to be concentration dependent. For the time being, let us treat Y as a function of T as well as ρ_g, and compare with the experimental data to find an empirical formula for $y(T,\rho_g)$.

Since at temperatures higher than melting temperature T_m, α should be equal to zero, we can assume that

$$y(T,\rho_g)=\begin{cases} k(\rho_g)(T_m-T) & (T\le T_m) \\ 0 & (T>T_m) \end{cases} \tag{67}$$

where $k(\rho_g)$ is an unknown function. Compared with the experimental data it can be found that

$$T_m = -102.46\rho_g^2 + 62.62\rho_g + 23.87 \tag{68}$$

and

$$k(\rho_g) = (-550\rho_g^2 + 362\rho_g + 10.26)^{-1} \tag{69}$$

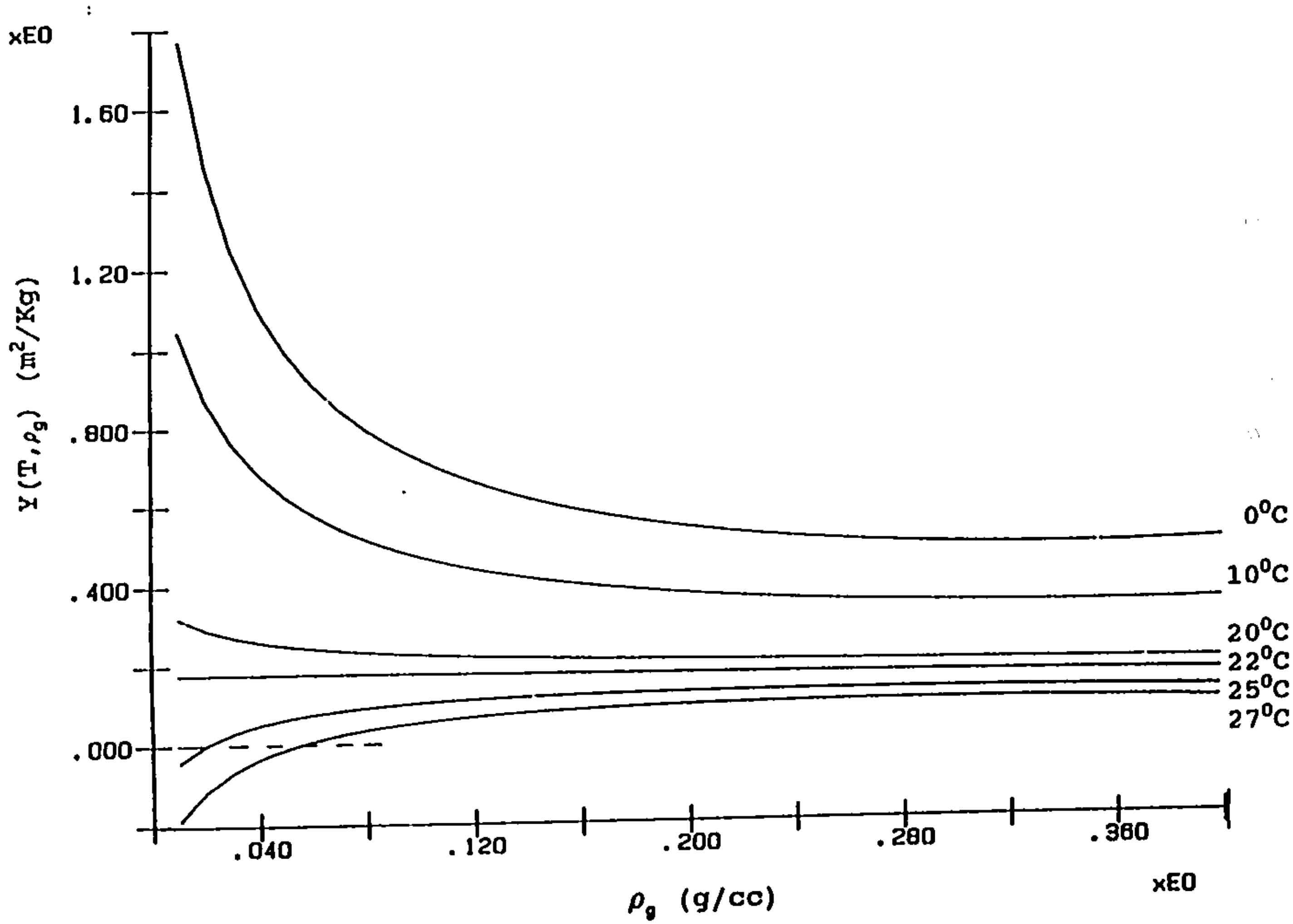

Fig. 3.23 The behaviour of $y(T,\rho_g)$: y against ρ_g.

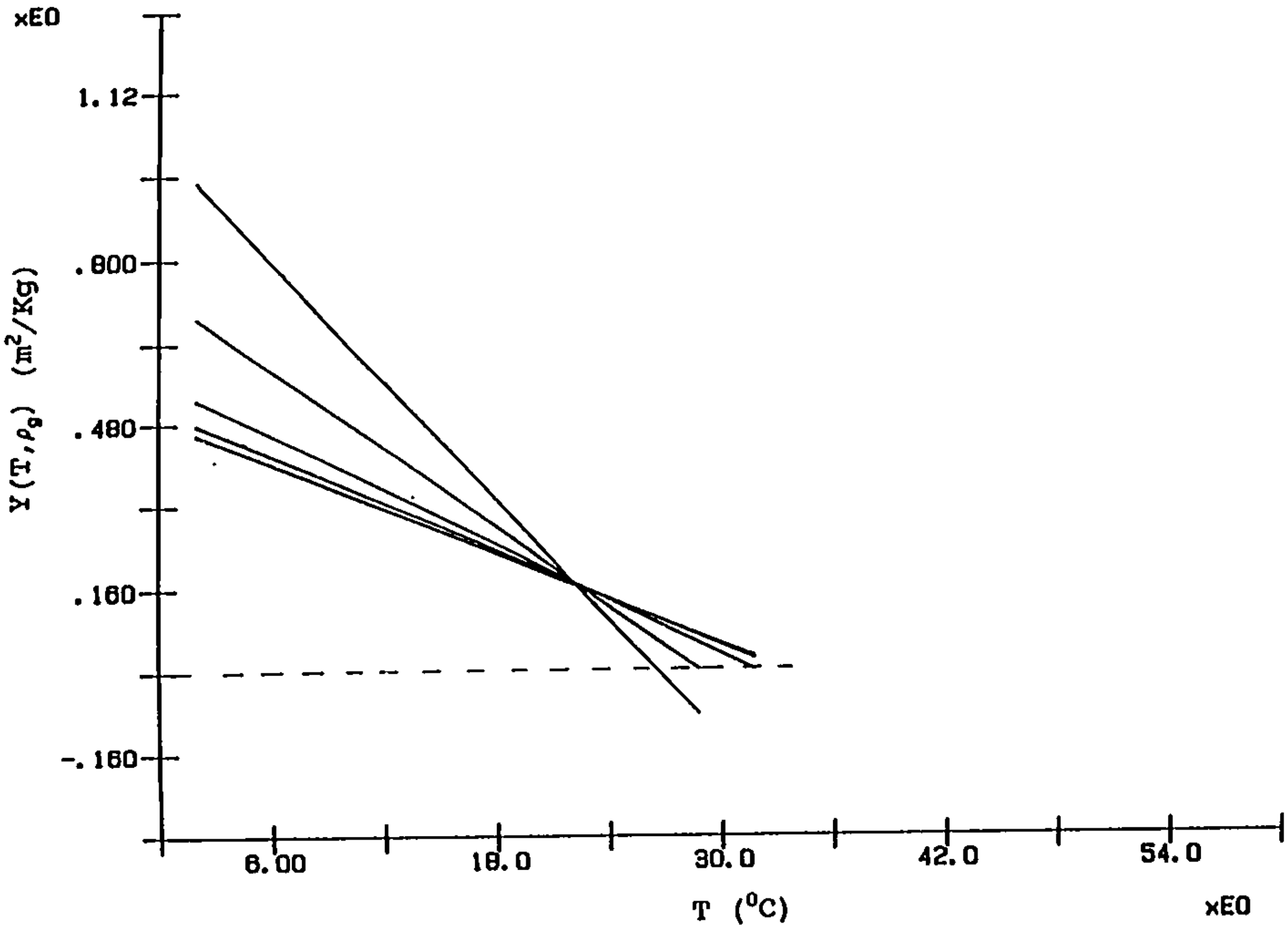

Fig. 3.24 The behaviour of $y(T,\rho_g)$: y vs. T , ρ_g = 0.05 (the line with the greatest slope), 0.1, 0.2, 0.3 and 0.4 (the line with the smallest slope) g/cc.

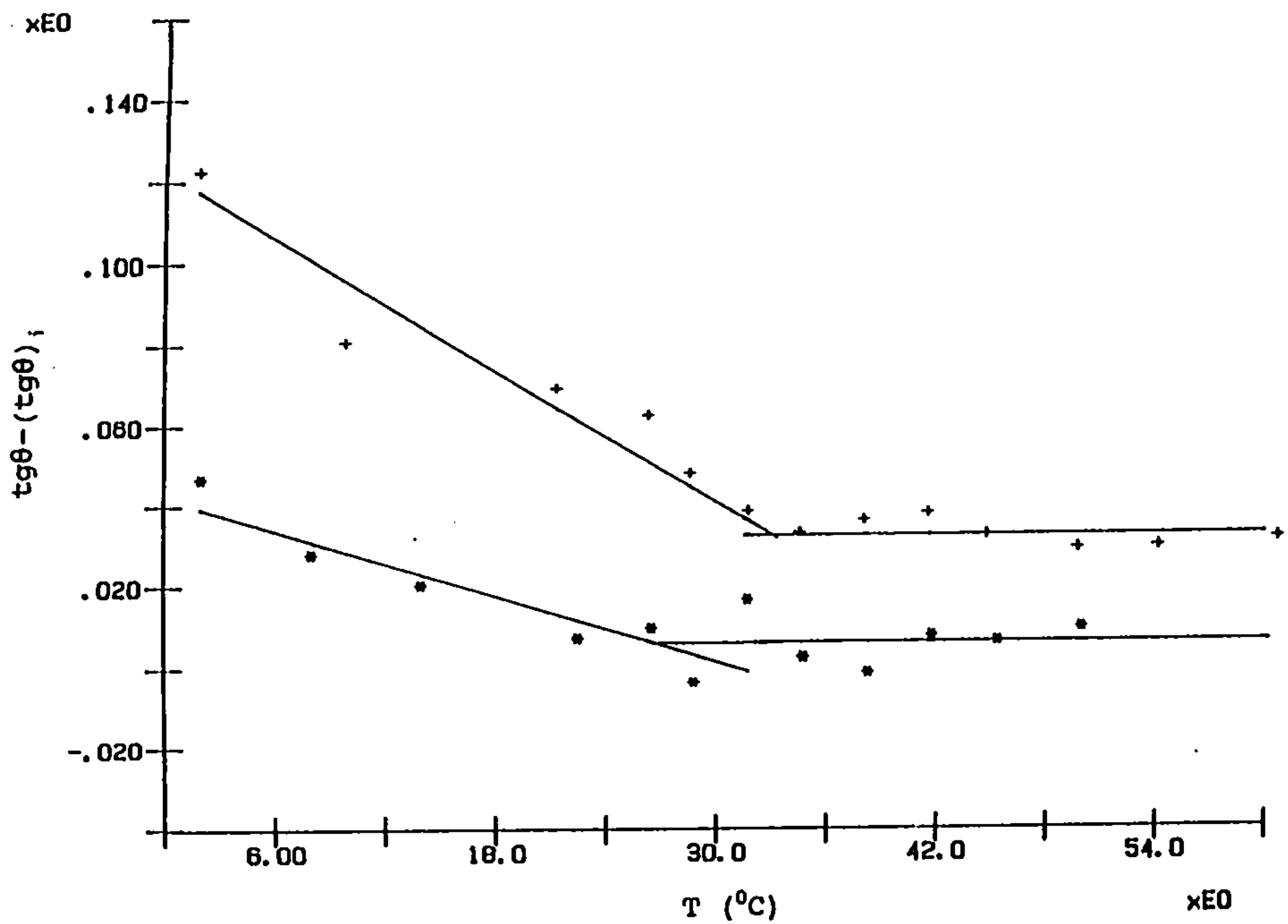

Fig. 3.25 $tg\theta-(tg\theta)_i$ as a function of temperature: c=0.05 (or $\rho_g \approx 0.047$g/cc) (*), c=0.3 (or $\rho_g \approx 0.244$g/cc) (+) and solid lines are the theoretical curves.

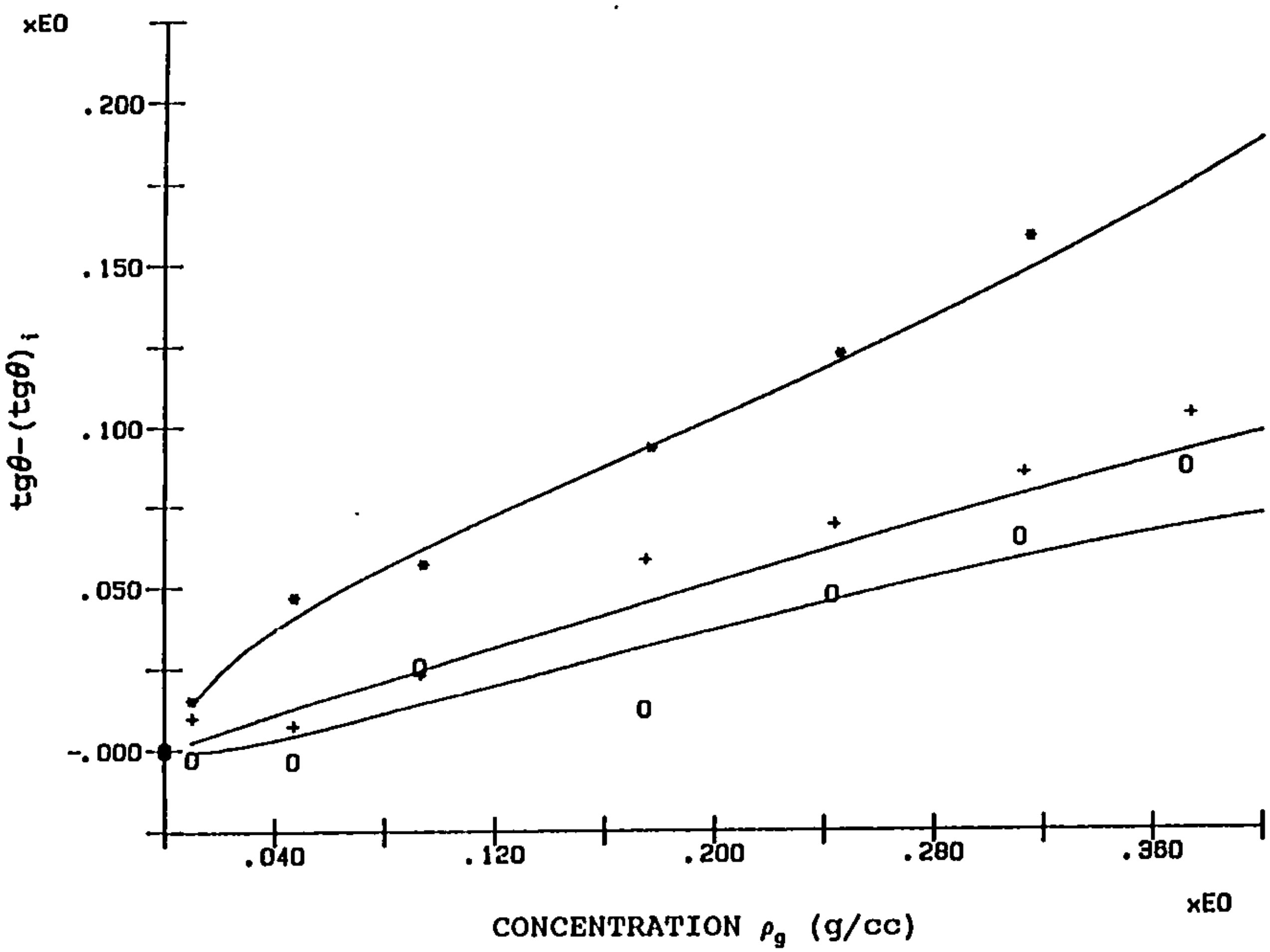

Fig. 3.26 $tg\theta-(tg\theta)_i$ as a function of concentration: T=1°C (*), 22°C (+) and 28°C (o). The solid lines are the theoretical curves.

The curves of $K(\rho_g)(T_m-T)$ are shown in Figs. 3.23 and 3.24. The intercepts of those curves with the line y=0 denote the melting point-concentration dependence. Why all the lines in Fig. 3.24 intercept at the same point (T=22°C) and why $Y(\rho_g,T)$ decreases with increasing ρ_g at $T<22^0C$ are left as two open questions.

The empirical formula for loss tangent can be obtained from Eqs. (66), (68) and (69), which is given by

$$tg\theta - (tg\theta)_i = 0.1315\rho_g + Y(T,\rho_g)\rho_g/n(\rho_g) \qquad (T\leq T_m) \quad \textbf{(70)}$$

In figures 3.25 and 3.26 are the theoretical curves, which fit the experimental data quite well.

Modulus of Network

In order to calculate $M'_n(\alpha(T)\phi)$, $\alpha(T)$ has to be found first. By changing the concentration unit from ρ_g to ϕ, we can plot $\alpha(T)/a$ against ϕ for different temperatures (Fig. 3.27), where

$$a = \frac{V_m}{\lambda(\sigma-\sigma_0)} \qquad \textbf{(71)}$$

$\alpha(T)/a$ is dependent on ϕ as I pointed out before. However, in the intermediate concentration region, the curves are quite flat. I calculated the average values of $\alpha(T)/a$ in this region and found its temperature dependence which is given by

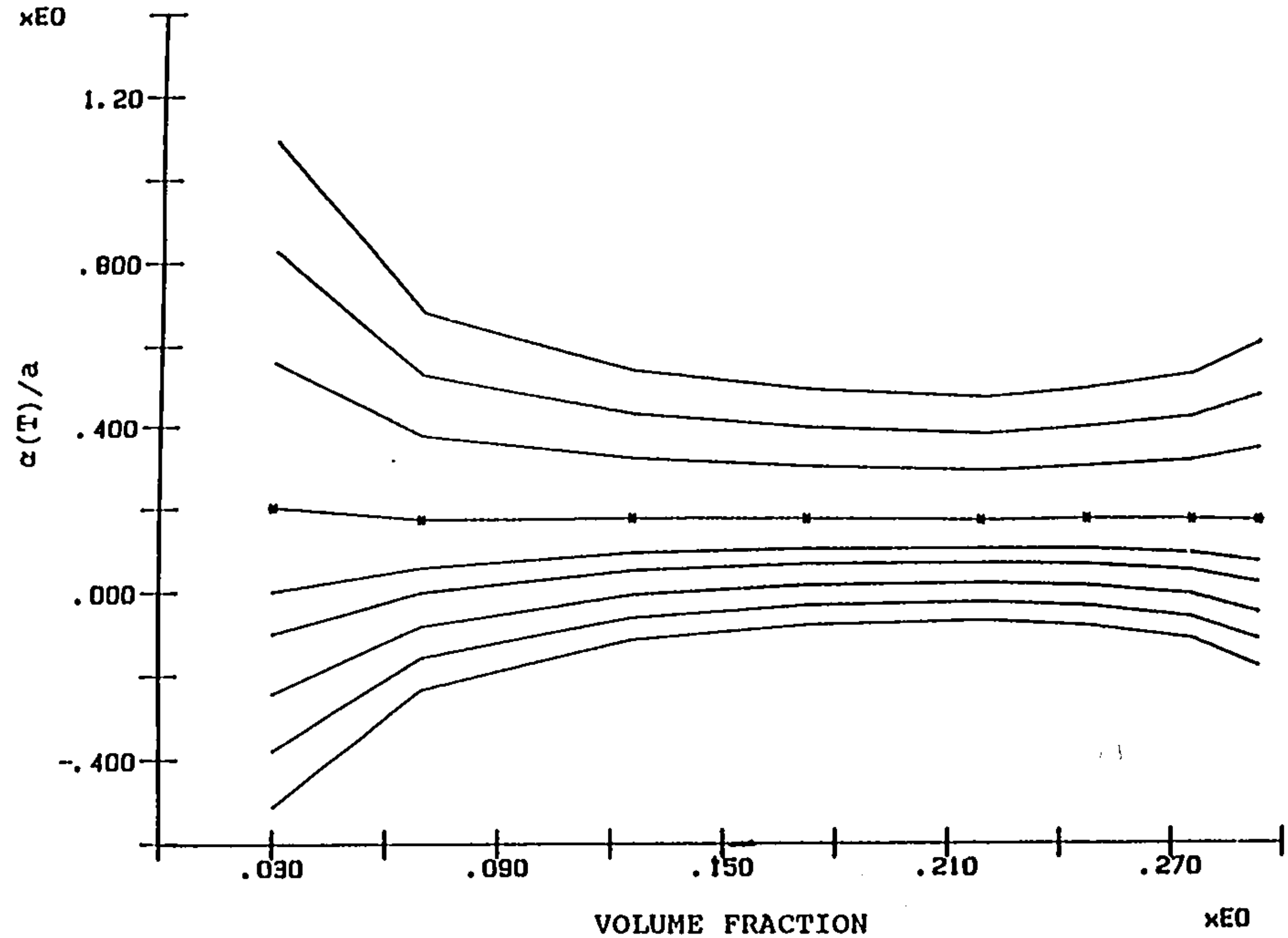

Fig. 3.27 $\alpha(T)/a$ at T = 1, 8, 14, 22, 26.5, 28.8, 32, 35, 38°C (from top to bottom), where $a=V_m/\lambda(\phi-\sigma_o)$.

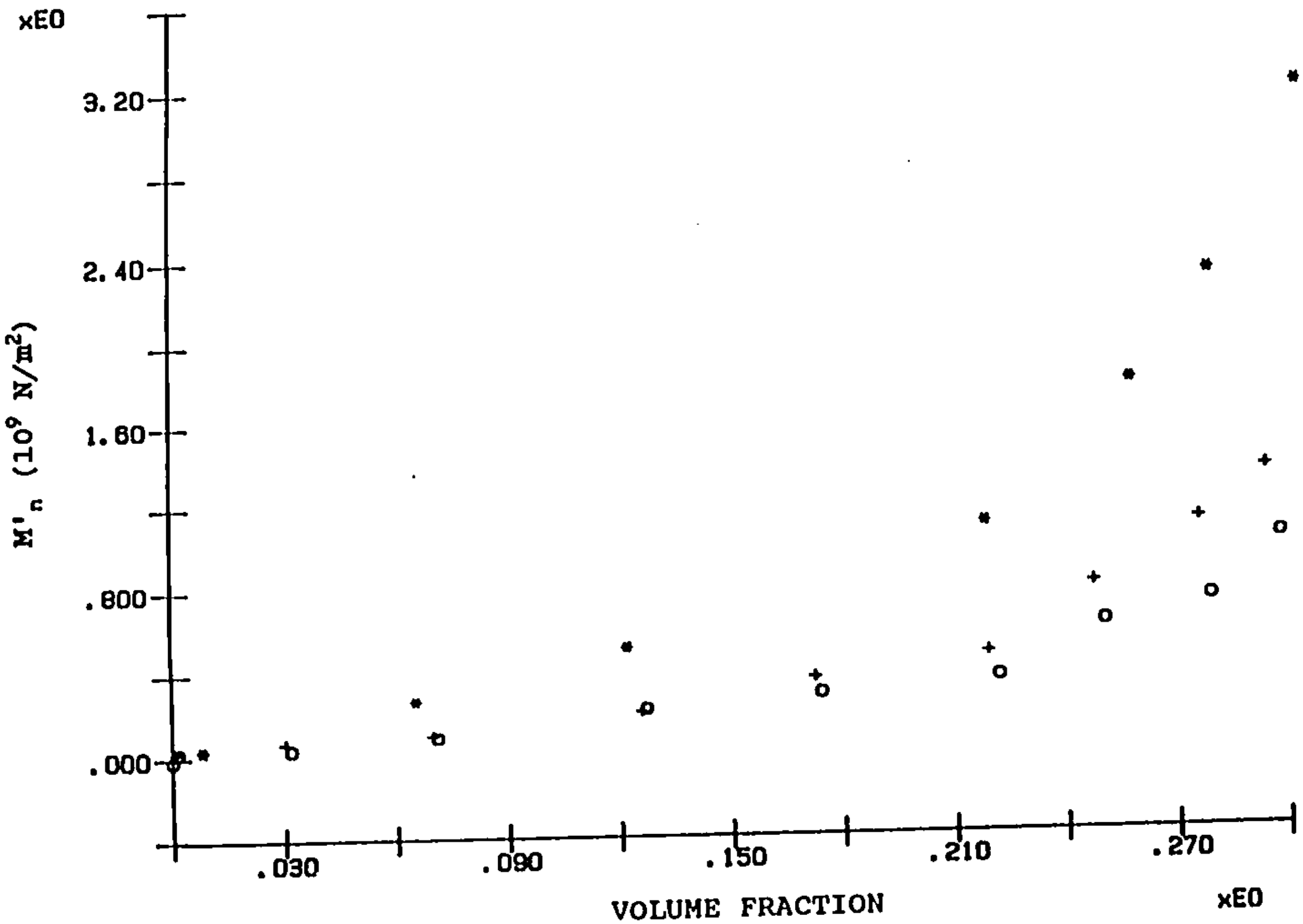

Fig. 3.28 Longitudinal storage modulus of network, calculated by model 1, at 1°C (*), 22°C (+) and 28°C (o).

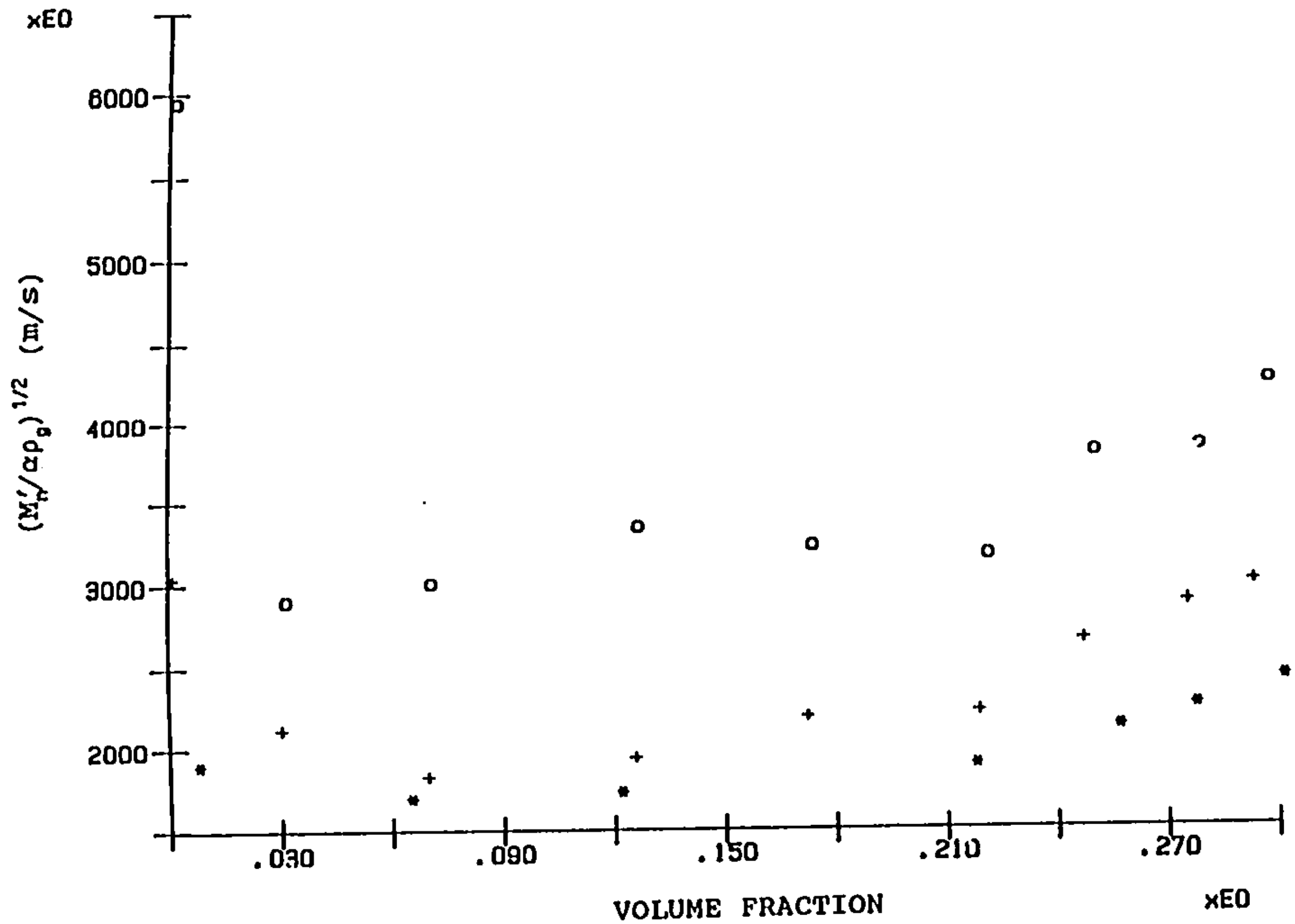

Fig. 3.29 $(M_n'/\alpha\rho_g)^{1/2}$ at 1°C (*), 22°C (+) and 28°C (o) (model 1).

$$\left(\frac{1}{a}\alpha\right)_{ave}(T) = 0.5696 - 0.0180T \tag{72}$$

Since at 0°C α should be close to 1, let a equal to 1.7556 so that

$$\alpha_{ave}(T) = 1 - 0.0316T \tag{73}$$

Using this $\alpha_{ave}(T)$ for the $\alpha(T)$ in Eq. (54), M'_n can be deduced from the experimental data of M' vs. ϕ. The curves of M'_n vs ϕ for 28°, 22°C and 1°C are shown in Fig. 3.28. M'_n increases with ϕ but decreases with T, which I think the behaviour of M'_n should be.

One problem of this model is that if M'_n and the network density $\alpha\rho_g$ are used to calculate $(M'_n/\alpha\rho_g)^{1/2}$, which corresponds to the sound velocity in the network, it will be found the higher the temperature the larger the $(M'_n/\alpha\rho_g)^{1/2}$ (Fig. 3.29), which is hard to understand. One possibility causing the problem is the substitution of $\alpha(T)$ by $\alpha_{ave}(T)$. According to Eq. (73), T cannot be larger than 31.6°C, otherwise α_{ave} will be negative, that is to say, no gel state can exist at T>31.6°C, which is contradictory to the melting point result. Later, in the summary, we will see there is another reason which may cause this problem.

σ

Using ϕ as the concentration unit, the best fitting curve to the experimental data of tgθ at 61°C is given by

$$[tg\theta]_{T=61^{\circ}C} = 0.1820\phi + 0.0508 \qquad (\phi < 0.218) \tag{74}$$

Since

$$[tg\theta-(tg\theta)_{1}]_{T=61^{\circ}C} = \lambda\frac{\phi}{V_m}\sigma_0 = \frac{1}{a}\frac{\sigma_0}{\sigma-\sigma_0}\phi \tag{75}$$

we have

$$\frac{1}{a}\frac{\sigma_0}{\sigma-\sigma_0} = 0.1820 \tag{76}$$

which gives out $\sigma \approx 4\sigma_o$.

The value of σ_o seems to be too small and why σ is much larger than σ_o is left as another open question.

3.4.2 Model 2

Gel is characterized by two kinds of bulk coefficients: (a) the elastic constants of (or the sound velocity in) the network and (b) the friction factor connecting the velocity of the network relative to the gel liquid and the resistive force provided by the gel liquid (Tanaka et al., 1973; Hosea et al., 1986b; Tokita, 1993). A theory for Brillouin light scattering from gels, proposed by Marqusee and Deutch in 1981, can be used to determine these two parameters. The physical picture adopted in M-D theory is similar to that describing flow in porous media.

Elastic waves propagating in a gel are divided into two groups. One is the wave propagating in the polymer network and the another is that propagating in the fluid. Generally, elastic waves in the network and sound waves in the fluid couple each other, and there is friction between these two mediums. Margusee and Deutch treat a polymer gel as a coupled fluid and network system and define a parameter $0 \leq \lambda \leq 1$ to measure the coupling effect. Two limiting cases are considered by them.

The first case, which predicts a two-mode type of behaviour for the Brillouin spectrum , occurs for small frictional damping. In this case two pairs of Brillouin peaks should be observable, which, for weak coupling $\lambda \rightarrow 0$, approach the unperturbed fluid and network frequencies $\pm\omega_o$ and $\pm\omega_n$. The second case, the strong friction case, corresponds to a one-mode type of behaviour and predicts a single pair of Brillouin peaks at $\pm\omega$. Since only one pair of the Brillouin doublets can be found in my results, it seems appropriate to compare the results with the theory in the limit of strong friction.

According to M-D theory, in the strong friction case the average sound speed v ($=2\pi v_B/q$) in the gel and the damping of these modes Γ ($= \Gamma_B\pi/q^2$) are given by

$$\rho_T v^2 = (v_f\sqrt{\rho_f^0} + v_n\sqrt{\rho_n^0})^2 + 2v_f v_n(\sqrt{\lambda}-1)\sqrt{\rho_f^0\rho_n^0} \tag{77}$$

$$2\rho_T\Gamma=(\eta_v+\frac{4}{3}\eta_s)+\frac{1}{fv^2}\left[\frac{\rho_f^0\rho_n^0}{\rho_T}\right]^2\left[v_f^2-v_n^2+v_f v_n(\rho_f^0-\rho_n^0)\left(\frac{\lambda}{\rho_f^0\rho_n^0}\right)^{\frac{1}{2}}\right]^2 \tag{78}$$

with

$$\rho_T=\rho_f^0+\rho_n^0 \tag{79}$$

where:

q = the wave vector of the sound,

f = the friction coefficient expressing the frictional damping on the elastic network resulting from the fluid moving relative to the network,

v_f and v_n = the sound velocities in the fluid and in the polymer network,

ρ_f^o and ρ_n^o = the equilibrium densities of the fluid and the network in a gel,

η_v and η_s = the hypersonic bulk and shear viscosities of the fluid.

Note that the sign before the $v_f v_n$ term should be positive (Ng et al., 1993).

In the strong friction limit, f satisfies the following conditions:

$$f>(\eta_v+\frac{4}{3}\eta_s)q^2, \qquad \omega_f\rho_f^0 \tag{80}$$

and

$$f > \omega_n \rho_n^0 \qquad (81)$$

the right-hand side of which has an upper limit of ~ 5×10^{13} $Kgm^{-3}s^{-1}$.

Let V and m be the total volume and the total mass of the system, m_g, m_l, m_n and m_f the masses of gelatin powder, solvent (in my case, the water), cross-links and fluid respectively, we have

$$m_f + m_n = m = m_l + m_g \qquad (82)$$

and

$$\rho_f^0 V = m_f, \qquad \rho_n^0 V = m_n \qquad (83)$$

Suppose at a certain temperature $m_n = \alpha m_g$, where $0 \le \alpha < 1$ is the mass fraction and increases with the decreasing temperature, then the network density and the fluid density can be expressed as

$$\rho_n^0 = \alpha c \frac{m_l}{V} \equiv \alpha c \rho_l \qquad (84)$$

$$\rho_f^0 = [1 + (1-\alpha) c] \rho_l \qquad (85)$$

respectively, where ρ_l is a function of c, and when c=0, $\rho_l = \rho_w$. The subscript w denotes the pure salted water. Thus, we have

$$(1+c) v^2 = [1+(1-\alpha) c] v_f^2 + \alpha c v_n^2 + 2 v_f v_n \sqrt{\lambda} \sqrt{\alpha c [1+(1-\alpha) c]} \qquad (86)$$

and

$$2(1+c)\rho_l\Gamma = (\eta_v+\frac{4}{3}\eta_s)+\frac{1}{fv^2}\left[\frac{\alpha c(1+c-\alpha c)}{1+c}\right]^2\rho_1^2 \times\left[v_f^2-v_n^2+v_f v_n(1+c-2\alpha c)\sqrt{\frac{\lambda}{\alpha c(1+c-\alpha c)}}\right]^2 \tag{87}$$

with

$$\eta_v+\frac{4}{3}\eta_s=(\eta_v+\frac{4}{3}\eta_s)_w+\Delta\eta=2\rho_w\Gamma_w+\Delta\eta=2\rho_w\frac{\Gamma_{Bw}\pi}{q_w^2}+\Delta\eta \tag{88}$$

where $\Delta\eta$ is the contribution of the residues to the fluid viscosity.

Sound Velocity in Fluid

It should be mentioned that v_f is not the sound velocity in pure water, but it can be figured out from the experimental data.

From Fig. 3.30 it can be seen that the curves of M' versus ρ_g at 50^{0}C, 55^{0}C and 61^{0}C almost overlap each other at concentrations lower than about 0.3g/cc and M' increases linearly with ρ_g . Since at those temperatures no network should exist, the storage modulus can be expressed as

$$M'=M_f'=M_l'+A\rho_g \tag{89}$$

where M'_f and M'_l are the storage moduli of the fluid and liquid, respectively. Using the average value of M's of these three temperatures at ρ_g<.3g/cc, A can be determined as 2321080 m^2/s^2. In general, we can assume that

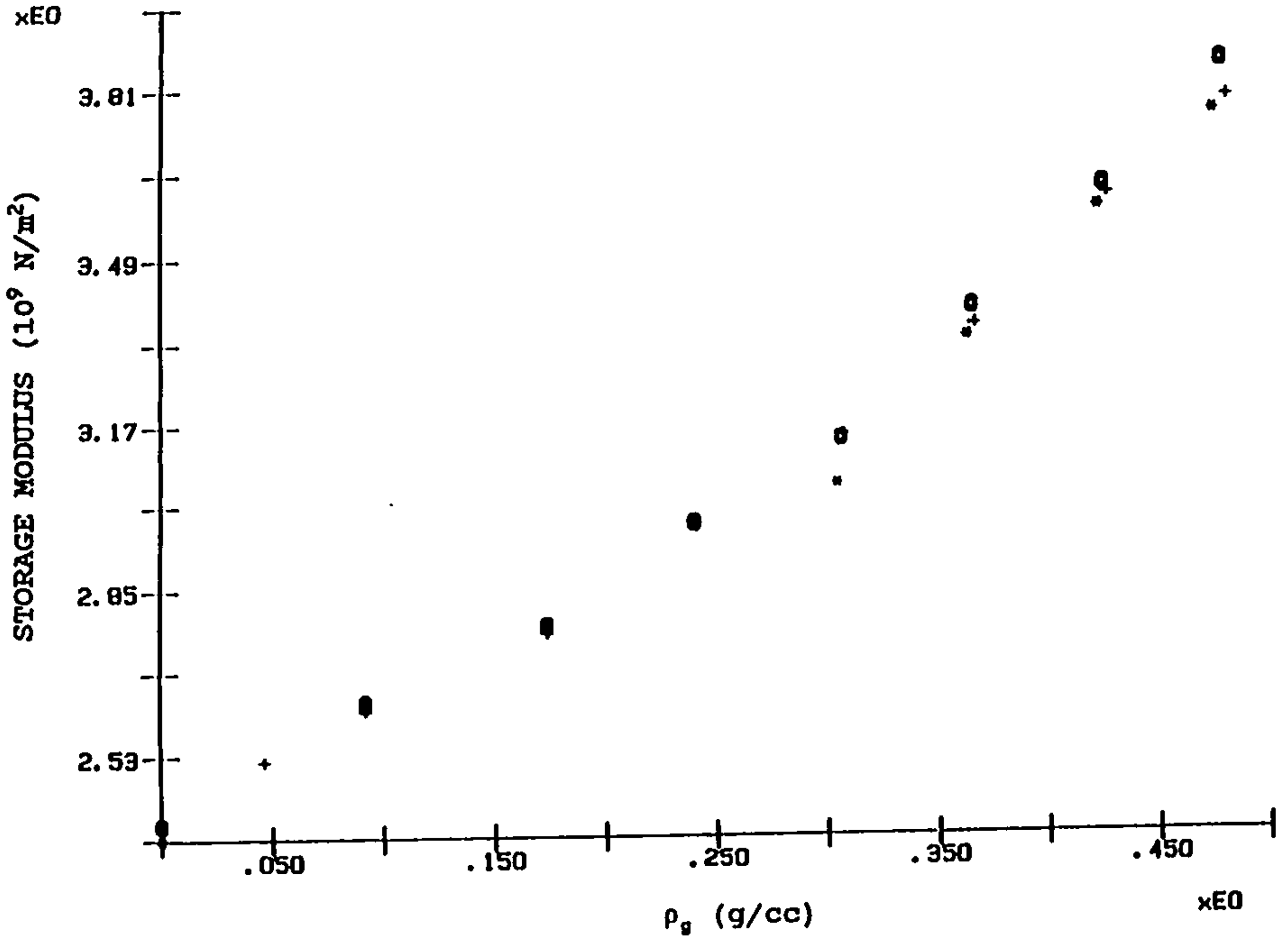

Fig. 3.30 Storage modulus M' versus ρ_g, T=50^{0}C (+), 55^{0}C (θ) and 61^{0}C (*).

$$M_f' = M_l' + A(1-\alpha)\rho_g \qquad (90)$$

i.e. $A(1-\alpha)\rho_g$ represents the contribution of the gelatin molecular residue to M_f. v_f is given by

$$v_f^2 = \frac{M_f'}{\rho_f^0} = \frac{1}{\rho_f^0}\left[M_l' + A(1-\alpha)c\rho_l \right] \qquad (91)$$

It should be emphasized that since the value of A is obtained from the experimental data at ρ_g<0.3g/cc, strictly speaking, the following calculation is only suitable in this concentration region. However, I will extend the results to higher concentration region and check their behaviour.

λ, α, v_n and f

There are four unknown parameters in equations (86) and (87): v_n, f, λ and α. Two equations are not enough to determine all the parameters. Actually, in M-D theory there is another formula — an expression for diffusion mode as a function of λ and f. Unfortunately, I do not have the experimental data. However, the reasonable λ and α can still be figured out within a certain range considering the following physical requirements to them.

Firstly, v_n should decrease with increasing temperature but increase with concentration since a higher concentration usually means an increased number of entanglements which will tend to increase v_n (de Gennes, 1979). Secondly, f should be large enough to meet the requirement of the strong friction limit. Also, it is expected that f is concentration and temperature dependent since the friction constant f is related to the viscosity of the gel liquid (water + residues) (Tanaka, 1973), which is a function of temperature T and the residue concentration in the gel liquid c_r. A higher concentration sample should have larger c_r, which will yield a larger friction constant. Thirdly, α should approach 1 at low temperature and decrease with increasing temperature.

In figures 3.31 and 3.32, I plotted the curves of v_n vs. c for various λ and α by using the experimental data of 22^{0}C. It can be seen that λ=0, or small α even at λ=1 causes v_n to decrease with increasing c at low concentration region, which obviously makes no sense. So, there must exist a low limit for λ and α. If α=1 the minimum value for λ is 0.006, and if α= 0.5 it will be 0.07. Although v_n is only weakly λ-dependent except for low values of λ, f increases with λ. In this case, a large λ seems to be a more suitable choice. Also, it provides the best prediction that v_n should smoothly approach zero as $c \to 0$. The reasonable α_{min} for λ=1 can be found for different temperatures, which are listed in table 3.3.

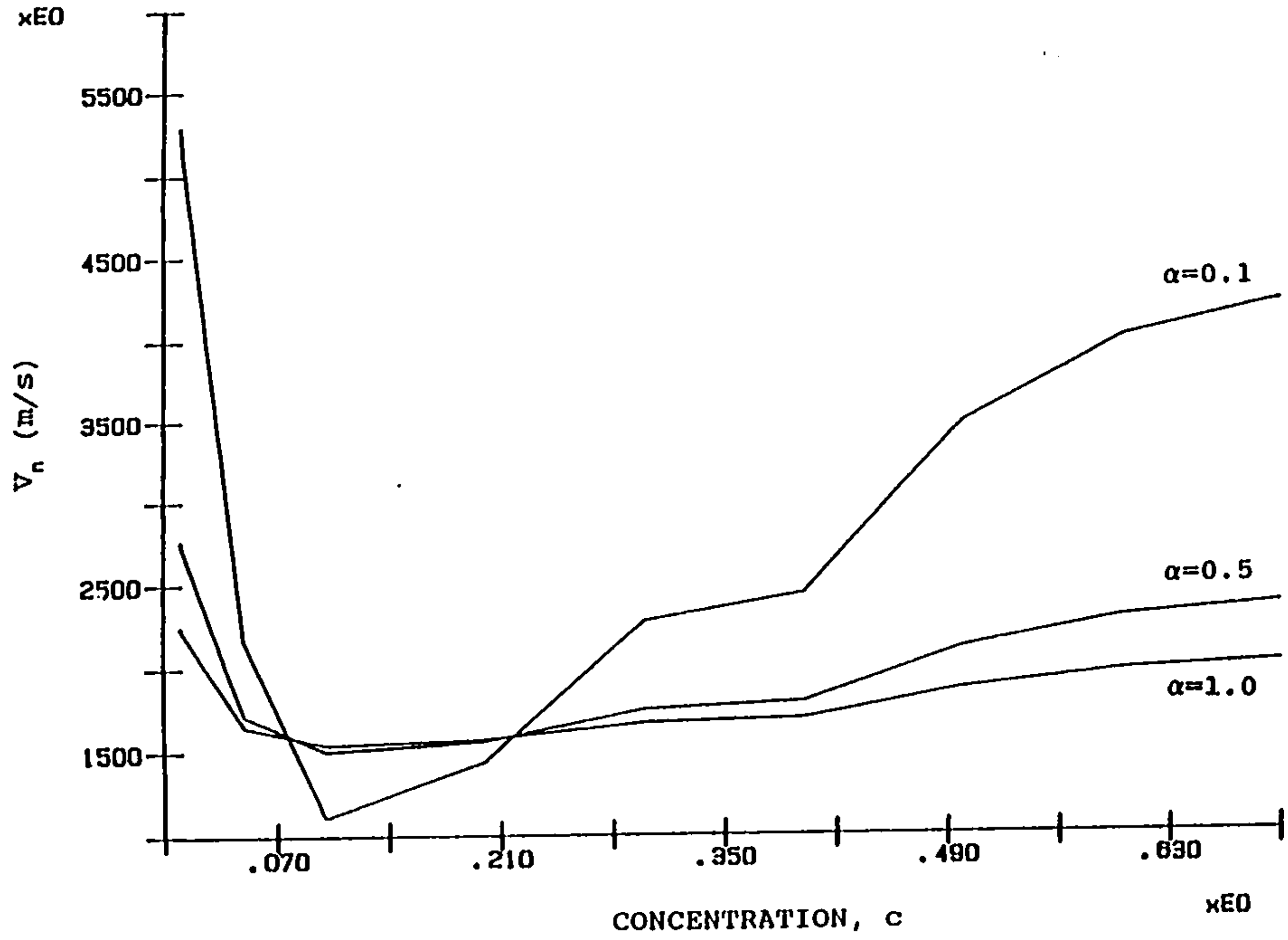

Fig. 3.31a v_n vs c for various α, λ=0, where v_n's are calculated from the experimental data at 22°C by using model 2.

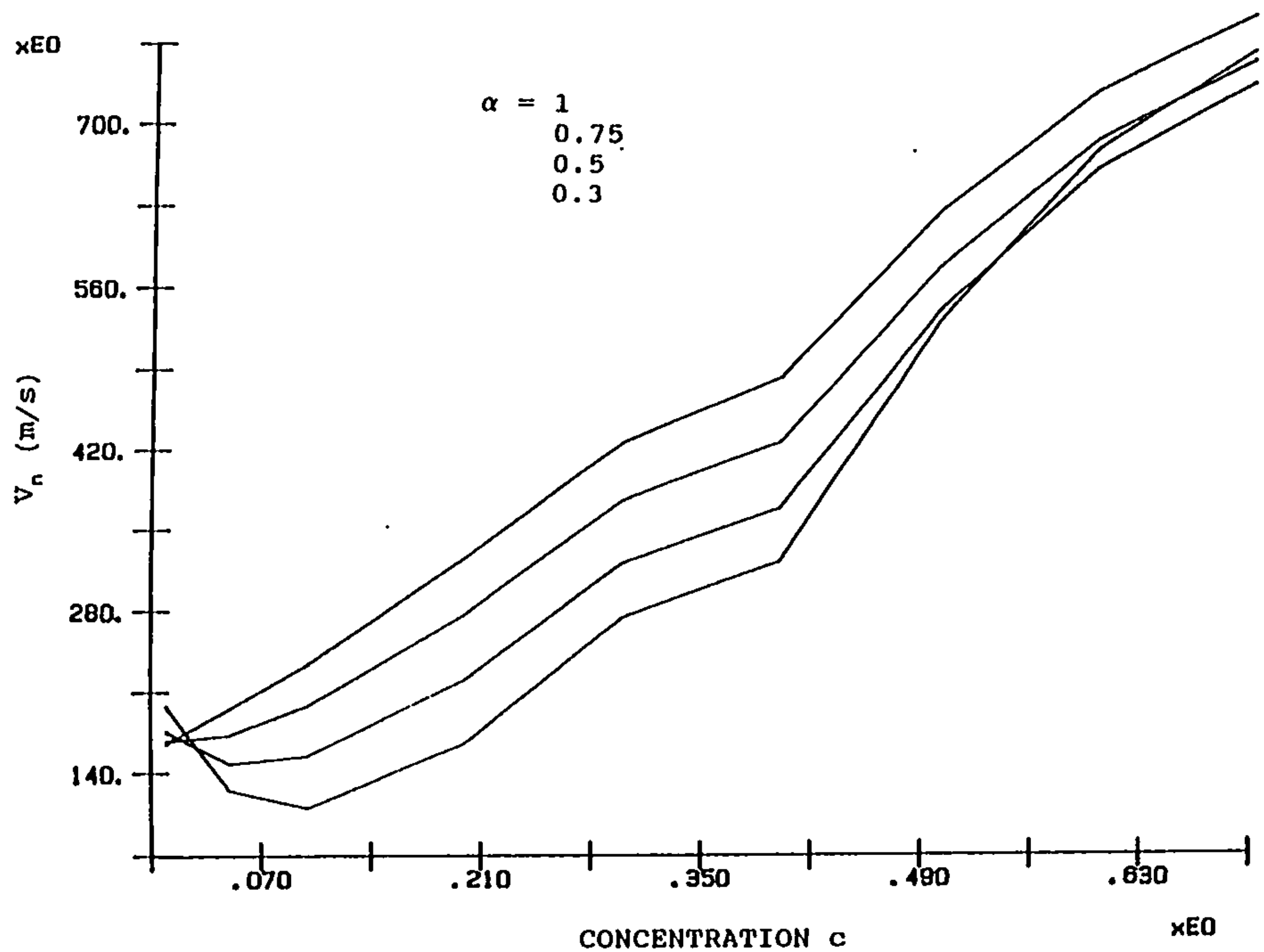

Fig. 3.31b v_n vs c for various α, λ=1.

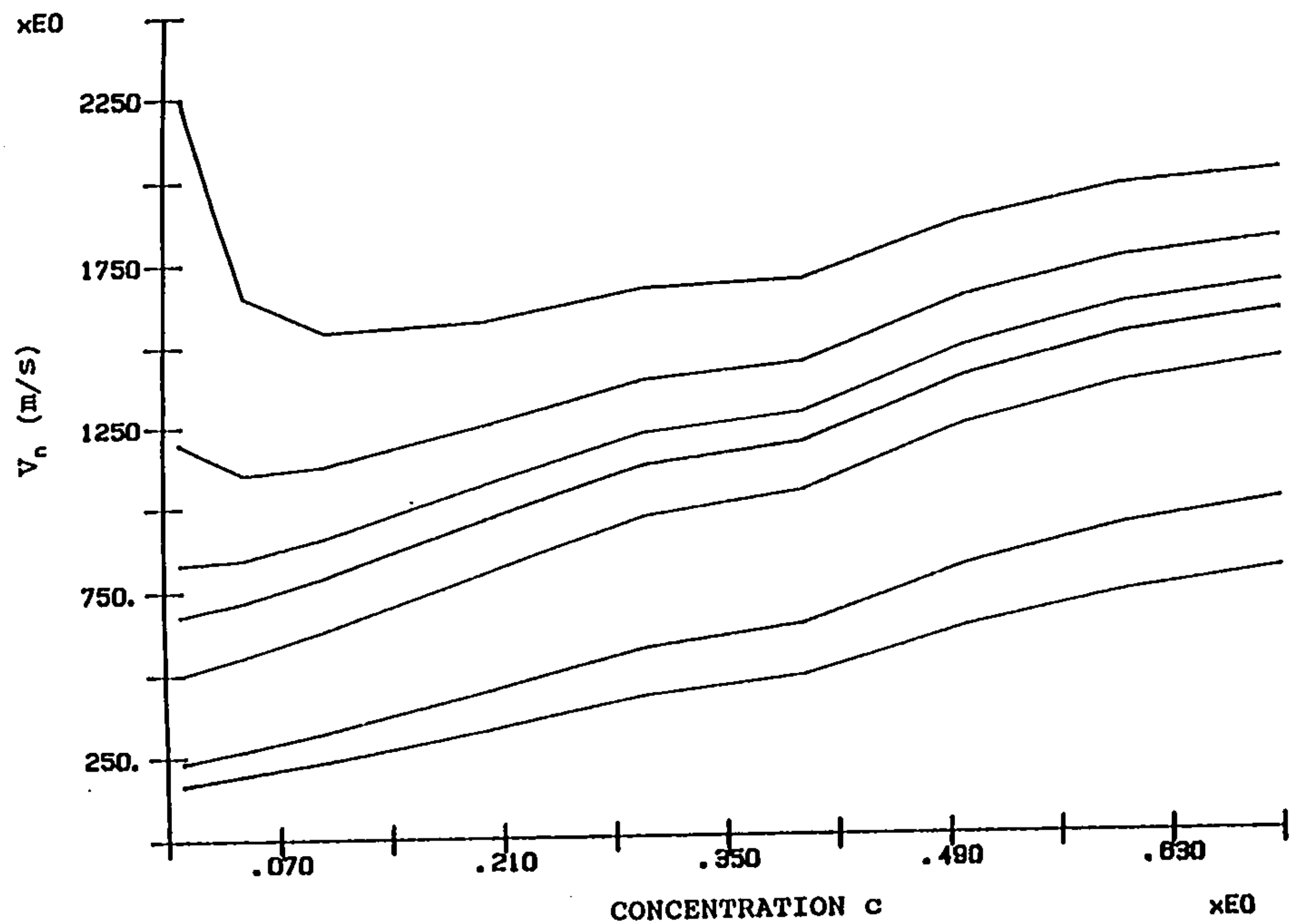

Fig. 3.32 v_n calculated from the experimental data at 22°C by using model 2, $\alpha=1$ and $\lambda=0$, 0.01, 0.03, 0.05, 0.1, 0.5 and 1 (from top to bottom).

Table 3.3 The reasonable α_{min}

T°C	2	22	26	28
α_{min}	.87	0.46	0.36	0.32

There exists a linear relation between α_{min} and T:

$$\alpha_{min} = 0.9733 - 0.0233T \tag{92}$$

This equation expresses the phenomenon that at gelation temperature not all the gelatin molecules are connected to form the network. As the temperature decreases, more and more gelatin molecules attach themselves to the network. Moreover, above 42°C there is no network, otherwise α_{min} will be negative, which is in agreement with the common experience that above about 40°C the gelatin-water system is in the sol state (Godard et al., 1978).

I calculated v_n and f for various temperatures within the limit of α. The α I chose for various temperatures are listed in Table 3.4.

Table 3.4 Mass fraction at various temperatures

T°C	1	14	22	26	28	32
α	0.955	0.64	0.46	0.36	0.32	0.23

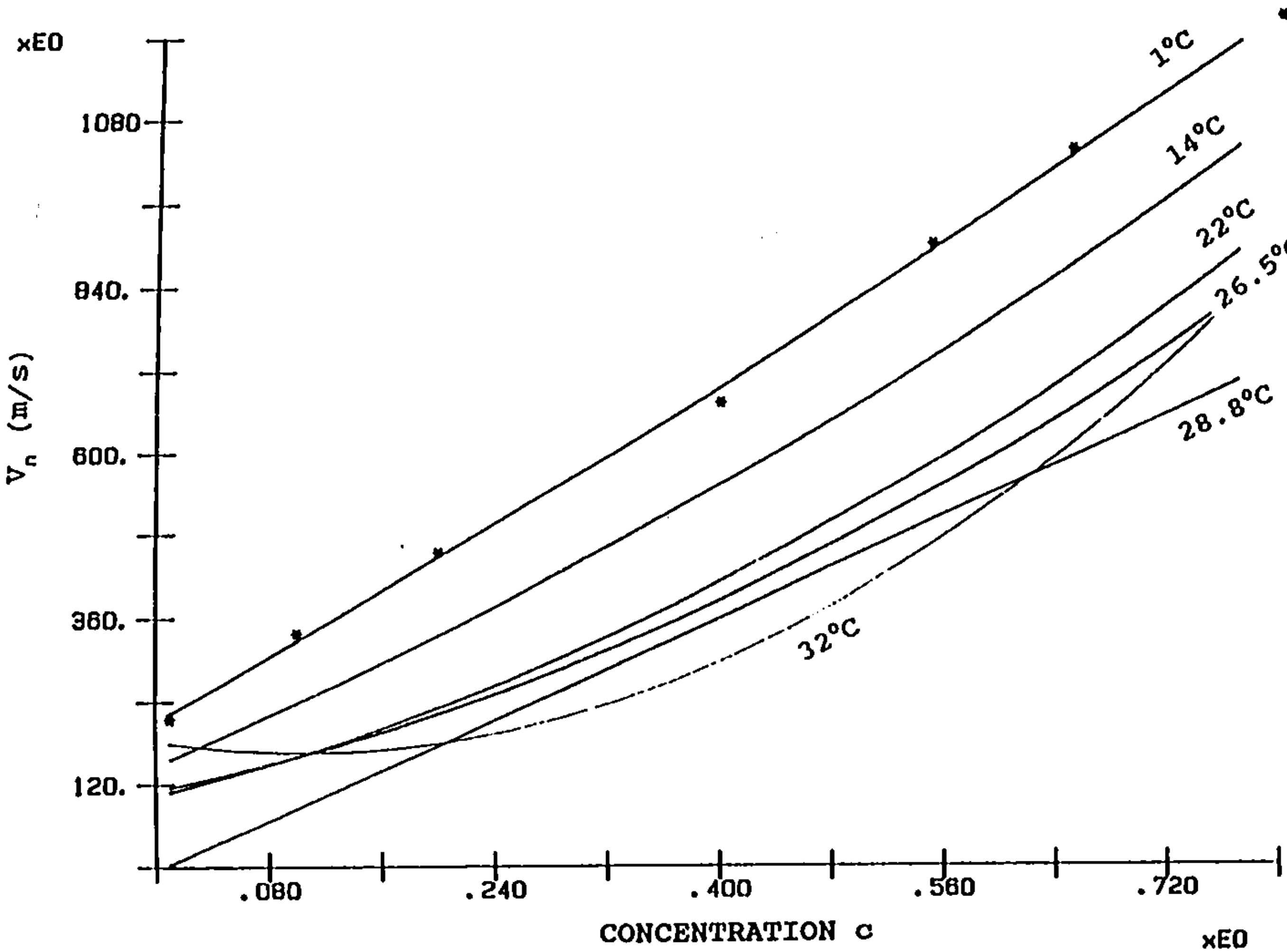

Fig. 3.33 v_n vs. c for various temperatures. $\lambda=1$ and α varies with the temperature (Table 3.4). *'s are the calculated data (T=1°C) and the solid lines are the best fitting curves to the calculated data.

v_n's Behaviour and Successful Explanation to M'

It can be seen from Fig. 3.33 that except for the curve for 32^{0}C, v_n increases with concentration and decreases with temperature as expected, which can be used to explain the different behaviours of the Brillouin shift (or sound velocity, storage modulus) at different concentrations when temperature changes (Fig. 3.10 and Fig. 3.14).

For λ=1, Eq. (77) becomes

$$\rho_T v^2 = (v_f\sqrt{\rho_f^0} + v_n\sqrt{\rho_n^0})^2 \tag{93}$$

or

$$\sqrt{\rho_T}\, v = \sqrt{M'} = \sqrt{M'_f} + \sqrt{M'_n} = \sqrt{M'_l + A(1-\alpha)\rho_g} + \sqrt{\alpha\rho_g}\, v_n \tag{94}$$

According to this equation, at a certain concentration the change of the sound velocity Δv with temperature depends on the changes of M'_f and M'_n with T. When temperature increases, M'_l increases but α and v_n decreases. At low concentrations, the main contribution to Δv is from the M'_f term, which increases with T. In the high concentration case, the change of M'_n is larger than the change of M'_f, which causes the decreasing of M' when temperature increases. At intermediate concentrations, these two opposite contributions compensate each other and v (or M') looks like independent of T.

The v_n curve for 32^{0}C has a drop between c=0.05 and c=0.1, which denotes that at that temperature the low concentration samples are in the sol state.

f's Behaviour and the Problem

The temperature and concentration-dependent behaviour of the friction constant predicted by this model is shown in Fig. 3.34, where I omitted the term $\Delta\eta$.

It can be seen that (a) f increases with concentration monotonously at 32^{0}C, but at low temperatures it increases first, then decreases, and the maximum position increases with T; (b) f is not large enough to satisfy the criterion of a strong frictional damping limit. If I add the term $\Delta\eta$ using the same way as I did for fluid velocity — letting $\Delta\eta$ equal to $B(1-\alpha)\rho_g$ and taking the slope of the fitting line of the viscosity vs. ρ_g at 61°C (ρ_g<0.3g/cc) as the value of B (8.4×10^{-6} m^2/s), f will be larger but its shape will still be the same (Table 3.5).

What causes this up and down behaviour?

One possibility is that this model neglects the sound attenuation within the fibres of the network itself since Eq. (78) only includes the intrinsic attenuation in the fluid (the first term) and the attenuation due to the relative motion of the fluid against the network (the second term). Now, let us add this attenuation in Eq. (78), and therefore in Eq. (87),

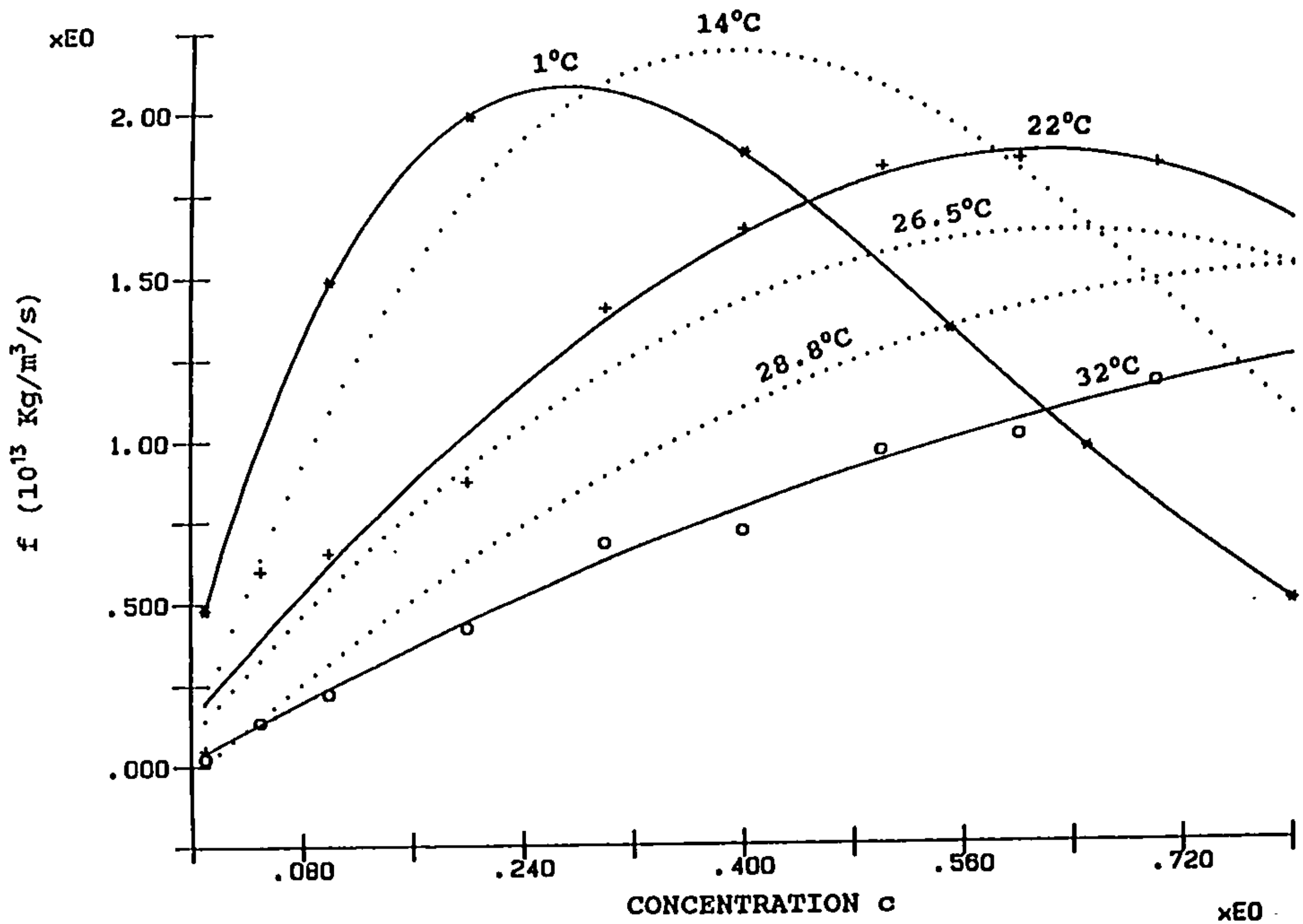

Fig. 3.34 Friction coefficients for various temperatures, λ=1 and α varies with the temperature (table 3.4). "*", "+" and "o" denote the calculated data (T = 1°C, 22°C and 32°C, respectively) and the solid and dotted lines are the best fitting curves to the calculated data.

to see if the shape will have any change.

Table 3.5 Friction coefficients (10^{13} Kg/m^3/s)

		c				
		0.01	0.1	0.2	0.4	0.55/0.5
T	$\Delta\eta=0$	0.480	1.488	1.988	1.873	1.334
1°C	$\Delta\eta\neq0$	0.487	1.510	2.016	1.898	1.334
T	$\Delta\eta=0$	0.050	0.650	0.870	1.643	1.828
22°C	$\Delta\eta\neq0$	0.055	0.968	1.143	2.221	2.393

Assuming this additional term can be expressed as

$$2\rho_n^0\Gamma_n = 2\alpha c\rho_l\Gamma_n \equiv 2\alpha c\rho_l\Gamma_{Bn}\pi/q_n^2 \qquad (95)$$

where Γ_n denotes the intrinsic attenuation in the network. When $c = 0$, $\Gamma = \Gamma_w$; and when $c \to \infty$ ($\rho_l \to 0$ and $c\rho_l \to \rho_t=\rho_s$), Γ approaches Γ_s, where Γ_s is the sound attenuation in the dried sample. Γ_n should depend on concentration, but the relation between Γ_n and c is not clear. For simplicity, I treated it and q_n as constants, and calculated f of 1°C at various values of Γ_n with $\Delta\eta=0$ (Fig. 3.35) to get some idea of how big the influence of Γ_n on f is. It can be seen that adding the attenuation term due to the network yields a larger friction constant but does not solve that up and down problem.

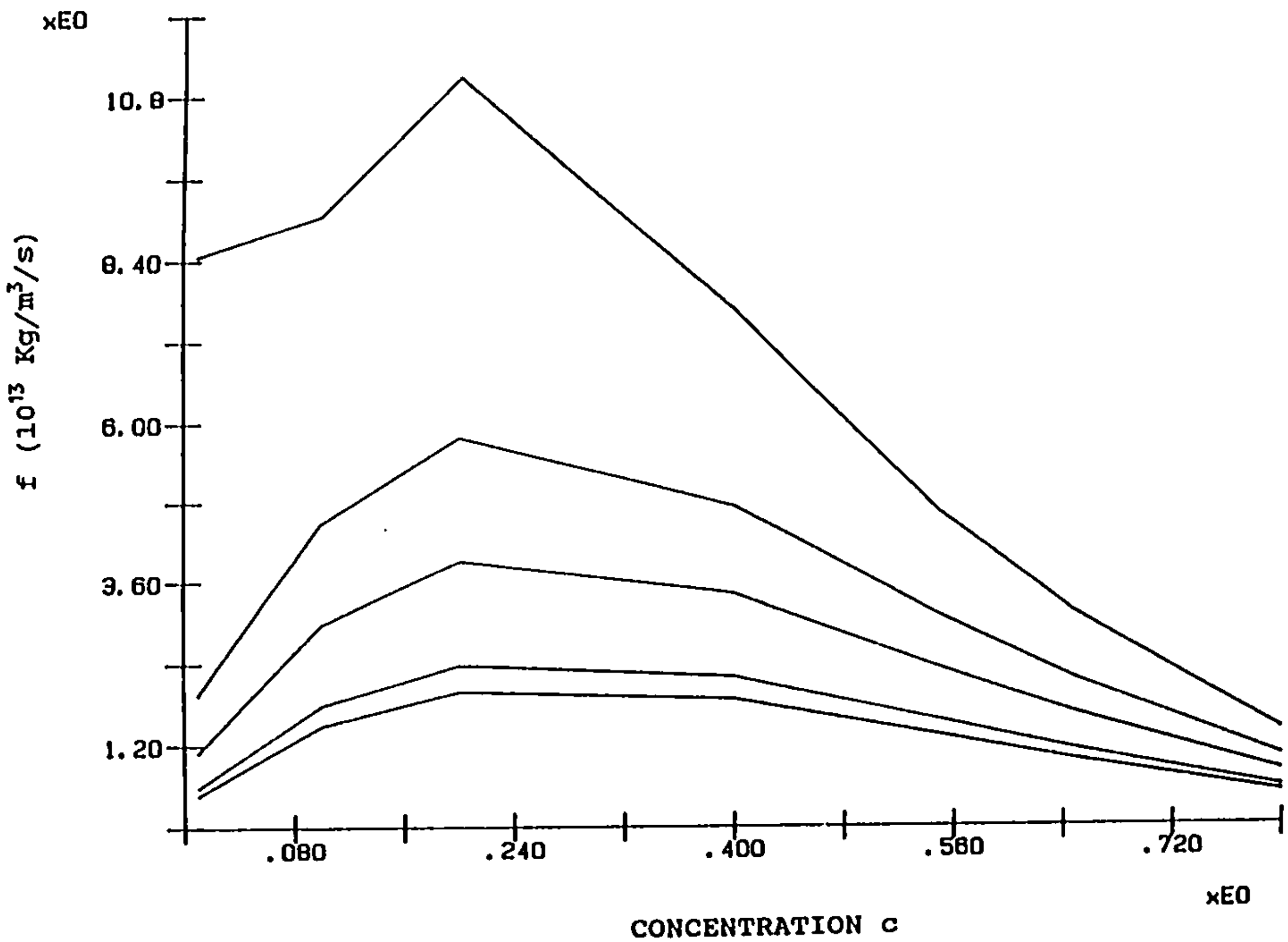

Fig. 3.35 Friction coefficient at T=1°C when Γ_{Bn} is given different values: 5, 4, 3, 1 and 0 GHz (i.e. Γ_n = 11.75, 9.40, 7.05, 2.35 and 0 $10^{-6} m^2/s$, from top to bottom), where λ=1 and α=0.995.

Another possibility is provided by Tokita. Tokita pointed out (1993) that gel can become inhomogeneous due to the density fluctuations frozen in the gel when the cross-linker concentration is increased. In such case, the frictional property is mainly governed by the spatial correlation length of the density fluctuations rather than by the average cross-length density of the gel, hence the friction decreases upon increasing the cross-linker concentration. I am not sure if this is a good explanation to that up and down problem.

When temperature drops, more and more gelatin molecules are connected to the network, and c_r becomes smaller and smaller. These two factors of lower T and smaller c_r give opposite influence on fluid viscosity. The temperature dependent behaviour of f will depend on which one of these two factors is dominant.

At last, I would like mention two things. One is the water populations in the gel state. In the gel-state the water molecules can be divided into three fractions (Djabourov et al., 1987): (a) the free water; (b) the bound water bound to the coils or to the aggregations of triple helices exposed to the free solvent; (c) the structural water made up of molecules which are bound to the chains in order to stabilize the triple helices or the aggregates of triple helices (Maquet, 1986). If we think part of the water participates in the formation of the network, we should adjust the values of

ρ_f° and ρ_n° used above: let ρ_f° be smaller and ρ_n° be larger, which is equivalent to a larger c. The result of this adjustment will make v_n larger, and f larger too in the low concentration region.

Another thing is that the values for α (therefore the value for v_n and f) are not unique. Indeed, if I choose a larger α, f will be larger. However, since α is already close to 1 for 1^0C, an arbitrary larger α at higher temperature will cause an increase in f with increasing temperature, which is undesirable.

Comments

From the discussion above, we can see that this model can successfully explain the experimental results of the temperature dependence of the storage modulus, and produce the reasonable v_n-T, v_n-c behaviour. But, its prediction to friction coefficient may be a problem. There are too many unknowns and too many parameters which makes it hard to get quantitative information.

It needs to be pointed out that α should also be a function of time and thermal history. For a gelation process, α will increase with time as displayed by the results of the gelation experiment (Fig. 3.6 and Fig. 3.7). At the gelation time, which is the moment when the two large clusters are connected together to form an infinite network, there are still some unattached gelatin molecules (residues) left in the gel liquid. As time goes on, these residues will attach themselves to the network (α increases), which makes the modulus larger. High concentration samples have more residues, which will increase the modulus more after the gelation time. In general, $\alpha=\alpha(T,t)$ and the above is the situation when $t \approx 4$ hours.

This model was used by some groups to analyze their experimental data (different materials) (Ng et al., 1985b; Kato, 1987; Brown et al., 1991; Ng et al., 1993), but none of them considered the temperature influence on the network density and the influence of the gelatin residues on v_f and fluid viscosity. So, my discussion is more thorough than theirs.

3.4.3 Model 3

D. L. Johnson's theory (1982a) for elastodynamics of gels is based on Biot's theory of acoustics in fluid-saturated porous media (Biot, 1956). Johnson treated the three-dimensional displacements of the solid and fluid parts of gels separately and on an equal footing, and gave generally complex expressions for two independent longitudinal modes —— the "fast" and "slow" waves —— and two transverse waves.

As in the model 2, two extreme cases are considered:

high-frequency limit $\nu \gg \nu_c$ and low-frequency limit $\nu \ll \nu_c$, where ν_c is the crossover frequency (Johnson, 1982a; Hosea et al., 1986a)

$$\nu_c = \eta_s / (\pi \rho_f r^2) \tag{96}$$

The crossover from the former extreme to the latter occurs when the viscous skin depth,

$$\delta_0 = [\eta_s / (\pi \rho_f \nu)]^{\frac{1}{2}} \tag{97}$$

of waves of frequency ν, exceeds the average width r, of the reticular channels through which the fluid, of shear viscosity η_s and density ρ_f, must flow.

In the high-frequency limit, if the networks are stiff (K_b, $G \gg K_f$), two modes for longitudinal waves can be seen and the velocities are:

$$v(fast) \approx \left[\frac{K_b + \frac{4}{3} G}{\phi \rho_s + (1 - \alpha_0^{-1})(1 - \phi) \rho_f} \right]^{\frac{1}{2}} \tag{98}$$

$$v(slow) \approx (K_f / \rho_f \alpha_0)^{1/2} = v_f / \alpha_0^{1/2} \tag{99}$$

where K_b and G are the bulk and shear moduli of the network, K_f the fluid bulk modulus, ϕ the volume fraction of the gel network (note: ϕ is not the fluid volume fraction as in Johnson's paper), ρ_s the solid density, and α_0 the tortuosity parameter which is related to the hydrodynamic drag parameter

λ by $\alpha_0 = (1-\lambda)^{-1}$ with $0<\lambda<1$. The total density, ρ_T, will be

$$\rho_T = (1-\phi)\rho_f + \phi\rho_s \tag{100}$$

If the networks are negligibly weak, $K_b = G = 0$, the slow wave is absent (it is diffusive, rather than propagating) (Johnson, 1982b), and

$$v^2(fast) = \frac{K^*}{\alpha_0\rho_f}\left[\frac{\phi(1-\phi)\rho_s + (\alpha_0 - 1 + \phi^2)\rho_f}{\phi\rho_s + (1-\alpha_0^{-1})(1-\phi)\rho_f}\right] \tag{101}$$

where K^* is the bulk modulus of the suspension (Wood, 1964),

$$1/K^* = (1-\phi)/K_f + \phi/K_s \tag{102}$$

and K_s is the bulk modulus of the solid in its bulk form.

The unconsolidated speed in Eq. (101) is not particularly sensitive to α_0, as α_0 varies from 1 to ∞. If $\alpha_0 \to \infty$, Eq. (101) becomes identical to Wood's formula,

$$v(fast) = v_0 = (K^*/\rho_T)^{1/2} \tag{103}$$

In the low-frequency gel limit (K_b, $G \ll K_f$, K_s), the velocity and attenuation are

$$v(fast) = v_0\left[1 + \frac{K_b(1-K^*/K_s)^2 + \frac{4}{3}G}{2K^*}\right] \tag{104}$$

$$\gamma = \frac{v^2 q^2}{2v_0\rho_T}\left[\frac{\eta_v + \frac{4}{3}\eta_s}{v_0^2} + \frac{k}{\eta_s}\phi^2(\rho_s - \rho_f)^2\right] \tag{105}$$

respectively, where k the fluid permeability which is a geometrical quantity presumed to be independent of fluid viscosity (biot, 1956), and q the hypersonic wavevector.

Since there exists the relationship between the attenuation γ and Brillouin width Γ_B and loss tangent tgθ,

$$\gamma = \frac{\pi\Gamma_B}{v} = \frac{q}{2}tg\theta \tag{106}$$

Eq. (105) can be rewritten as

$$tg\theta = \frac{v^2 q}{v_0^3 \rho_T} \times \frac{2\rho_v \Gamma_{Bv} \pi}{q_v^2} + \frac{v^2 q}{v_0 \rho_T}\frac{1}{b}\left[\phi(1-\phi)(\rho_s-\rho_f)\right]^2 \tag{107}$$

where

$$b = (1-\phi)^2 \eta_s / k \tag{108}$$

Comparing to model 2, it can be seen that the high frequency limit corresponds to the small friction case of the M-D model and the low-frequency limit corresponds to the strong friction case. The two important parameters, v_n and f in the M-D model are related to the K_b, G and k, η in the DJ model by

$$\begin{aligned} v_n &= \left[(K_b + \frac{4}{3}G)/\rho_n^0\right]^{1/2} \\ f = b &= (1-\phi)^2\eta_s/k \end{aligned} \tag{109}$$

It should be mentioned that there will be some difficulties or extra uncertainties to use this model (JD model) to analyze my experimental data: (a) my experiments only offered the information about longitudinal waves, it is impossible for me to split it into two parts, bulk and shear parts, to proceed with the calculation, unless some value for the Poisson's ratio is assumed. (b) the K_s was deduced from the Brillouin shift of the dried sample at room temperature, which may not be the same as the bulk modulus of the solid particles (gelatin) in suspensions. However, the real problems to use this model is as follows.

Since there are two choices, high-frequency weak network limit and low-frequency gel limit, which all match my experimental results (one mode for longitudinal wave), the first thing is to decide which limit I should use to analyze the data. It can be done by comparing ν with ν_c to see which one is larger. According to Johnson's paper (1982a) the typical value of r is ~100Å. I estimated the up limits of r for various concentrations using the formula $r<(m_w/\rho_g)^{1/3}$. The corresponding low limits of crossover frequencies are listed in Table 3.6, where $\eta_s=10^{-3}$ kg/m/s was used. These low limit values of ν_c are too small to meet the requirement of the low-frequency gel limit.

Table 3.6 Estimated low limit values of ν_c

c	0.01	0.1	0.2	0.4	0.55	0.65	0.8
r <	237Å	112	91	75	69	56	62
ν_c >	.56GHz	2.51	3.82	5.62	6.70	7.36	8.28

As to the high-frequency weak network limit, it has its problem when it is used to analyze my data, which will be explained below.

At 55^0C, the gelatin-water system is in the sol state, i.e. the system is a suspension, so Eq. (102) can be used to calculate its bulk modulus. Now ϕ is the volume fraction of the gelatin solid particles and

$$\begin{aligned} \rho_g &= \phi\rho_s \\ \rho_l &= (1-\phi)\rho_w \end{aligned} \tag{110}$$

where ρ_w is the pure water density. From the measured data ρ_l and ρ_g, ϕ and ρ_s can be calculated. The average value for ρ_s is about 1.483 g/cc.

Table 3.7 A comparison between M' and K^* (55°C)

c	0	0.1	0.2	0.3	0.4	0.5	0.6	0.7
ϕ	0	0.062	0.118	0.168	0.221	0.252	0.282	0.304
M'/K^*	1	1.040	1.045	1.067	1.069	1.121	1.159	1.204

Longitudinal storage modulus for dried samples, M'_s, was used to calculate K_s, where the Poisson's ratio,

$$\sigma=(3-M/K)/(3+M/K),$$

of 0.4 for many plastics was taken which led to $M'_s= 9K_s/7$ and $K_s=1.36\times10^{10}$ N/m^2. The values of calculated K^* are smaller than that of the corresponding longitudinal modulus, and the ratio of M'/K^* increases with concentration (Table 3.7). That is to say, even at 55°C (in the sol state), the shear modulus is not equal to zero. Although, the ratio of M'/K^* can be larger or smaller than those values given above, depending on the value of K_s used (or the Poisson's ratio chosen), unless K_s is negative, which of course makes no sense, M' is always larger than K^*. Because of this, I do not think the high-frequency and weak network limit is suitable for me to use except at real low concentration.

To sum up, the high-frequency and weak network limit is not suitable for this system, and the crossover frequency may not be large enough to let one use the low-frequency gel limit in the hypersonic frequency region. Considering of this and other uncertainties mentioned above, I will not do more calculations.

3.4.4 Thermodynamical Behaviour

The relation between T_m and c has already been determined (Fig. 3.13). Now, I can use this result and the formula (111) derived by Eldridge and Ferry (1954) to calculate the melting enthalpy.

$$\frac{d\ln c_w}{dT_m} = -\frac{\Delta H^0}{R_g T_m^2} \tag{111}$$

where ΔH^0 is the melting enthalpy, the heat of reaction required to break a cross-link between two potential junctions, R_g is the gas constant, and the units of T_m and concentration c_w are K and %w/w, respectively. This equation can be rewritten as (Michon, 1993)

$$\frac{d\ln c_w}{d(\frac{1}{T_m})} = -\frac{\Delta H'}{R_g(1-\frac{1}{2}f')} \qquad (112)$$

where ΔH' is the sum of the ΔH° of the f'/2 chain segments which form the junction zone and f' is the functionality (the number of bonds that a monomer can form). For gelatin, f'=6 since the junction zones in gelatin result from the formation of triple helices.

The logarithmic plot of concentration vs. reciprocal melting temperature is shown in Fig. 3.36. It appears almost as a straight line except for the lowest concentration (<1%) point, which means that the melting enthalpy is a constant in the concentration range of 1% to 33%.

The melting enthalpy calculated from the slope of the straight line is 684 KJ/mol, which is close to the value reported by Michon's group (1993).

Using the same analysis as te Nijenhuis' (1981), in which ΔH° of a folding process equals to 18.3 KJ/mol and 9 windings correspond with a length of 86Å, I calculated the mean number of windings per helix in a cross-link, which turns out to be equal to 35.4. The average length of the cross-links is 338Å.

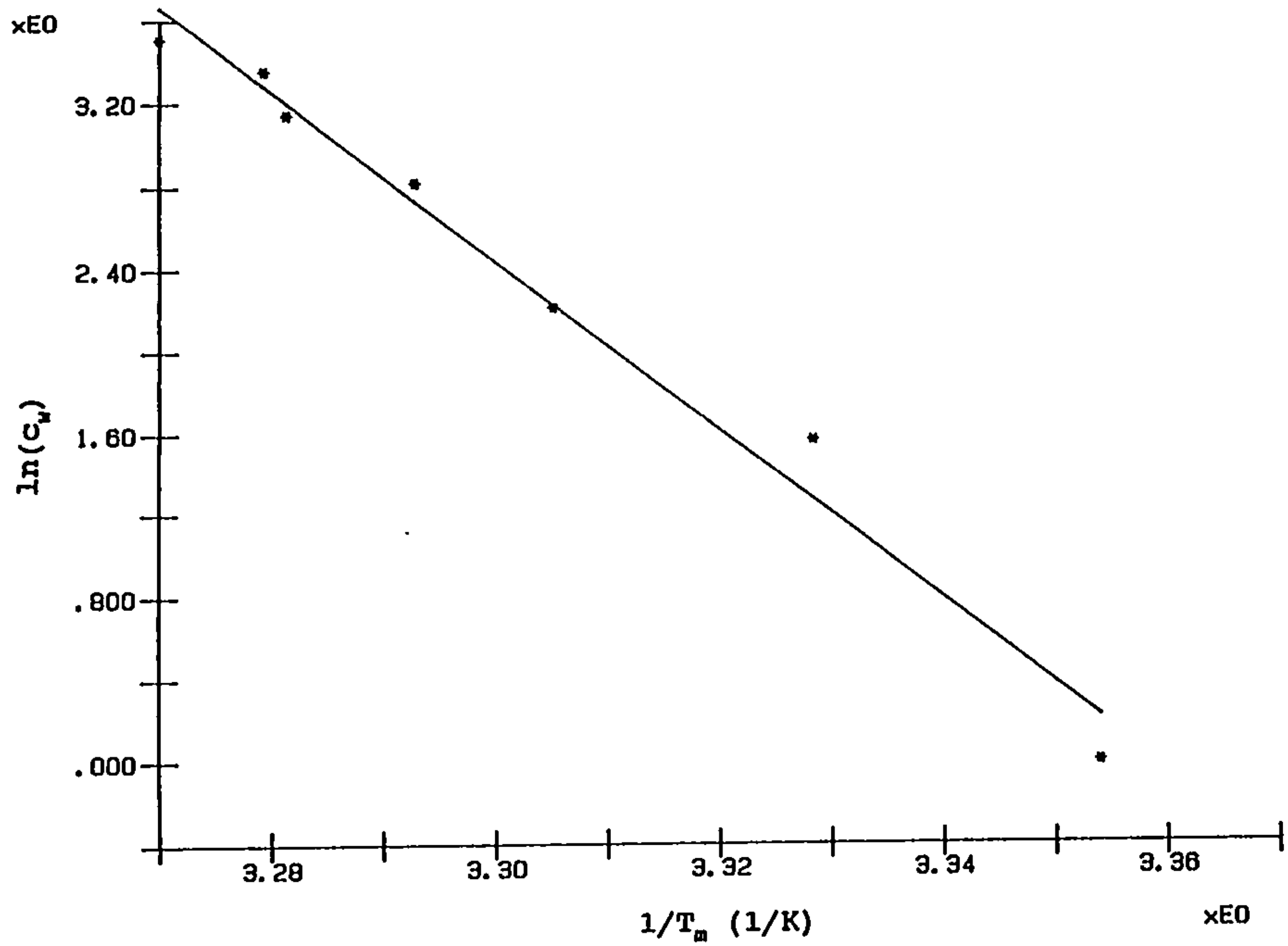

Fig. 3.36 The logarithmic plot of concentration vs. reciprocal melting temperature.

3.5 Summary

I believe that this is the first detailed report of Brillouin spectroscopy of gelatin gel. The new results I got include:

—— Thermal history (cooling rate) effects the eventual (equilibrium) state: fast cooling yields smaller crystalline regions, therefore, smaller sound velocity (Brillouin shift) and attenuation (width); also, the higher the concentration, the larger the difference (Figs. 3.8 and 3.9)

—— Concentration effects the behaviour of temperature dependence of the sound velocity (Brillouin shift, longitudinal storage modulus): sound velocity increases with increasing temperature at low concentration, but decreases at high concentration (Fig. 3.10), which gives us a hint that the sound velocity in network should decrease with increasing temperature.

—— Sound attenuation increases with decreasing temperature for all the concentrations and the curves of the Brillouin width against temperature consist of two straight segments for dilute and intermediate concentrations (Fig. 3.11). The low temperature part has a larger slope, which indicates there is an extra attenuation in the gel state. As to its mechanism, different model has different explanation. According to the model 1, the cross-section between phonon and the gelatin molecule in the network is larger than that between phonon and the gelatin molecule in the solution, which cause the extra attenuation. Model 2 and 3 attribute it to the attenuation due to the relative motion of the fluid against the network and the friction between them.

—— Brillouin shift and width increase with increasing concentration linearly and the linear relations break down at concentration about 0.4. The higher the concentration, the larger the slope. The v_B-c curves for various temperatures below about 40°C intersect each other in the region around 0.25, but the Γ_B-c curves diverge (Figs. 3.16 and 3.17).

As to the models, an empirical formula for loss tangent was obtained from model 1, which fitted the experimental data quite well (Figs. 3.25 and 3.26); model 2 gave out a successful explanation to the behaviour of storage modulus-temperature dependence (page 100); but, there are some difficulties to use model 3 to analyze my data.

Since models 1 and 2 are based on different assumptions and theories, to obtain different values for M'_n from the different models is not strange. It simply shows that one or both of the models are not perfect. As a comparison, I listed the results of 1°C in Table 3.8 (row 2 and row 5). It can be seen that the value of the M'_n of model 1 is much larger than that of model 2. I can make the M'_n of model 2 larger by choosing a smaller λ, e.g., λ=0.5 (Table 3.8, row 4). However, it will yield a smaller f.

The M'_n of model 1 will be smaller if the first term in Eq. (54), K_f, is timed by a constant, β, larger than 1, i.e.

$$M' = \beta K_f + M'_n(\alpha(T)\phi) \tag{113}$$

which I think is reasonable considering the following fact.

At 55°C, $\alpha(T) = 0$ and Eq. (53) turns to be

$$K_f = K_w / [1-\phi(1-r)] \tag{114}$$

At this temperature, M'_n should be equal to zero since there is no network existing. However, the calculated K_f does not equal to M', the experimental data, — the same problem discussed in model 3 (Table 3.7).

Table 3.8 Network moduli at 1°C, calculated from different models, with different parameters

c		0.01	0.1	0.2	0.4	0.55
M'_n	model 1	0.035	0.263	0.515	1.090	1.785
	model 1 with β		0.180	0.409	0.937	1.491
	model 2, λ=0.5	0.001	0.019	0.063	0.231	0.506
	model 2, λ=1	.0004	0.010	0.035	0.137	0.317

where the unit of M'_n is 10^9 N/m^2, the row "model 1" shows the data calculated from Eq. (54).

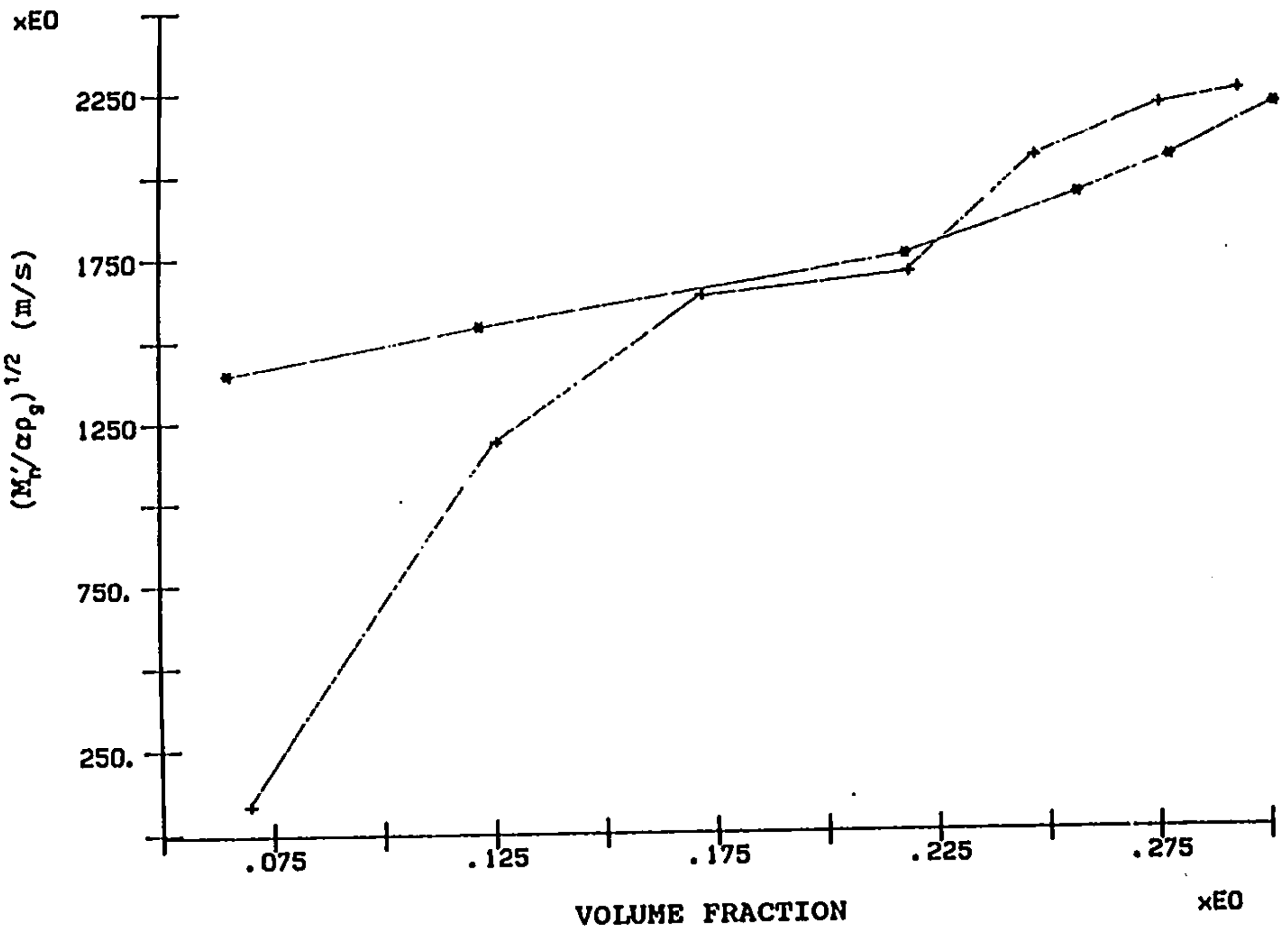

Fig. 3.37 Corrected $(M_n'/\alpha\rho_s)^{1/2}$ at 1°C (*) and 22°C (+).

If I let β equal to M'/K_f (i.e. M'/K^* in Table 3.7), M'_n will be smaller (Table 3.8, row 3). Also, the problem of positive temperature dependence of $(M'_n/\alpha\rho_g)^{1/2}$ can be partly solved (Fig. 3.37).

The information I obtained about this gelatin-water system can be summarized as follows:

With the decreasing of temperature or the passage of time in gelation process, more and more gelatin molecules are connected together to form networks. However, at gel point not all the gelatin molecules attach to the network, some still remain in the fluid. There exists coupling between the fluid and the network.

In the gel state, the storage moduli of fluid and network both contribute to the longitudinal storage modulus of the system, and the former increases with temperature but the latter decreases with temperature. Sound attenuation includes three parts: the attenuations in the fluid and network, and the attenuation due to the relative motion of the fluid against the network. The friction coefficient is at least in the order of 10^{12} $Kgm^{-3}s^{-1}$, and it can be as large as $10^{14}Kgm^{-3}s^{-1}$. Tanaka (1973) and Tokita (1993) measure the friction coefficient of poly(acrylamide) gels by mechanical method and found its order-of-magnitude is from 10^{12} to 10^{14} $Kg/m^3/s$ depending on the concentration.

When gelatin-water system transits from gel state to sol state, heat is needed to break the cross-links between two potential junctions. The melting enthalpy was found to be 684 kJ/mol, corresponding with mono-helices of 35 windings and a length of 338Å.

As I mentioned above, in order to get more accurate values for all the parameters of this system and explain all the experimental data, a more perfect theory is need.

Chapter 4

Icosahedral Quasicrystal $Al_{63.5}Cu_{24.5}Fe_{12}$

The penetration of light into an opaque material is determined by the conductivity of the material. In the case of metals, where large numbers of conduction electrons shield the metallic interior, the bulk phonons can not be detected; however, you can see the surface mode in their Brillouin spectra, which is due to bulk phonon-induced mechanical perturbations or ripples on the surface of the solid. The magnitude of the overall optical conductivity of the Al-Cu-Fe quasicrystal in the visible range is typical of most metals, i.e., of the order of $10000\Omega^{-1}cm^{-1}$(Homes et al., 1991). Thus only surface phonons will be observed in the Brillouin spectrum. However, it is still possible to deduce the bulk elastic constants as explained in Chapter 2.

A polycrystalline sample of the $Al_{63.5}Cu_{24.5}Fe_{12}$, about $3\times2\times0.5mm^3$ in size, was used in this experiment. The sample was mechanically polished to reduce its diffuse scattering

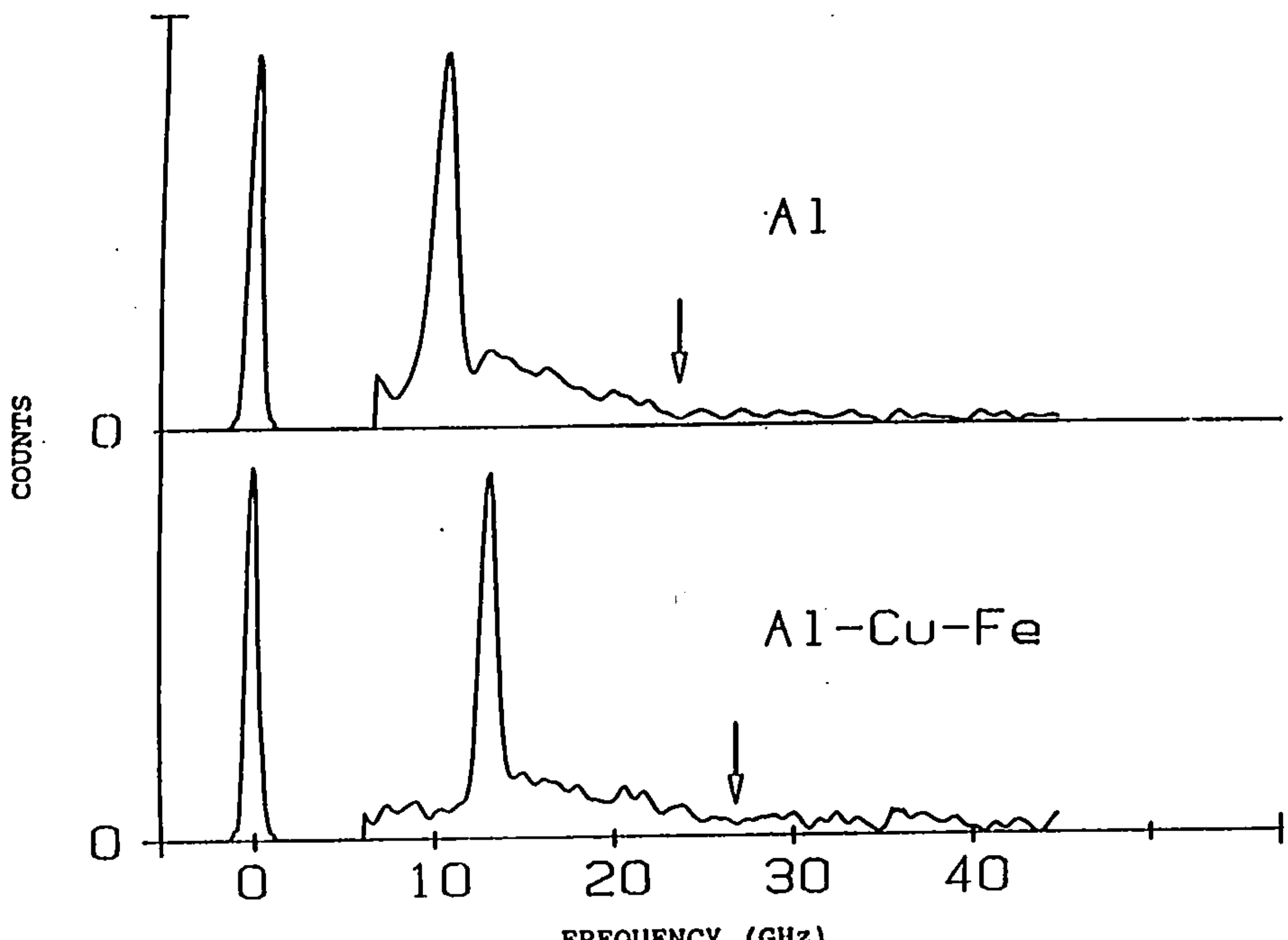

Fig. 4.1 Brillouin spectra of polycrystalline aluminum (top) and polycrystalline $Al_{63.5}Cu_{24.5}Fe_{12}$ (bottom) at room temperature. Arrows in both spectra indicate the position of $q_R v_l$.

intensity. For comparison, a polycrystalline sample of Al was also examined.

A similar experimental system as described in Chapter 3 was used in this experiment. The tandem FP was used in a five-pass configuration to increase the resolution. Back-scattering geometry was employed with an incident angle of 75°.

The Brillouin spectra at room temperature are shown in Fig. 4.1. They have the same characteristics as described in Chapter 1: a prominent Rayleigh surface phonon (~10^2 counts) and a broad shoulder with a minimum on it. Arrows in the spectra indicate the minimum positions of $q_R v_L/2\pi$. The elastic peaks at 0 frequency are of the order of 10^9 counts and have been scaled to the level of the Rayleigh surface mode phonon.

The surface wavevector q_R can be calculated using the formula (4). The experimental results are given in Table 4.1, where Γ_R is FWHM of the Rayleigh surface phonon peak.

Table 4.1 Experimental results

	ν_R(GHz)	Γ_R(MHz)	$q_R v_L/2\pi$(GHz)
Al	10.62	188	24
AlCuFe	13.25	93	27

From those data, the velocities of surface, longitudinal and transverse waves, v_R, v_L and v_T can be evaluated by using formula (7). The results are given in Table 4.2.

Table 4.2 Velocities of surface, longitudinal and transverse waves

	v_R(m/s)	v_L(m/s)	v_T(m/s)
Al	2829	6393	3022
AlCuFe	3529	7191	3809

The two independent elastic constants c_{11} and c_{44} can be calculated by $c_{11}=\rho v_L^2$ and $c_{44}=\rho v_T^2$ (Farnell, 1978) with ρ_{AlCuFe} = 4.5g/Cm^3. Poisson's ratio σ, which characterizes the elastic properties of the isotropic medium, is given by (Loudon, 1978)

$$v_t^2/v_l^2 = (1-2\sigma)/2(1-\sigma) \tag{115}$$

It turns out $c_{11}=2.3\times10^{12}$ dyn/cm^2 and $c_{44}=0.65\times10^{12}$ dyn/cm^2 for AlCuFe. These values are approximately twice those of the corresponding constant of aluminum. σ(AlCuFe)=0.305 and σ(Al)=0.356, i.e. $Al_{63.5}Cu_{24.5}Fe_{12}$ is more rigid than Al.

As to the attenuation of Rayleigh waves, two dominant responsible mechanisms are the attenuations by mass defects (Steg et al., 1970; Wallis et al., 1979) and by surface roughness (Maradudin et al., 1975 and 1976). In typical situations, however, it seems likely that the latter will be more significant than the former in determining the attenuation length (Wallis et al., 1979).

Maradudin and Mills discussed the attenuation of Rayleigh surface waves by surface roughness and gave an expression for the inverse mean free path of a phonon, l_R^{-1}, in a Gaussian model of small surface roughness,

$$\langle f(0)f(x_l)\rangle = \delta^2 \exp(-x_l^2/a^2) \tag{116}$$

In their calculation, the surface is in the x_1x_2-plane. The height of a point on the surface above x_1x_2-plane is $f(x_1,x_2)$. $x_l=\sqrt{(x_1^2+x_2^2)}$ and $\delta^2=<f(x_1,x_2)^2>$. a is the transverse correlation length that provides a rough measure of the mean separation of adjacent peaks or adjacent valleys. The mean-free path deduced is given by

$$l_R^{-1} = (\delta a/\pi)^2 (q_R)^5 F(aq_R) \tag{117}$$

where $F(aq_R)$ is also a function of v_R, v_T and v_L. In the long wavelength limit, $aq_R << 1$,

$$F(aq_R) = \frac{\pi^2}{R^2}\left(\frac{v_R}{v_t}\right)^4\left(1-\frac{1}{2}\frac{v_R^2}{v_T^2}\right)^{-2}\left(1-\frac{v_R^2}{v_L^2}\right)^{-1}\left(1-\frac{v_T^2}{v_L^2}\right)\left(\frac{1}{2}-\frac{v_T^2}{v_L^2}\right)+\frac{1}{32} \tag{118}$$

where R is a function of v_R, v_T and v_L too.

Since $F(aq_R)$ has almost the same value for Al and AlCuFe, leaving only $a\delta$ as a variable, the difference in attenuation of the Rayleigh phonon in Al and AlCuFe can be plausibly explained by a difference in surface roughness.

Appendix 1

Coupling of Acoustical Systems

Many problems of practical interest involve the interaction between two or more wave-carrying systems, coupled together so strongly that the motion of each is noticeably affected by the other. The simplest example of coupled wave motion is that of two copenetrating media which couple together at every point in space, e.g. a porous solid coupling to the air (or water) in its pores.

The solid portion can be considered as an interlocking mesh, and for waves considerably longer than pore size, it can be considered as an elastic medium of mean density ρ_s and volume compressibility κ_s. The fluid also has an effective density ρ_f which may not be equal to its density in free space, and an effective bulk modulus K_f. These two parts may have different displacements from equilibrium and different velocities.

It should be noted that compressional force can be applied to the two parts independently. For example, pressure can be applied to the air to change its density without appreciably changing the density of the solid fibres. Also, force can be applied to the fibre network which will compress the net without appreciably affecting the interspersed air (Morse, P. M. et al., 1986).

In Biot's paper (1956) where a volume of the solid-fluid system represented by a cube of unit size was considered, the stress tensor separated into two parts:

(1) the force acting on the solid part of each face of the cube, which is denoted as

$$\begin{bmatrix} \sigma_x & \tau_z & \tau_y \\ \tau_z & \sigma_y & \tau_x \\ \tau_y & \tau_x & \sigma_z \end{bmatrix} \tag{119}$$

(2) the force acting on the fluid part of each face of the cube, which is represented by

$$\begin{bmatrix} h & 0 & 0 \\ 0 & h & 0 \\ 0 & 0 & h \end{bmatrix} \tag{120}$$

The corresponding strain tensor in the solid is denoted as

$$\begin{bmatrix} e_x & \gamma_z/2 & \gamma_y/2 \\ \gamma_z/2 & e_y & \gamma_x/2 \\ \gamma_y/2 & \gamma_x/2 & e_z \end{bmatrix} \tag{121}$$

with

$$e_x=\partial s_x/\partial x,\ etc., \tag{122}$$

$$\gamma_z=\partial s_x/\partial y+\partial s_y/\partial x,\ etc., \tag{123}$$

where s_x, s_y, and s_z are the components of the displacement vector of the solid. And the strain tensor in the fluid is defined by

$$\epsilon=\frac{\partial S_x}{\partial x}+\frac{\partial S_y}{\partial y}+\frac{\partial S_z}{\partial z} \tag{124}$$

where S_x, S_y, and S_z are the components of the average fluid displacements.

The major part of the coupling between the two parts will come in the frictional force arising when the velocities of the solid net and the entrapped air are not equal. Morse gave out an expression of the linearized hydrodynamics equations for solid-air system, in which the continuity equations of the two portions are separate, but the equations of motion are coupled by the flow resistance Φ (1986):

$$\kappa_a\frac{\partial p_a}{\partial t}=-\nabla\cdot\vec{u}_a \qquad \kappa_s\frac{\partial p_s}{\partial t}=-\nabla\cdot\vec{u}_s \tag{125}$$

$$\rho_a\frac{\partial\vec{u}_a}{\partial t}=-\nabla p_a+\Phi\,(\vec{u}_s-\vec{u}_a) \tag{126}$$

$$\rho_s\frac{\partial\vec{u}_s}{\partial t}=-\nabla p_s+\Phi\,(\vec{u}_a-\vec{u}_s) \tag{127}$$

where p_a and p_s the components of the pressure applied to the air and to the solid respectively, κ's are the compressibilities, u's the velocities, Φ the flow resistance, and the subscript "a" and "s" mean "air" and "solid".

If no air is present, p_a is zero, $\vec{u}_a$ equals $\vec{u}_s$, and the solid network will transmit compressional waves with a wave velocity

$$v_s=\sqrt{1/\rho_s\kappa_s} \tag{128}$$

If the density and compressibility of the fibre structure were equal to that of the air, $\vec{u}_s$ again would equal $\vec{u}_a$, and the wave velocity would be equal to that of air,

$$v_a=\sqrt{1/\rho_a\kappa_a} \tag{129}$$

For intermediate cases the coupling will modify the wave velocity of both parts of the system. It is not hard to find that the wave vector q is given by

$$q^2=\frac{1}{2}\omega^2\,(\alpha_s^2+\alpha_a^2)\pm\frac{1}{2}\,[\omega^4\,(\alpha_s^2-\alpha_a^2)^2-4\omega^2\kappa_a\kappa_s\Phi^2]^{1/2} \tag{130}$$

where

$$\alpha_s^2 = \kappa_s\rho_s + i\frac{\kappa_s\Phi}{\omega}$$
$$\alpha_a^2 = \kappa_a\rho_a + i\frac{\kappa_a\Phi}{\omega} \tag{131}$$

if we consider the one-dimensional plane-wave solutions

$$p_a = p_{a0}e^{i(qx-\omega t)}, \qquad u_a = \frac{\omega\kappa_a}{q}p_a$$
$$p_s = p_{s0}e^{i(qx-\omega t)}, \qquad u_s = \frac{\omega\kappa_s}{q}p_s \tag{132}$$

for simplicity.

When $|v_a^2-v_s^2| >> 4\Phi^2/\omega^2\rho_a\rho_s$,

$$q^2 = (\frac{\omega}{v_s})^2+i\Phi\frac{\omega\rho_s}{v_s^2}+\frac{\Phi^2}{\rho_s\rho_a}\frac{1}{v_a^2-v_s^2} \tag{133}$$

or

$$=(\frac{\omega}{v_a})^2+i\Phi\frac{\omega\rho_a}{v_a^2}+\frac{\Phi^2}{\rho_s\rho_a}\frac{1}{v_s^2-v_a^2} \tag{134}$$

indicating two possible waves, with two velocities

$$v_1 = v_a(1+\frac{\Phi^2}{2\omega^2\rho_a\rho_s}\frac{v_a^2}{v_a^2-v_s^2}) \tag{135}$$

or

$$v_2 = v_s(1+\frac{\Phi^2}{2\omega^2\rho_a\rho_s}\frac{v_s^2}{v_s^2-v_a^2}) \tag{136}$$

Above is just a simple example which tells us that there will be as many different kinds of waves as there are different systems interacting.

Biot proposed a phenomenological theory of elastic and viscous behaviour in porous, macroscopically homogeneous, and isotropic, elastic media saturated with a compressible viscous fluid (Biot, 1956; Biot et al., 1957; Biot, 1962a; 1962b). Because the motion of the solid and fluid parts are followed separately and on equal footing, this theory represents the most general "effective medium" theory possible for two-component solid-fluid systems (Chandler, et al., 1981). The consequences of this theory is that there is always a fast and a slow compressional wave (the latter is diffusive at low frequencies) but only one shear wave because the fluid does not support a shear.

Gels are porous solids (Silberberg, 1989). Since a gel consists a cross-linked network immersed in a fluid, coupled equations should be used to describe the motion of the solvent molecules and the polymer network (Peters et al., 1989). Several persons presented their hydrodynamics equations for the gel system, e.g. Tanaka, T. et al. (1973), Bacri, J. C. et al. (1978), Marquess, J. A. et al. (1981), Johnson, D. L. (1982), Peters, A. et al. (1989), Shibayama, M. et al. (1993), and Onuki, A. (1993). In the following I will list two of them.

The linearized hydrodynamics equation adopted by Marqusee and Deutch are as follows:

$$\frac{\partial\delta\rho_n}{\partial t}+\rho_n^0\nabla\cdot\vec{u}=0 \tag{137}$$

$$\frac{\partial\delta\rho_f}{\partial t}+\rho_f^0\nabla\cdot\vec{U}=0 \tag{138}$$

$$\rho_n^0\frac{\partial\vec{u}}{\partial t}=G\nabla^2\vec{s}+(K_b+G/3)\nabla(\nabla\cdot\vec{s})+\beta\nabla(\nabla\cdot\vec{S})-f(\vec{u}-\vec{U}) \tag{139}$$

$$\rho_f^0\frac{\partial\vec{U}}{\partial t}=-v_0^2\nabla\delta\rho+\eta_s\nabla^2\vec{U}+(\eta_v+\eta_s/3)\nabla(\nabla\cdot\vec{U})+\beta\nabla(\nabla\cdot\vec{s})-f(\vec{U}-\vec{u}) \tag{140}$$

In these expressions, the first two are the continuity equations for the fluid and the network respectively, where $\vec{U}$ and $\vec{u}$ are the velocities of the fluid and the network. The other two are the equations of motion, where $\vec{S}$ and $\vec{s}$ are displacements of the fluid and the network respectively, β describes the coupling effect. The first two terms on the right-hand side of Eq. (139) is the elastic force, the last term denotes the frictional damping on the elastic network resulting from the fluid moving relative to the network, and the next to the last term contains the coupling effect of elastic waves in this two-phase system.

Based on Biot's theory about porous-fluid systems, Johnson proposed a more general set of linear dynamic equations for gel systems taking into account a mass coupling in the inertia terms. Johnson claimed that the inertia terms should in principle be replaced by

$$\rho_{11}\frac{\partial}{\partial t}u+\rho_{12}\frac{\partial}{\partial t}U = \rho_g^o\frac{\partial}{\partial t}u+(\alpha-1)\,\rho_f^o\frac{\partial}{\partial t}(u-U) \tag{141}$$

$$\rho_{22}\frac{\partial}{\partial t}U+\rho_{12}\frac{\partial}{\partial t}u = \rho_f^o\frac{\partial}{\partial t}U+(\alpha-1)\,\rho_f^o\frac{\partial}{\partial t}(U-u) \tag{142}$$

where ρ_{ij} are elements of a mass density matrix which take into account the fact that the relative fluid flow through the pores is not uniform, and α a purely geometrical constant larger than 1. General arguments show

$$\rho_{11} + \rho_{12} = \rho_g^{\circ},\ \rho_{22} + \rho_{12} = \rho_f^{\circ},\ \text{and}\ \rho_{12} = -(\alpha-1)\,\rho_f^{\circ}.$$

Appendix 2

Light scattering from Hydrodynamic Modes

The spectrum of scattered light is proportional to

$$I(\vec{q},\omega)=\int_{-\infty}^{+\infty}dt\ e^{-i\omega t}\langle\delta\varepsilon^{*}(\vec{q},0)\,\delta\varepsilon(\vec{q},t)\rangle \tag{143}$$

where $\delta\varepsilon(\vec{q},t)$ is the Fourier transform of the space and time dependent fluctuating dielectric constant $\delta\varepsilon(\vec{r},t)$:

$$\delta\varepsilon(\vec{q},t)=\int d\vec{r}\ e^{i\vec{q}\cdot\vec{r}}\delta\varepsilon(\vec{r},t) \tag{144}$$

The angular brackets (correlation functions) denote an average over the equilibrium fluctuations.

In general, we can assume that the system is in local equilibrium and that the dielectric fluctuations may be expressed in terms of linear deviations of a pertinent subset of the thermodynamic variables $\{\delta\Phi_j(\vec{q},t)\}$ from equilibrium:

$$\delta\varepsilon(\vec{q},t)=\sum_j\left(\frac{\partial\varepsilon}{\partial\psi_j}\right)\delta\psi_j(\vec{q},t) \tag{145}$$

where ψ_j can be density ρ, temperature T, entropy s, pressure p, etc. and the dielectric constant derivatives are evaluated at equilibrium. Thus, the spectrum

$$I(\vec{q},\omega)\propto\sum_{j,l}\left(\frac{\partial\varepsilon}{\partial\psi_j}\right)\left(\frac{\partial\varepsilon}{\partial\psi_l}\right) \times\int_{-\infty}^{+\infty}dt\; e^{-i\omega t}\langle\delta\psi_j^*(\vec{q},0)\,\delta\psi_l(\vec{q},t)\rangle \tag{146}$$

The time dependence of the fluctuations can be computed from appropriate linearized hydrodynamic equations.

The calculation of correlation functions is a tedious work. Here I just show the main steps using the linearized hydrodynamic equations for a pure monatomic fluid as an example.

The equations given by Berne and Pecora (1976) is as follows:

$$\begin{aligned}
&\frac{\partial\rho_1}{\partial t}+\rho_0\mu_1=0\\
&\frac{\partial\mu_1}{\partial t}+\frac{v_T^2}{\rho_0}\nabla^2\rho_1+\alpha v_T^2\nabla^2 T_1-D_v\nabla^2\mu_1=0\\
&\frac{\partial T_1}{\partial t}-\frac{(\gamma-1)}{\alpha\rho_0}\frac{\partial\rho_1}{\partial t}-\gamma D_T\nabla^2 T_1=0
\end{aligned} \tag{147}$$

where μ, D_v and D_T are defined as

$$\mu_1=\nabla\cdot\vec{u}_1; \qquad D_V=(\eta_V+\frac{4}{3}\eta_s)/m\rho_0; \qquad D_T=\lambda/m\rho_0 c_p \tag{148}$$

and the subscripts 1 denote the fluctuations of the corresponding quantities around their own equilibrium values, e.g. $\rho_1 \equiv \delta\rho(\vec{r},t)$. ρ_0 is the equilibrium density, v_T the isothermal sound speed, α the thermal expansion coefficient, c_p the specific heat at constant p and γ the specific heat ratio.

The easiest way to solve these equations is using Fourier-Laplace analysis. By the Fourier-Laplace ($i\omega$=s) transforms of the fluctuations,

$$\tilde{\rho}_1(\vec{q},s)=\int_0^\infty dt\ e^{-st}\int d^3r\ e^{i\vec{q}\cdot\vec{r}}\ \rho_1(\vec{r},t)=\int_0^\infty dt\ e^{-st}\ \rho_1(\vec{q},t) \tag{149}$$

etc. Eq. (147) can be expressed in matrix form as

$$\begin{bmatrix} s & \rho_0 & 0 \\ -\omega^2(q)/\gamma\rho_0 & (s+D_V q^2) & -\alpha\omega^2(q)/\gamma \\ -(\gamma-1)s/\alpha\rho_0 & 0 & (s+\gamma D_T q^2) \end{bmatrix} \begin{bmatrix} \tilde{\rho}_1(\vec{q},s) \\ \tilde{\mu}_1(\vec{q},s) \\ \tilde{T}_1(\vec{q},s) \end{bmatrix} = \begin{bmatrix} 1 & 0 & 0 \\ 0 & 1 & 1 \\ -(\gamma-1)/\alpha\rho_0 & 0 & 0 \end{bmatrix} \begin{bmatrix} \rho_1(\vec{q},t=0) \\ \mu_1(\vec{q},t=0) \\ T_1(\vec{q},t=0) \end{bmatrix} \tag{150}$$

where $\omega(q)\equiv vq$ and v is the adiabatic sound speed.

This matrix equation can be written in the more concise form

$$\mathbf{M}(q,\ s)\cdot\tilde{\psi}_1(\vec{q},\ s) = \mathbf{N}(q)\cdot\psi_1(\vec{q},t=0) \tag{151}$$

where there is a one-to-one correspondence, reading left to right, between the four matrices in Eqs. (150) and (151).

Its solution is

$$\bar{\psi}_1(\vec{q},s) = M^{-1}(q,s)\cdot N(q)\cdot\psi_1(\vec{q},t=0) \tag{152}$$

$M^{-1}(q,s)$ is the reciprocal of $M(q,s)$ and it can be expressed formally as

$$M^{-1}(q, s) = A(q,s)/|M(q, s)| \tag{153}$$

where $A(q,s)$ is a matrix which can be calculated from $M(q, s)$, and $|M(q,s)|$ the determinant of $M(q,s)$. Thus the solution can be expressed as

$$\bar{\psi}_1(\vec{q},s) = B(q,s)\cdot\psi_1(\vec{q},t=0)/|M(q, s)| \tag{154}$$

where $B(q,s) = A(q,s)\cdot N(q)$

But, for light scattering what we require are the correlation functions $<\psi_{1j}^*(\vec{q},t=0)\psi_{1l}(\vec{q},t)>$, which now can be found if we calculate their corresponding Laplace transforms first:

$$<\psi_{1j}^*(\vec{q},t=0)\psi_{1l}(\vec{q},s)>$$
$$=<\psi_{1j}^*(\vec{q},t=0)B_{li}(q,s)\psi_i(\vec{q},t=0)>/|M(q,s)| \tag{155}$$

then transform them back by doing inverse Laplace transforms.

In the above example, the results are greatly simplified because in the limit $q\to 0$:

$$\begin{aligned}\langle\rho_1^*(\vec{q},0)\,T_1(\vec{q},0)\rangle &= 0\\ \langle\rho_1^*(\vec{q},0)\,\mu_1(\vec{q},0)\rangle &= 0\\ \langle T_1^*(\vec{q},0)\,\mu_1(\vec{q},0)\rangle &= 0\end{aligned} \tag{156}$$

It can be seen from Eq. (155) that the behaviour of the spectrum will be governed by the roots of the determinant of the hydrodynamic matrix $\mathbf{M}(q,s)$. Indeed, if we are only interested in the position and the width of the Brillouin peaks, We just need solve the dispersion equation

$$|\mathbf{M}(q,s=i\omega)| = 0 \tag{157}$$

In the above example, the three roots are

$$\begin{cases} \omega_0 = iD_T q^2 \\ \omega_\pm = \pm v_s q + i\Gamma q^2 \end{cases} \tag{158}$$

where

$$\Gamma \equiv \frac{1}{2}[(\gamma-1)D_T + D_V] \tag{159}$$

is the classical attenuation coefficient of sound. These three roots describe one central peak and a Brillouin doublet.

List of Bibliography

Abreu, V. J. and Skinner W. R. (1989) *Appl. Opt.* **28**, 3382

Bacri, J. C. and Rajaonarison, R. (1978) *J. Phys. (Paris) Lett.* **40**, 5

Bedborough D. S. and Jackson, D. A. (1976) *Polymer* **17**, 573

Berne, B. J. and Pecora, R. (1976) in "*Dynamic Light Scattering*", p239, Toronto

Biot, M. A. (1956) *J. Acoust. Soc. Am.* **28**, 168, 179

Biot, M. A. and Willis, D. G. (1957) *J. Appl. Mech.* **24**, 594 Biot, M. A. (1962a) *J. Appl. Phys.* **33**, 1482

Biot, M. A. (1962b) *J. Acoust. Soc. Am.* **34**, 1254

Born, M. and Wolf, E. (1975) in "*Principle of Optics*", p325, Pergamon Oxford

Boyle, W. S. and Smith, G. E. (1970) *Bell Syst. Tech. J.* **49**, 587

Brinker, C. J. and Scherer, G. W. (1990) in "*Sol-Gel Science*"

Brown, W., Schillen, K., Johnsen, R., Konak, C. and Dvoranek, L. (1992) *Macromolecules* **25**, 802

Clark, A. H. and Ross-Marphy, S. B. (1987) *Adv. in Poly. Sci*, **83**, 57

Courtens, E. (1987) *Phys. Rev. Lett.* **58**, 128

de Gennes, P. -G. 1979 in "*Scaling Concepts in Polymer Physics*", Cornell University press

Derossi, D., Kajiwaka, K., Osada, Y. and Yamauchi, A. (1991) in "*Polymer Gels*"

Djabourov, M., Leblond J. and Papon, P. (1988) *J. Phys. France* **49**, 319

Djabourov, M. and Leblond J. (1987) in "*Reversible Polymeric Gels and Related Systems*", (P. S. Russo ed.)

Eldridge J. E. and Ferry, J. D. (1954) *J. Phys. Chem.* **58**, 992

Farnell, G. W. (1970). in "*Physical Acoustics*" Vol. 6. (W. P. Mason, ed), Academic Press, New York

Farnell, G. W. (1978) in "*Acoustic Surface Waves*", (A. A. Oliner ed.)

Favard, P., Lechaire, J., Maillard, M., Favard, N., Djabourov, M. and Leblond, J. (1989) *Bio. Cell*, **67**, 201

Ferry, J. D. (1948) *J. Am. Chem. S.* **70**, 2244

Flory, P. J. and Weaver, E. S. (1960) *J. Am. Chem. Soc.* **82**, 4518

Godard, P., Biebuyck, J. J., Daumerie, M., Naveau, H. and Mercier, J. P. (1978) *J. Poly. Sci.* **16**, 1817

Guenet, J. M. (1992) in "*Thermoreversible Gelation of Polymers and Biopolymers*", Academic Press

Hecht, E. (1987) in "*Optics*", 2nd edition, Addison-Wesley Publishing Company

Herning, T., Dlabouruv, M. and Leblond, J. (1991) *Polymer* 32, 3213

Herzfeld, K. F. and Litovitz, H. A. (1959) in "*Absorption and Dispersion of Ultrasonic Waves*", New York

Higgs, P. G. and Ross-Murphy, S. B. (1990) *Int. J. Bid. Macromol.* **12**, 233

Homes, C. C., Timusk, T., Wu, X., Altounian, Z., Sahnoune, A. and Strom-Olsen, J. O. (1991) *Phys. Rev. Lett.* **67**, 2694

Hosea, T. J. C. and Ng, S. C. (1986a) *Chem. Phys.* **103**, 345

Hosea, T. J. C. and Ng, S. C. (1986b) *Polymer* **27**, 1864

Janesick, J. and Blouke, M. (1987) *Sky & Telescope* **74**, 238

Johnson, D. L. (1982a) *J. Chem. Phys.* **77**, 1531

Johnson, D. L. and Plona, T. J. (1982b) *J. Acoust. Soc. Am.* **72**, 556

Kato, E. (1987) *J. Phys. Soc. Jap.* **56**, 1779

Kulicke, W. M. and Nottelmann, H. (1989) in "*Polymers in Aqueous Media*", edited by J. E. Glass

Litovitz T. A. and Davis C. M. (1965) in "*Physical Acoustics 2A*", (W. P. Mason ed.)

Loudon, R. (1978) *Phys. Rev. Lett.* **40**, 581

Loudon, R. and Sandercock, J. R. (1980) *J. Phys.* **C13**, 2609

Macsuga, D. D. (1972) *Biopolymers* **11**, 937

Mallamace, F., Micali, N., Cirino, V., Bansi, R., Pajevic, S. and Sciortino, F. (1992) *J. phys. II* (Paris) **12**, 2081

Maquet, J., Theveneau, H., Djabourov, M., Leblond, J. and Papon, P. (1986) *Polymer* **27**, 1103

Maradudin, A. A. and Mills, D. L. (1975) *Appl. Phys. Lett.* **28**, 573

Maradudin, A. A. and Mills, D. L. (1976) *Ann. Phys.* **100**, 262

Marqusee J. A. and Deutch, J. M. (1981) J. Chem. Phys. **75**, 5239

Michon, C., Cuvelier, G. and Launay, B. (1993) *Rheol. Acta* **32**, 9

Mishra, S. and Bray, R. (1977). *Phys. Rev. Lett.* **39**, 222

Munch, T. P., Candan, S., Duplessix, R., Picot, C., Herz, J. and Benoit, H. (1976) *J. Polym. Sci.* **14**, 1097

Ng, S. C., Teh, H. C., Hosea, T. J. C. and Gan, L. M. (1984) *Phys. Lett.* **105A**, 153

Ng, S. C., Hosea, T. J. C., Tch, H. C. and Gan, L. M. (1985a) *J. Phys. E* **18**, 250

Ng, S. C., Hosea, T. J. C. and Gan, L. M. (1985b) *J. phys. Lett.* **46**, L887

Ng, S. C. and Li, Y. (1993) *J.Phys. II France* 3, 1241

O'Connor C. L. and Schlupf, J. P. (1967) *J. Chem. Phys.* **47**, 31

Onuki, A. (1993) in "*Advances in Polymer Science*" **110**, (K. Dušek ed.), New York

Peters, A. (1989) in "*Polymers in Aqueous Media*", (J. E. Glass ed.)

Pezron, L., Djabourov, M. and Leblond, J. (1991) *J. Polymer*, **32**, 3201

Ren, S. Z., Shi. W. F., Zhang, W. B. and Sorensen, C. M. (1992) *Phys. Rev. A* **45**, 2416

Ren, S. Z. and Sorensen, C. M. (1993) *Phys. Rev. Lett.* **70**, 1727

Ross-Murphy, S. B. (1991) in "*Food Polymers, Gels and Colloids*", (E. Dickinson ed.)

Sandercock, J. R. (1978). *Solid State Commu.* **26**, 547

Sandercock, J. R. (1982). in *Light Scattering in Solids III*, (M. Cardona and G. Guntherodt ed.)

Shibayama, M. and Tanaka, T. (1993) In "*Advances in Polymer Science*" **109**, (K. Dusĕk ed.), New York

Silberberg, A. (1989) in "*Polymers in Aqueous Media*", (J. E. Glass ed.)

Stainsby, G. (1977) in "*The Science and Technology of Gelatin*", (A. G. Ward and A. Courts ed.)

Steg, R. G. and Klemens, P. G. (1970) *Phys. Rev. Lett.* **24**, 381

Tanaka, T., Hocker, L. O. and Benedek G. B. (1973) *J. Chem. Phys.* **59**, 5151

Tanaka, T. (1981) *Sci. Am.* **244**, 124

Tanaka, T. (1985) in "*Dynamic light scattering*", (R. Pecoren ed.)

te Nijenbuis, K. (1981) *Colloid & Polymer Sci.* **259**, 1017

Tokila, M. (1993) In "*Advances in Polymer Science*" **110**, (K. Dusĕk ed.), New York

Vanderwal, J. J., Mudare S. and Walton, D. (1981) *Opt. Commu.* **37**, 33

Wallis, R. F., Mills, D. L. and Maradudin, A. A. (1979) *Phys. Rev.* **B19**, 3981

Walton, D., Vanderwal, J. J. and Zhao, P. (1992) *Appl. Spectro.* **46**, 373

Walton, D. (1994) private conversation.

Wood, A. B. (1964) in "*A Textbook of Sound*", p360, London